

AD-767 280

THE INTERACTION OF A HYPERSONIC PLUME
WITH AN EXTERNAL HYPERSONIC STREAM

John T. Kelly

Polytechnic Institute of Brooklyn

Prepared for:

Army Research Office-Durham
Advanced Research Projects Agency

July 1973

DISTRIBUTED BY:

NTIS

National Technical Information Service
U. S. DEPARTMENT OF COMMERCE
5285 Port Royal Road, Springfield Va. 22151

CONTRACT No. DAHCO4-69-C-0077
ARPA ORDER No. 1442, AMENDMENT 2
PROGRAM CODE 9E30

VH

73-12

AD 767280

THE INTERACTION OF A HYPERSONIC PLUME
WITH AN EXTERNAL HYPERSONIC STREAM

by

JOHN T. KELLY



DDC
RECEIVED
OCT 8 1973
RECEIVED
E

POLYTECHNIC INSTITUTE OF BROOKLYN

DEPARTMENT
of
AEROSPACE ENGINEERING
and
APPLIED MECHANICS

JULY 1973

APPROVED FOR PUBLIC RELEASE;
DISTRIBUTION UNLIMITED.

Reproduced by
NATIONAL TECHNICAL
INFORMATION SERVICE
U.S. Department of Commerce
Springfield, VA. 22151

PIBAL REPORT No. 73-12

R

Unclassified
Security Classification

DOCUMENT CONTROL DATA - R & D

(Security classification of title, body of abstract and indexing annotation must be entered when the overall report is classified)

1. ORIGINATING ACTIVITY (Corporate author) Polytechnic Institute of Brooklyn Dept. of Aerospace Eng. & Applied Mechanics Route 110, Farmingdale, New York 11735		2a. REPORT SECURITY CLASSIFICATION Unclassified	
3. REPORT TITLE THE INTERACTION OF A HYPERSONIC PLUME WITH AN EXTERNAL HYPERSONIC STREAM		2b. GROUP	
4. DESCRIPTIVE NOTES (Type of report and inclusive dates) Research Report			
5. AUTHOR(S) (First name, middle initial, last name) John T. Kelly			
6. REPORT DATE July 1973		7a. TOTAL NO. OF PAGES 153 / 164	7b. NO. OF REFS 36
8a. CONTRACT OR GRANT NO. DAHC04-69-C-0077		9a. ORIGINATOR'S REPORT NUMBER(S) PIBAL Report No. 73-12	
b. PROJECT NO.		9b. OTHER REPORT NO(S) (Any other numbers that may be assigned this report)	
c. ARPA Order No. 1442, Amendment 2			
d. Program Code 9E30			
10. DISTRIBUTION STATEMENT Approved for public release; distribution unlimited.			
11. SUPPLEMENTARY NOTES		12. SPONSORING MILITARY ACTIVITY U.S. Army Research Office Box CM, Duke Station Durham, North Carolina 27706	
13. ABSTRACT A theoretical study of the gas dynamic interaction between a hypersonic plume and the opposed hypersonic external stream is presented. Steady, axisymmetric, inviscid, perfect gas flow is postulated for both the bow and far field regions. Limiting forms of solutions are obtained for the bow region by application of the Newton-Busemann approximation (i.e., $\epsilon_e, \epsilon_{io} \rightarrow 0$, $M_{\infty e}, M_{\infty io} \rightarrow \infty$ such that $M_{\infty e}^2 \epsilon_e, M_{\infty io}^2 \epsilon_{io} \rightarrow O(1)$) to both the exhaust plume and ambient air flow. Through asymptotic expansions and their matching, it is found that six regions are required to adequately describe the bow region. For the far field region, the hypersonic small-disturbance form of the Newton-Busemann approximation (i.e., $\epsilon_e \rightarrow 0$, $M_{\infty e} \rightarrow 0$, $\delta_e \rightarrow 0$ such that $M_{\infty e}^2 \delta_e^2 \epsilon_e \rightarrow O(1)$) is applied. From asymptotic expansions and their matching, it is found that "entropy wake" solutions are required to adequately describe the exhaust flow and the air flow near the contact surface. Analytical solutions are obtained which (i) define scaling parameters for the bow and far field flow; (ii) estimate the accuracy of the Newtonian impact theory in predicting bow region geometry and properties; (iii) establish the variation of bow and far field properties with variation in the primary system design parameters.			

DD FORM 1 NOV 65 1473

Unclassified
Security Classification

Unclassified

Security Classification

14. KEY WORDS	LINK A		LINK B		LINK C	
	ROLE	WT	ROLE	WT	ROLE	WT
Plume interaction Hypersonic Retro configuration						

THE INTERACTION OF A HYPERSONIC PLUME
WITH AN EXTERNAL HYPERSONIC STREAM

by

John T. Kelly

This research was sponsored by the Advanced Research Projects Agency of the Department of Defense and was monitored by the U.S. Army Research Office, Durham, North Carolina under Contract No. DAHC04-69-C-0077.

Reproduction in whole or in part is permitted for any purpose of the United States Government.

Polytechnic Institute of Brooklyn
Department
of
Aerospace Engineering and Applied Mechanics
July 1973

PIBAL Report No. 73-12

Approved for public release; distribution unlimited.

THE INTERACTION OF A HYPERSONIC PLUME
WITH AN EXTERNAL HYPERSONIC STREAM[†]

by

John T. Kelly[‡]

Polytechnic Institute of Brooklyn
Preston R. Bassett Research Laboratory
Farmingdale, New York

ABSTRACT

A theoretical study of the gas dynamic interaction between a hypersonic plume and the opposed hypersonic external stream is presented. Steady, axisymmetric, inviscid, perfect gas flow is postulated for both the bow and far field regions. Limiting forms of solutions are obtained for the bow region by application of the Newton-Busemann approximation (i.e., $\epsilon_e, \epsilon_{io} \rightarrow 0$, $M_{\infty e}, M_{\infty io} \rightarrow \infty$ such that $M_{\infty e}^2 \epsilon_e, M_{\infty io}^2 \epsilon_{io} \sim O(1)$) to both the exhaust plume and ambient air flow. Through asymptotic expansions and their matching, it is found that six regions are required to adequately describe the bow region. For the far field region, the hypersonic small-disturbance form of the Newton-Busemann approximation (i.e., $\epsilon_e \rightarrow 0$, $M_{\infty e} \rightarrow 0$, $\delta_e \rightarrow 0$ such that $M_{\infty e}^2 \delta_e^2 \epsilon_e \sim O(1)$) is applied. From asymptotic

[†]This research was supported by the Advanced Research Projects Agency of the Department of Defense and was monitored by the U.S. Army Research Office, Box CM, Duke Station, North Carolina 27706, under Contract No. DAHC04-69-C-0077.

The author would like to thank Prof. S. G. Rubin for his invaluable discussions during the course of this work.

[‡]Currently at Aerochem Research Labs., Princeton, New Jersey.

expansions and their matching, it is found that "entropy wake" solutions are required to adequately describe the exhaust flow and the air flow near the contact surface. Analytical solutions are obtained which (i) define scaling parameters for the bow and far field flow; (ii) estimate the accuracy of the Newtonian impact theory in predicting bow region geometry and properties; (iii) establish the variation of bow and far field properties with variation in the primary system design parameters.

TABLE OF CONTENTS

<u>Section</u>		<u>Page</u>
I	Introduction	1
II	Jet Exhaust Model	14
III	Analysis of Bow Region	19
IV	Discussion of Results	69
V	Analysis of Corner Region	79
VI	Far Field Region Analysis	91
VII	Discussion of Results	119
VIII	Conclusions	121
IX	References	124
	Appendix (A) Bow Initializing Scheme	127

LIST OF FIGURES

	Page
1 Schematic of Jet and External Flow Interaction	130
2 Flow Regimes	131
3 Undisturbed Plume Model Exponent as a Function of Angle and Distance	132
4 Experimentally Determined Shock and Contact Surface Locations Referred to R_{s10}	133
5 Predicted Contact Surface Shapes	134
6 Comparison of Shock and Contact Surface Positions	135
7 Comparison of Contact Surface Pressure Distributions	136
8 Comparison of Calculated Shocks and Contact Surface Positions with Experimental Results of Zakkay	137
9 Contact Surface Pressure Distribution.	138
10 Variation of Bow Geometry with n	139
11 Variation of Bow Geometry with θ_{∞}	140
12 Variation of Contact Surface Pressure with θ_{∞}	141
13 Variation of Bow Geometry with χ_j ...	142
14 Variation of Contact Surface Pressure with χ_j	143
15 Isobars and Streamlines for Bow Region	144
16 Density and Velocity Distributions for Bow Region	145
17 Isobars and Streamlines for Bow Region	146

LIST OF FIGURES (continued)

18	Density and Velocity Distributions for Bow Region	147
19	Corner Region	148
20	Core Pressure to Ambient Pressure vs. Jet Exit Mach Number	149
21	Far Field Shock and Contact Surface Position	150
22	Far Field Shock and Contact Surface Position	151
23	Far Field Properties vs. Stream Function	152
24	Far Field Properties vs. Stream Function	153

LIST OF SYMBOLS

c	Plume model angle parameter
D	Body diameter
F	Deviation of internal shock from a sphere
F_x	Axial force
H	Ratio of radius of curvature of flow streamlines within layer to that of the shock
L	Streamwise length scale
M	Mach number
n	Plume exponent
p	Pressure
q	Streamline velocity
r	Distance measured away from axis
R	Radius measured from jet in bow region or distance away from axis in far field region
T	Temperature
u	Velocity parallel to shock
U	Free stream velocity
v	Velocity normal to shock
x	Distance measured along shock
y	Bow region layer thickness
Y	Far field layer thickness
β	Shock angle in corner and far field
δ	Layer thickness
ϵ	Density ratio across shock
γ	Ratio of specific heats
κ	Radius of curvature

LIST OF SYMBOLS (continued)

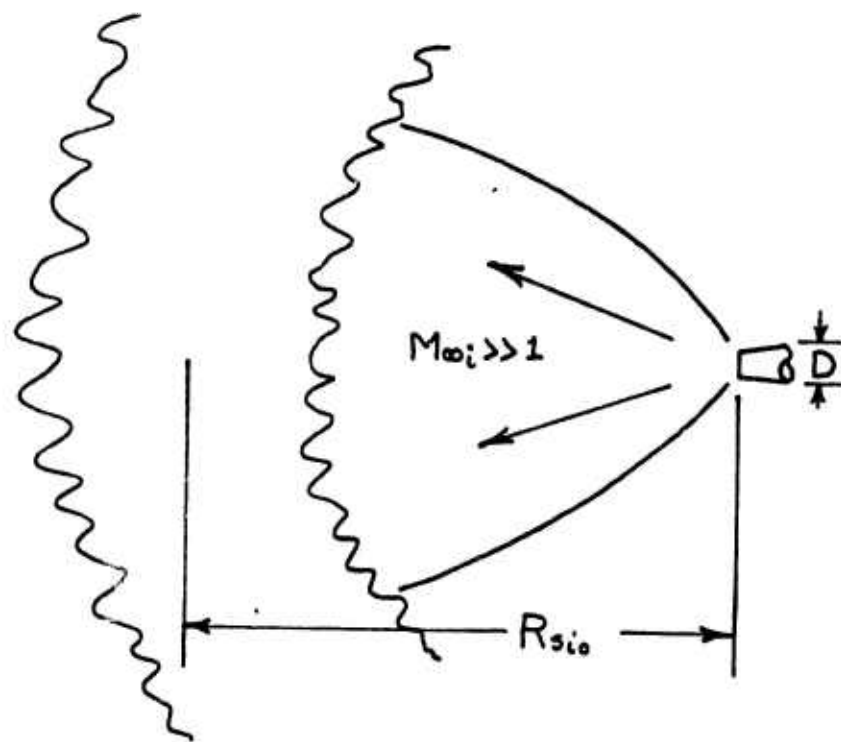
η	Ratio of calculated n to analytical approximation
μ	Viscosity
ρ	Angle measured from jet centerline
π	Ratio of jet stagnation to free stream dynamic pressure
ψ	Streamfunction
σ	Shock angle for bow region
θ_∞	Limiting angle for flow into a vacuum

SUBSCRIPTS

$0,1,2..$	Denotes the order of the term in the expansion
cs	Contact surface
e	External flow properties
i,j	Internal flow properties
$*$	Point at which flow has crossed shock
o	At internal normal shock point
l	Layer
s	Shock surface
∞	Free stream condition

INTRODUCTION

A theoretical study of the interaction of a highly underexpanded jet issuing into a high Mach number free stream that is opposed to the jet's expansion along its axis is presented. At some distance, characterized by the length R_{sio} the jet and free stream gases interact. The jet flow is thereby deflected downstream by the external flow. The particular case of interest to be examined in this study concerns flows where the typical dimension of the body D is much less than R_{sio} (see schematic (1)).



Schematic (1)

For this case, analytical models of the upstream and downstream gas dynamic interaction processes are formulated herein. The following approximations are postulated:

1. Steady Flow
2. Axisymmetric Flow
3. Continuum
4. Inviscid
5. Thermally and Calorically Perfect Gas

In further studies, assumption 4 can be partially relaxed by applying boundary layer concepts along the shear surfaces for high Reynolds' number flows. Also, assumption 5 can be relaxed quite easily by applying Mollier charts or similar models for equilibrium gas dynamic properties.

A general schematic of the flow structure under these assumptions is given in figure 1, where three distinct flow regions are discerned. The major characteristics of these regions are as follows:

Bow Region

This region is characterized by nearly normal interior and exterior shocks and relatively thin layers. The flow within the layers is then necessarily subsonic and of high density.

Corner Region

The layers thicken markedly and turn in a downstream direction. Both interior and exterior layers undergo transonic expansions about the relatively motionless core region surrounding the plume. The development of the plume ahead of

the internal shock resembles very closely that of a plume expanding into a quiescent ambient.

Far Field Region

The exterior shock and interface are at relatively small angles with the freestream. The flow in all layers is supersonic and nearly parallel to the axis.

Flow systems of these types are of considerable interest for the practical applications of force vector control and attendant surface thermal protection of re-entry vehicles. For force vector control, the altered pressure distribution on the body, as well as the jet thrust, has to be considered in calculating the total force on the body. For thermal protection, although the hot external gases are blown free from the nose by the jet, it is still necessary to consider the heat flux due to the possible reattachment of this separated gas flow on the body.

In addition to the effects already mentioned, which are manifested near the body, we must also be concerned with the flow field far downstream of the body. In this wake-like region, the mixing of the jet gases may affect the chemical processes occurring in the wake to such an extent that observable properties and hence detection or communication may be greatly facilitated or decreased. It is apparent that if such a system were to be properly utilized, a detailed understanding of the physical and chemical processes occurring within the disturbed flow field must be obtained.

Previous theoretical and experimental studies have added considerably to our basic knowledge in this area. The first studies ^{1,2,3} were essentially experimental in nature, applying only simplified modeling to correlate the data. A significant result of these early investigations ^{2,3} was that two modes of interaction were observed to exist. The modes were dependent upon the jet exit Mach number M_j , free stream Mach number M_{∞} , ratio of jet stagnation pressure to free stream dynamic pressure Π , body size D , and shape. One mode is characterized by large interaction distances with unsteady shocks and bounding surfaces. This flow regime is designated as the unstable case.

The second mode of interaction is characterized by a relatively short interaction length and steady strong shocks. This flow regime is the case investigated herein. The mechanism for transition from the steady to unsteady flow was postulated by Finley ³ to be a result of the development, for low Π and M_{∞} or high M_j , of a multiple cell structure for the undisturbed plume before the interaction region is reached. In view of the subsonic flow existing behind the Mach disc separating the cells, we have the possibility of upstream influence from the surrounding gases affecting the interaction region in a possibly unsteady manner.

The boundary between stable and unstable flow,^{1,2,3} for experiments where the effect of body size on the flow is negligible is given by:

$M_{\infty e}$	M_j	π
7.1	1.0	2
7.1	4.0	8
7.1	4.85	15
7.1	5.30	20
2.71	3.10	4
2.71	3.90	8

Thus, to achieve stable flow, the jet stagnation pressure must be much larger than the free stream dynamic pressure (i.e., $\pi \gg 1$) for moderate values of M_j . These are the same conditions under which R_{sio} becomes much larger than D (for D approximately equal to jet exit diameter); therefore, the case studied herein will always be of the stable type.

It should be noted that one investigator² observed a region for large values of π where the flow became unstable and continued to be so for all higher values of π . This result has not been duplicated by other investigators, and indications of stable interactions^{4,5,7} have been obtained from other experiments at conditions that fall within the region of unstable flow found in Reference 2.

In addition, it has been observed^{1,3,4} that the interaction length R_{sio} for the stable condition is a function of $\pi, \delta_j, \delta_e, M_{\infty e}, M_j, p_{\infty e}$ and that the contact surface separating the

external stream from the jet gases is almost spherical in nature. These observations have been utilized in constructing simplified models to describe the flow field associated with stable interactions.

Theoretical analyses of this jet interaction problem have appeared only recently. In 1969, Laurmann⁶, utilizing the Newtonian impact theory, calculated quantitative results for the upstream region. This paper presented general features of the upstream bow interaction, but did not correctly treat such areas as the corner region and the far field development of the flow. In 1971, a time-dependent numerical technique⁷ was employed by Rudman and Vaglio-Laurin to calculate detailed quantitative dynamic properties of the upstream flow interaction. In the calculations, the jet plume boundary layer intersection with the shock layers was assumed to be a point interaction and the core pressure was assumed to be that of the freestream. The downstream flow was not considered in the above report and only the bow region was evaluated.

The present study was undertaken for the primary task of correcting the errors inherent in a Newtonian impact analysis, to estimate the effect of the corner region on the total flow field, and to calculate the far field interaction.

An analytic approach was considered since such a method provides for the greatest insight into the physical processes and

also defines the accuracy associated with various approximations. Finally, this study also acts as a model for extending calculations to more complicated configurations; e.g., where the body influences the flow or where the jet is at an angle of incidence to the free stream.

We must now determine the operating conditions under which our simplifying assumptions are satisfied. For a missile or vehicle re-entering the earth's atmosphere, we have the following range of conditions from approximately 400,000 ft. altitude down to approximately 50,000 ft. altitude.

Range of Typical Operating Conditions for a Re-Entry Vehicle

$U_{\infty e}$ (ft/sec)	15,000	23,000
$M_{\infty e}$	10	25
$p_{\infty e}$ (lbf/ft ²)	6.92×10^{-5}	23.27

Over this range of operating conditions, we generally find that rarefaction, viscous, chemical or physical effects may be significant. This would violate our assumptions and therefore we must examine the relevant parameters and their numerical values in order to ascertain when our assumptions are fully satisfied.

The first limitation on the parameters involves the assumption of steady flow and requires that $\tau \gg 1$, $M_{\infty e} \gg 1$, $M_j = O(1)$. The reasons for this have been discussed previously. A second limitation relates to rarefaction effects occurring within the

flowfield. For the upstream region, we have three areas where rarefaction effects may invalidate the application of the analysis. The first area is the plume core itself where the large degree of expansion may take the free plume flow into the transitional regime. From an analysis of a steady spherical source flow expanding into a vacuum Hamel and Willis⁸ derived an expression for the distance beyond which the source gas becomes collisionless. This is given by

$$R_t \sim (Re_*)^{3/4} r_*$$

where r_* is the jet nozzle throat radius and Re_* is the Reynolds' number evaluated at the nozzle throat. This value is only a function of the nozzle throat conditions and hence is a constant for a particular set of chamber conditions. This can also be simply related to the thrust of our jet

$$R_t \sim \left(\frac{T}{g u_* I_{sp}} \right)^{3/5} \left(\frac{u_* u_*}{P_{0j}} \right)^{1/8}$$

where I_{sp} is the specific impulse, T is the thrust and P_{0j} is the jet chamber pressure. In order that the plume flow for our problem be a continuum, the interaction distance, R_{sio} , for the interior shock must be much less than the distance R_t . The interaction distance R_{sio} is determined by the condition of equal stagnation pressures along the axis. Therefore,

$$R_{sio} = r_* \left(\frac{P_* U_{\infty}^2 \epsilon_i^{1/2}}{\rho_{\infty} U_{\infty}^2} \right)^{1/2} \left(\int_0^{\theta_{\infty}} \cos^2 \frac{\pi \varphi}{2\theta_{\infty}} \sin \varphi d\varphi \right)^{-1/2}$$

This expression is a result of assuming a source like behavior for the undisturbed plume properties. The occurrence of the various quantities in the above expression will be detailed in a later section relating to undisturbed plume properties. The condition for continuum flow for the plume expansion is then

$$\frac{R_t}{R_{sio}} = (Re_*)^{3/4} \frac{r_*}{R_{sio}} \gg 1$$

In terms of the thrust of the jet, the above becomes

$$\frac{R_t}{R_{sio}} = \left(\frac{\gamma_e M_{oe}^2}{\epsilon_i^{1/2} (\gamma_i + 1)} \int_0^{\theta_{\infty}} \cos^n \frac{\pi \varphi}{2\theta_{\infty}} \sin \varphi d\varphi \right)^{1/2} \left(\frac{T}{g \mu_* I_{sp}} \right)^{1/4} \frac{P_{oe}^{1/2}}{\mu_*^3 U_*^{1/4} P_{oj}^{1/8}} = L$$

Following Reference (9) we take the numerical value of $\frac{R_t}{R_{sio}} \geq 10$ to be safely within the continuum region. This bound is indicated in Figure 2 for the representative conditions of

$$M_{oe} = 10, P_{oj} = 50 \text{ atm.}, \mu_* = 2 \times 10^{-6} \text{ lbf sec/ft}^2, U_* = 3000 \text{ fps}$$

$$\gamma_i = 1.25, I_{sp} = 300 \text{ sec}$$

We now direct our attention to the internal and external shock layers where rarefaction effects can result in the thickening of the shocks and shear layers to such an extent that they strongly influence the development of the layers. In a paper by Bush¹⁰ it was illustrated that the thickening of the shocks and growth of the viscous shear layers are related for the shock layers; and, therefore, we need only determine the thickness of the shock with respect to the layer thickness to de-

termine where inviscid continuum theory is valid. It has been shown ¹¹ that a continuum inviscid description of the flow is appropriate when

$$\delta_{le}/\delta_{se} \text{ , } \delta_{li}/\delta_{si} \geq 15$$

where in the above δ denotes thickness, and l denotes layer, s shock and e, i , external and internal layers respectively. From Adams and Probstein ¹² we have for the thickness of the shock for either external or internal flow

$$\delta_s = \nu^*/c^*$$

Where c^* and ν^* respectively are the speed of sound and viscosity evaluated at $M = 1$.

After introducing the interaction length R_{sio} as a significant length, this then reduces to ¹³

$$\frac{\delta_s}{R_{sio}} \approx M_\infty^{2\omega}/R_\infty \approx \mu_0/\mu_\infty R_\infty$$

Where ω is the exponent for temperature in the power law viscosity model, R_∞ is the Reynolds' number and M_∞ is the Mach number, based on free stream properties. We now introduce the first order thicknesses of the shock layers, which will be derived in detail in a later section.

$$\frac{\delta_{le}}{R_{sio}} \approx \epsilon_e \quad \frac{\delta_{li}}{R_{sio}} \approx \epsilon_{io}^{1/2}$$

Where ϵ_e, ϵ_i are the density ratios across the normal part of the shocks along the axis of symmetry.

Therefore,

$$\frac{\delta l_e}{\delta s_e} \approx \frac{\mu_{oe}}{\mu_e} \epsilon_e R_{oe} \quad \frac{\delta l_i}{\delta s_i} \approx \frac{\mu_{oi}}{\mu_i} \epsilon_i^{1/2} R_{oi}$$

where R_{oo} is based on the interaction distance R_{sio} . Using the source model for the plume properties and the equality of stagnation pressures to determine R_{sio} , we can reduce the above ratios to functions of jet thrust, T , jet throat properties and external flow gas properties. The results of this are:

$$\frac{\delta l_e}{\delta s_e} = \frac{\epsilon_e \gamma_e^{1/2} M_{oe} (T P_{oe})^{1/2} u_{*i}^{1/2}}{\mu_{oe} u_{oe} I_{sp}^{1/2} \sqrt{6} \epsilon_i^{1/4} \left(\int_0^{\theta_{oo}} \cos^2 \frac{\pi \varphi}{2\theta_{oo}} \sin \varphi d\varphi \right)^{1/2}} = N$$

$$\frac{\delta l_i}{\delta s_i} = \frac{\epsilon_i^{3/4} \gamma_e^{1/2} M_{oe} (T P_{oe})^{1/2} \int_0^{\theta_{oo}} \cos^2 \frac{\pi \varphi}{2\theta_{oo}} \sin \varphi d\varphi}{\mu_{*} u_{*}^{1/2} \sqrt{6} I_{sp}^{1/2}} = L$$

Using values stated previously which are representative of typical flight conditions, the above can be plotted as a function of altitude for a given thrust, above which rarefaction effects have to be accounted for. This has been carried out in Figure 2 and it can be seen that for jets of 10 to 10^5 pound force thrust, there is a large region of flow where the continuum inviscid analysis will apply.

We must now examine the region where perfect gas behavior or equilibrium gas behavior will apply. For the external shock layer, there are many analyses and data available which indicate when nonequilibrium effects in such general flow fields

become important. For the plume and internal flow, this is not the case. The reason for this is that rocket exhaust chemical composition, especially those of the solid propellant variety, varies greatly from application to application and in each case the bounds of equilibrium are different. Therefore, we cannot define a single general condition when nonequilibrium flow occurs. Therefore, we will set down the bound for the external flow as the limit for the combined layers above which the flow cannot be considered to be in equilibrium.

The external layer nonequilibrium bound is adapted from a paper by Cheng¹⁴ and is based on the relaxation processes behind a normal shock. When the distance for relaxation to equilibrium conditions behind the shock becomes of the same order of magnitude as the layer thickness, then nonequilibrium effects must be taken into account. Cheng's results gave a single point at high altitude, which when combined with binary scaling led to the result in Figure 2, above which nonequilibrium effects must be considered. Binary scaling derives from the fact that at high altitude the probability for chemical reactions to occur by three-body collisions is much less than that for two-body reactions. Under these conditions, it can be shown that if density and field dimension are held constant, then the degree of nonequilibrium will be the same in each case.

Since the body dimension R_{s_0} is related to jet thrust and density $\rho_{\infty e}$ is related to altitude, we can then establish a relationship between thrust and altitude, which will maintain the product of density and dimension constant, giving the same degree of nonequilibrium. The binary scaling principle only applies to high altitude, for moderate to low altitude collisions should be prevalent enough that equilibrium flow is maintained.

Referring to Figure 2, it is shown that for typical re-entry conditions the extent of the equilibrium, inviscid, continuum flow is about one half of the complete continuum, inviscid region; however, there is still a considerable region where all the assumptions stated previously are fully satisfied.

Now that we have determined our bounds of validity for an analysis based on several assumptions, we can proceed to outline the analysis in detail.

JET EXHAUST MODEL

The undisturbed plume which interacts with the external flow to form the bow layer develops in an environment (the core region) where there is little fluid motion and hence nearly constant pressure. Under these circumstances, the undisturbed plume is analogous to the case of a jet exhausting into a quiescent ambient which is at the core pressure. We can then employ analyses developed for plumes exhausting into quiescent ambients to our retro plume case. To be consistent with the analyses for the downstream and bow region, we will utilize an analytical approach for the undisturbed plume. There are many models available for describing the isentropic expansion of a jet far away from the nozzle exit. Many of them have the form 15, 16, 17*

$$\rho \propto \frac{\cos^n C\phi}{R^2} \quad (1)$$

Other properties can be determined from this expression by use of the isentropic flow relations (No's. 30.2-30.3 from the Bow Analysis).

*In this reference, an expression for Mach number is given which when substituted into the isentropic relationships for high Mach number gives a result identical to (1).

In (1) φ is the angle measured away from the axis of symmetry, R is radius measured from the nozzle exit and n and C are constants for a given nozzle and jet gas composition. Various forms have been proposed for n and C as functions of plume specific heat ratio γ_j , exit Mach number M_j , and nozzle exit angle Θ_n . Using the form $C = \pi/2\Theta_\infty$, where Θ_∞ is the sum of the Prandtl-Meyer limiting turning angle into a vacuum and Θ_n , gives the correct theoretical result of zero density or infinite Mach number when $\varphi = \Theta_\infty$. For this value of C , we can extract from a Prandtl-Meyer analysis¹⁵ near the nozzle lip the value for n .

$$n = \frac{2}{\gamma_j - 1} \quad (2)$$

This result can also be obtained from application of the small disturbance theory to hypersonic jets expanding into a vacuum¹⁸. As will be shown in the bow layer analysis section, these values for n and C give the physically realistic result in the limit as $\epsilon_{i_0} \rightarrow 0$ that the density and other flow variables remain of the same order as we go away from the axis. For any other choice of C and n as a function of γ_j the density would be finite on the axis and either zero or infinite away from the axis. Even though the form of n as a function of γ_j is correct, its numerical value for a given γ_j is still not clear. This is because comparisons with numerical results give different values for n , varying between the value

given in (2) and one half that value ¹⁹. The difficulty is that the form of equation (1) is not general enough to be valid over a full range of R and ϕ . This point is illustrated in an article by Boynton ¹⁵ where he shows for $\phi < .4$ the proportionality constant is approximately one and for $\phi > .4$ the numerical results lie closer to the curve for a proportionality factor of two. Since the bow shock layer and downstream layer depend critically on the undisturbed plume flow, (as will be shown in the bow and downstream analyses sections) then it was felt that a review of numerically calculated undisturbed plumes to give "best" values for n was justified. The expected value would probably lie somewhere between the theoretical value $\frac{2}{\gamma_j - 1}$ and $\frac{1}{\gamma_j - 1}$.

Three sources of numerical plume calculation data were chosen for examination to determine "best" values for n . In reference (20) numerical calculation of three plumes from supersonic nozzles expanding into a quiescent ambient were presented. Two of the nozzles ($\gamma_j = 1.15, 1.18$) are representative of those used for launch vehicles, and the third ($\gamma_j = 1.24$) is representative of spacecraft nozzles. The method of characteristics was used in this study to determine, for constant γ_j , Mach number contours, and density and temperature distributions along and perpendicular to the axis of symmetry. The second reference ¹⁶ contained the calculation of the plume resulting from the expansion of air through a sonic orifice. Mach number distributions perpendicular to the axis of sym-

metry were given. The third source used ¹⁵ contains results of a numerical calculation, using a finite difference technique, of the flow from a nozzle representative of a launch vehicle. Density is given as a function of angle from the axis in this work. To determine n from the above sources for points away from the axis, we simply use the isentropic relationships and the assumed distribution (1) to determine for a known value of the constant Θ_∞ and ρ at a given ϕ and R . However, near the axis this procedure does not yield good results since large changes in n produce little measured change in ρ or M in this region. In this case, we then apply a derivative of the density distribution to obtain a better relationship for determining n . For the first and second references where properties are given as functions of r , the distance perpendicular to the axis, the expression

$$n = \left(\frac{2\Theta_\infty}{\pi}\right)^2 \left(-1 + \frac{(\alpha/r_j)^2}{(r/r_j)^2} \frac{1}{2} \frac{\partial(\rho/\rho_{\infty i_0})}{\partial(r/r_j)}\right) \quad (3)$$

establishes n from the density gradient perpendicular to the axis. For the third reference, we use

$$n = -\left(\frac{2\Theta_\infty}{\pi}\right)^2 \frac{1}{\phi} \frac{\partial(\rho/\rho_{\infty i_0})}{\partial \phi} \quad (4)$$

Values of η , the ratio of n calculated from 3 and 4, to $2/(\delta_j - 1)$ are plotted in figure (3) as a function of φ/θ_∞ and x/r_j . From this graph, it is evident that n is not a constant but varies both as a function of φ/θ_∞ and x/r_j . If use is to be made of (1) in calculating retro plumes, then for each change in x/r_j a new value of n must be determined from figure (3).

The variation of n with φ/θ_∞ is not as critical as the axial variation since the bulk of the mass flow, which determines the plume external stream interaction, lies near the axis and therefore the behavior for $\varphi/\theta_\infty > .5$ is not significant to the interaction. Also, for φ/θ_∞ near zero the density is near one for any value of n . Noting this, we then take the value of n found at $\varphi/\theta_\infty = .25$ to be the "best" value for a given x/r_j . Characteristic retro plume calculations have been carried out with values of n determined from figure (3). Results of these calculations will be discussed in the sections on bow and downstream analyses.

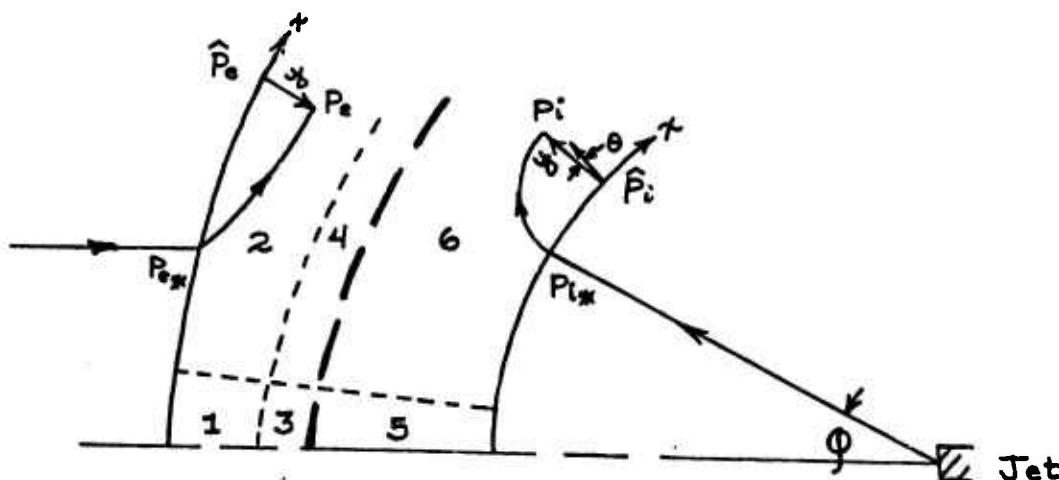
ANALYSIS OF BOW REGION

For the problem studied here $M_{\infty e}, M_{\infty i_0} \gg 1$ and $\beta_e, \beta_i \approx 0$

The flow within the internal and external shock layers are determined by a perturbation theory for strong shock waves and small layer thicknesses. The procedure involves a limit* of the governing equations and boundary conditions when

$$\epsilon_e, \epsilon_{i_0} \rightarrow 0 \quad M_{\infty e}, M_{\infty i_0} \rightarrow \infty \quad \text{and} \quad M_{\infty e}^2 \epsilon_e, M_{\infty i_0}^2 \epsilon_{i_0} = O(1) \text{ where}$$

$\epsilon_e, \epsilon_{i_0}$ are the density ratios across the shocks at the axis. To elucidate some detail of the flows within the layers, the coordinates normal to the shocks are expanded in powers of $\epsilon_e^l, \epsilon_{i_0}^m$ where l, m are to be determined. The orders of magnitude of the various flow quantities in terms of $\epsilon_e, \epsilon_{i_0}$ and $M_{\infty e}^2 \epsilon_e, M_{\infty i_0}^2 \epsilon_{i_0}$ are derived from the requirement that the shock relations and flow equations yield a nontrivial system which includes all the physical effects of interest as $\epsilon_e, \epsilon_{i_0} \rightarrow 0$. The coordinate systems are shock oriented and are illustrated in schematic (2)



Schematic (2)

*This limit will be denoted the N-B limit after Newton-Busemann

Upon application of the N-B limit mentioned above, it is found that the flow field divides into several regions within which unique asymptotic expansions for the dependent variables must be determined. It will be shown in the following analysis that four regions characterized by two major effects are required to describe adequately the external flow and two regions characterized by two major effects are needed for the internal flow. In both the internal and external layers, a region characterized by constant density to first order is formed near the axis of symmetry. Away from the axis, the density and other properties vary both along and across the layers. For the external layer, a region characterized by non-constant stream velocity is formed near the contact surface in both the near and away from axis regions. This contrasts with the character of the region near the shock where the velocity is constant to first order.

The regions are numbered one through six in schematic (2)*. Once the flow properties are established in each of these regions, then matching between the expanded properties will be demonstrated to show their consistency and where necessary, composite expansions will be formulated. The final step in the solution to the bow region problem will consist of the numerical matching of contact surface pressure and position (i.e., flow deflection) between the external and internal shock layer flows.

* These regions, of course, are not drawn to scale.

To achieve this result: (i) initial radii of curvatures and positions of internal and external shocks will be found from a scheme which uses solutions obtained for regions 1,3, and 5 (this scheme will be outlined in appendix (A)); (ii) shocks will be extended away from the axis utilizing these radii of curvature;(iii) external and internal contact surface pressure and position will then be calculated, using solutions from regions 2, 4 and 6. The pressures and positions are then compared to determine if numerical matching is achieved; (iv) if equality to a certain tolerance is not found, then the radii of curvatures are iterated until matching is achieved. Having accomplished matching, the procedure starting from step (ii) will be repeated using the newly found radii of curvatures as the initial values.

A brief outline of the regions considered and their major characteristics is now given.

For region two, which is of $O(\epsilon)$ in thickness and $O(1)$ in length, the N-B limit gives the familiar hypersonic blunt body result, which has been investigated in whole or in part by many authors^{10, 21, 22}. The orders of magnitude of the flow quantities in this region are the same as those directly behind the shock. A major characteristic of the solution found is that the velocity along streamlines is constant in the first order approximation. This result, adequate for points near the shock, has been shown to be incorrect¹⁰ near the

contact surface in region 4; and, therefore, a new expansion must be sought. In reference (10) the initial orders of magnitude of the flow variables in region 4 were established as well as the thickness of this region, which is $O(\epsilon^{3/2})$. To first order when the N-B limit is applied, the constant streamline velocity result of the region 2 analysis must be replaced by an expression for velocity which accounts for pressure gradients along streamlines which are found to be the same for all streamlines in this layer. After determining expressions for the flow variables in region 4 matching with region 2 is then demonstrated and a composite expansion is then formed which is valid throughout regions 2 and 4. For general shock shapes these expressions must be numerically integrated to yield values for the flow variables of interest. Having established results for distances of $O(1)$ away from the axis, we now wish to determine expansions valid near the axis in the N-B limit for use in the initial radii of curvatures of the shocks scheme.

In this study, unlike in past investigations,^{10, 21, 22} attention is focused on this near axis region because we are seeking accurate and simple analytic expressions for the layer thickness and contact surface pressure distribution as functions of shock radius of curvature to be used in the initializing scheme. It will be shown that the near axis region 1

will be of $O(\epsilon_0)$ in thickness and $O(\epsilon_0^{1/2})$ in length. This region is characterized by constant density to first order. As in the region away from the axis, the first order velocity along streamlines is constant. Consequently, as in the away from axis case in region 3 near the contact surface we must modify the expansions to include the effect of non-constancy of velocity along streamlines. The dimensions of this region are $O(\epsilon_0^{3/2})$ in thickness and $O(\epsilon_0^{1/2})$ in length. The variables found in this region are demonstrated to match with those of region 1. A composite expansion for region 1 and region 3 is then formulated. Finally, matching between 1, 3 and 2, 4 is demonstrated for the specific case of a spherical external shock.

For the internal layer analysis, more details will generally be included than for the external flow since this work appears here for the first time. For region 6, which is $O(1)$ in length, the N-B limit leads to the results that the layer thickness and streamline velocity to first order, for non-trivial results, must be of $O(\epsilon_0^{1/2})$. Also, the internal shock is spherical in form and the first order pressure and density are constant across the layer with an error $O(\epsilon_0^{1/2})$. These results will lead to interesting conclusions, which will be discussed at the end of the analysis. The solution found in 6 unlike the external flow case is valid throughout the shock layer for distances of $O(1)$. For general shock shapes, these

equations must be numerically integrated away from the axis. As in the external flow case, a region of $O(\epsilon_i^{1/2})$ in thickness and of $O(\epsilon_i^{1/2})$ in length is required near the axis to be used in the initializing scheme. As for the external layer, the near axis region 5 is found to have constant density to first order. A solution technique is then applied which makes use of this characteristic to determine analytic expressions for internal layer thickness and contact surface pressure distribution near the axis to be used in the initializing scheme. Having found solutions for the variables in region 5, we then match these to the variables obtained in region 6 for the specific case of a spherical shock.

The detailed analyses for each of the six regions will now be given.

External Layer - Region 2 Analysis

Following previous investigations,²¹ we obtain the orders of magnitude of the variables inside the layer from the values obtained from the shock relations. These relations are:

$$\hat{p}_e - p_{oe} = \rho_{oe} U_{oe}^2 (1 - \hat{\epsilon}) \sin^2 \hat{\sigma} \quad (1.1)$$

$$\hat{u} = U_{oe} \cos \hat{\sigma} \quad (1.2)$$

$$\hat{v} = U_{oe} \hat{\epsilon} \sin \hat{\sigma} \quad (1.3)$$

$$\hat{\rho} = 1/\hat{\epsilon} = 1 / \left(\frac{\gamma_e - 1}{\gamma_e + 1} + \frac{2}{(\gamma_e + 1) M_{oe}^2 \sin^2 \hat{\sigma}} \right) \quad (1.4)$$

Non dimensionalizing the pressure by $\rho_{oe} U_{oe}^2$, velocity by U_{oe} and density by ρ_{oe} , we obtain from (1.1-1.4)

$$\hat{p} = 1/\gamma_e M_{oe}^2 + (1 - \hat{\epsilon}) \sin^2 \hat{\sigma} \quad (2.1)$$

$$\hat{u} = \cos \hat{\sigma} \quad (2.2)$$

$$\hat{v} = \hat{\epsilon} \sin \hat{\sigma} \quad (2.3)$$

$$\hat{\rho} = 1/\hat{\epsilon} \quad (2.4)$$

Taking the NB limit, we find from (2.1-2.4)

$$\hat{p} \cong \sin^2 \hat{\sigma} \quad (3.1)$$

$$\hat{u} \cong \cos \hat{\sigma} \quad (3.2)$$

$$\hat{v} \cong \epsilon_e \sin \hat{\sigma} \quad (3.3)$$

$$\hat{\rho} \cong 1/\epsilon_e \quad (3.4)$$

Using the orders of magnitude established by (3.1-3.4), we can now write the following expansions:

$$u = u_0 + \epsilon_e u_1 + \dots \quad (4.1)$$

$$v = \epsilon_e v_0 + \epsilon_e^2 v_1 + \dots \quad (4.2)$$

$$p = p_0 + \epsilon_e p_1 + \dots \quad (4.3)$$

$$\rho = \rho_0/\epsilon_e + \rho_1 + \dots \quad (4.4)$$

In order that the flow variables described previously lead to a meaningful description of the flow, we must stretch the normal coordinate y . From the continuity equation we find for y

$$y \approx \frac{\dot{m}}{\rho u 2\pi r} \approx \frac{r^2 \frac{\rho_0 \epsilon_e U_0 \epsilon \pi}{\rho_0 \epsilon_e U_0 \epsilon 2\pi}}{\epsilon_e} \approx r \epsilon_e$$

Since $r \approx O(R_{s0})$ which is set as the unit length scale, then $y \approx O(\epsilon_e)$. Therefore, to obtain non-trivial results, we must stretch y by $O(\epsilon_e)$. The expansions of the variables and the stretched coordinate y should now be applied to the governing equations

$$\frac{\partial \rho u r}{\partial x} + \frac{\partial \rho v r H}{\partial y} = 0 \quad H = 1 - \kappa y \quad (5.1)$$

$$u \frac{\partial u}{\partial x} + H v \frac{\partial u}{\partial y} - \kappa u v + \frac{1}{\rho} \frac{\partial p}{\partial x} = 0 \quad (5.2)$$

$$u \frac{\partial v}{\partial x} + H v \frac{\partial v}{\partial y} - \kappa u^2 + \frac{H}{\rho} \frac{\partial p}{\partial y} = 0 \quad (5.3)$$

$$u \frac{\partial \rho/\rho^*}{\partial x} + v H \frac{\partial \rho/\rho^*}{\partial y} = 0 \quad (5.4)$$

Before substituting in the expansions of the variables, it will be advantageous for final integration of the equations to change the above system to one employing the stream function as an independent variable.

Define

$$\frac{\partial \Psi}{\partial x} = H r \rho v \quad (6.1)$$

$$\frac{\partial \Psi}{\partial y} = -r \rho u \quad (6.2)$$

The above system under the transformation

$$\frac{\partial}{\partial x} = \frac{\partial \Psi}{\partial x} \frac{\partial}{\partial \Psi} + \frac{\partial}{\partial x}$$

$$\frac{\partial}{\partial y} = \frac{\partial \Psi}{\partial y} \frac{\partial}{\partial \Psi}$$

then becomes

$$H r \frac{\partial p}{\partial \Psi} = \frac{Dv}{Dx} + \kappa u \quad (7.1)$$

$$(u^2 + v^2)/2 + h = (u_*^2 + v_*^2)/2 + h_* \quad (7.2)$$

$$p/\rho^\delta = p_*/\rho_*^\delta \quad (7.3)$$

$$\frac{Dy}{Dx} = H \frac{v}{u} \quad (7.4)$$

The distance across the layer in terms of Ψ is obtained from

$$\frac{\partial y}{\partial \Psi} = - \frac{1}{r \rho u} \quad (7.5)$$

In this system we then must add

$$r = r_0 + \epsilon_e r_2 + \dots \quad (8.1)$$

$$H = 1 - \kappa_0 \gamma_0 \epsilon_e + \dots \quad (8.2)$$

Expanded boundary conditions at the shock are:

$$\hat{p} = \epsilon_e / M_{\infty}^2 \epsilon_e + \left(1 - \epsilon_e \left(1 + \frac{\cot^2 \hat{\sigma}}{M_{\infty}^2 \epsilon_e} \right) \right) \sin^2 \hat{\sigma} \quad (9.1)$$

$$\hat{u} = \cos \hat{\sigma} \quad (9.2)$$

$$\hat{v} = \epsilon_e \left(1 + \frac{\cot^2 \hat{\sigma}}{M_{\infty}^2 \epsilon_e} \right) \sin \hat{\sigma} \quad (9.3)$$

$$\hat{\rho} = 1 / \left(\epsilon_e \left(1 + \frac{\cot^2 \hat{\sigma}}{M_{\infty}^2 \epsilon_e} \right) \right) \quad (9.4)$$

This then gives the result for first and second order boundary conditions:

$$\hat{p}_0 = \sin^2 \hat{\sigma} \quad (10.1)$$

$$\hat{u}_0 = \cos \hat{\sigma} \quad (10.2)$$

$$\hat{v}_0 = \left(1 + \cot^2 \hat{\sigma} / M_{\infty}^2 \epsilon_e \right) \sin^2 \hat{\sigma} \quad (10.3)$$

$$\hat{\rho}_0 = 1 / \left(1 + \cot^2 \hat{\sigma} / M_{\infty}^2 \epsilon_e \right) \quad (10.4)$$

$$\hat{p}_2 = 1 / M_{\infty}^2 \epsilon_e - \left(1 + \cot^2 \hat{\sigma} / M_{\infty}^2 \epsilon_e \right) \sin^2 \hat{\sigma} \quad (10.5)$$

$$\hat{u}_1 = 0 \quad (10.6)$$

$$\hat{v}_1 = 0 \quad (10.7)$$

$$\hat{\rho}_1 = 0 \quad (10.8)$$

Substituting (4.1-4.4) into (5.1-5.4) and then collecting terms of like order in ϵ_e we obtain

First Order Problem

$$p_0 = \hat{p}_0 - \frac{\kappa}{r_0} \int_{\psi}^{\hat{\psi}} u_{0*} d\psi \quad (11.1)$$

$$(11.2)$$

$$\rho_0 = \rho_0 \rho_{0*} / \rho_{0*} \quad (11.3)$$

$$u_0 = u_{0*} \quad (11.4)$$

$$v_0 = u_0 \frac{\partial y_0}{\partial x} \quad (11.5)$$

$$y_0 = \int_{\psi}^{\hat{\psi}} \frac{d\psi}{\rho_0 u_0 r_0}$$

Second Order Problem

$$p_1 = \hat{p}_1 - \int_{\psi}^{\hat{\psi}} \left[\frac{\kappa u_1}{r_0} + \frac{1}{r_0} \frac{\partial v_1}{\partial x} + \frac{\kappa u_1}{r_0} (\kappa y_0 r_0 + y_0 \cos \sigma) \right] d\psi \quad (12.1)$$

$$(12.2)$$

$$\rho_1 = \rho_0 \rho_{1*} / \rho_{0*} + (\rho_1 / \rho_0 - \rho_{1*} / \rho_{0*}) \rho_{0*} \rho_0 / \rho_{0*} \quad (12.3)$$

$$u_1 = - \frac{\rho_{0*}}{u_0 \rho_{0*}} \ln \rho_0 / \rho_{0*} \quad (12.4)$$

$$v_1 = u_0 \frac{\partial y_1}{\partial x} + \kappa y_0 v_0 + v_0 (u_1 / u_0) \quad (12.5)$$

$$\frac{\partial y_1}{\partial \psi} = \frac{1}{\rho_0 u_0 r_0} (\rho_1 / \rho_0 + u_1 / u_0 + r_1 / r_0)$$

Equations (11.1) to (12.5) describe all the properties of interest near the shock, with an error $O(\epsilon^{3/2})$.

External Layer - Region 4 Analysis

Bush¹⁰ has determined from these results that equations (11.1) to (12.5) are not valid at the contact surface due to the change in order of magnitude of streamline velocity and hence another expansion is required. Following his results, we derive the system of equations valid in the contact surface region with an error $O(\epsilon^{3/2})$.

The expansions for the variables in this region are:

$$u = \epsilon e^{1/2} \tilde{u}_0 + \epsilon e \tilde{u}_1 + \dots \quad (13.1)$$

$$v = \epsilon e^2 \tilde{v}_0 + \epsilon e^{5/2} \tilde{v}_1 + \dots \quad (13.2)$$

$$p = \tilde{p}_0 + \epsilon e \tilde{p}_1 + \dots \quad (13.3)$$

$$\rho = \tilde{\rho}_0 / \epsilon e + \tilde{\rho}_1 + \dots \quad (13.4)$$

$$r = r_0 + \epsilon e^{3/2} r_1 + \dots \quad (13.5)$$

$$H = 1 + \kappa_0 \tilde{y}_0 \epsilon e^{3/2} + \dots \quad (13.6)$$

$$x = \tilde{x} \quad (13.7)$$

$$y = \epsilon e^{3/2} \tilde{y} \quad (13.8)$$

These will be substituted into the governing equations (5.1) to (5.4). The resulting systems of equations are:

First order system of equations

$$\frac{\partial \tilde{p}_0}{\partial \tilde{y}} = 0 \quad (14.1)$$

$$\tilde{u}_0 \frac{\partial \tilde{u}_0}{\partial \tilde{x}} + \tilde{v}_0 \frac{\partial \tilde{u}_0}{\partial \tilde{y}} + \frac{1}{\tilde{\rho}_0} \frac{\partial \tilde{p}_0}{\partial \tilde{x}} = 0 \quad (14.2)$$

$$\tilde{\rho}_0 / \tilde{\rho}_0 = \tilde{\rho}_{0*} / \tilde{\rho}_{0*} \quad (14.3)$$

$$\frac{\partial \tilde{r}_0 \tilde{\rho}_0 \tilde{u}_0}{\partial \tilde{x}} + \frac{\partial \tilde{r}_0 \tilde{\rho}_0 \tilde{v}_0}{\partial \tilde{y}} = 0 \quad (14.4)$$

Second order system of equations

$$\frac{\partial \tilde{p}_1}{\partial \tilde{y}} = 0 \quad (15.1)$$

$$\tilde{u}_0 \frac{\partial \tilde{u}_1}{\partial \tilde{x}} + \tilde{u}_1 \frac{\partial \tilde{u}_0}{\partial \tilde{x}} + \tilde{v}_0 \frac{\partial \tilde{u}_1}{\partial \tilde{y}} + \tilde{v}_1 \frac{\partial \tilde{u}_0}{\partial \tilde{y}} + \quad (15.2)$$

$$1/\tilde{\rho}_0 \frac{\partial \tilde{p}_1}{\partial \tilde{x}} - \frac{\tilde{p}_1}{\tilde{\rho}_0^2} \frac{\partial \tilde{\rho}_0}{\partial \tilde{x}} = 0 \quad (15.3)$$

$$\tilde{\rho}_1 = \tilde{\rho}_0 \tilde{\rho}_{1*} / \tilde{\rho}_{0*} + \left(\frac{\tilde{p}_1}{\tilde{\rho}_0} - \frac{\tilde{p}_{1*}}{\tilde{\rho}_{0*}} \right) \tilde{\rho}_{0*} \frac{\tilde{\rho}_0}{\tilde{\rho}_{0*}}$$

We can extract from (14.1) to (15.4)

First order results

$$\tilde{p}_0 = \tilde{p}_0(x) \quad (16.1)$$

$$\tilde{u}_0^2 = \tilde{u}_{0*}^2 - 2\tilde{p}_{0*}/\tilde{\rho}_{0*} \ln \tilde{p}_0/\tilde{p}_{0*} \quad (16.2)$$

$$\tilde{\rho}_0 = \tilde{p}_0 \tilde{\rho}_{0*} / \tilde{p}_{0*} \quad (16.3)$$

Second order results*

$$\tilde{p}_1 = \tilde{p}_1(x) \quad (17.1)$$

$$2\tilde{u}_0\tilde{u}_1 = 2\tilde{u}_{0*}\tilde{u}_{1*} - 2\frac{\tilde{p}_{0*}^2}{\tilde{\rho}_{0*}\tilde{p}_0} \left(\frac{\tilde{p}_1}{\tilde{p}_{0*}} - \right. \quad (17.2)$$

$$\left. \frac{\tilde{p}_0\tilde{p}_{1*}}{\tilde{\rho}_{0*}^2} \right) - 2 \left(\frac{\tilde{p}_{1*}}{\tilde{\rho}_{0*}} - \frac{\tilde{p}_{1*}\tilde{p}_{0*}}{\tilde{\rho}_{0*}^2} \right) \ln \tilde{p}_0/\tilde{p}_{0*} \quad (17.3)$$

$$\tilde{\rho}_1 = \frac{\tilde{p}_0\tilde{\rho}_{1*}}{\tilde{\rho}_{0*}} + \left(\frac{\tilde{p}_1}{\tilde{p}_0} - \frac{\tilde{p}_{1*}}{\tilde{\rho}_{0*}} \right) \tilde{\rho}_{0*} \tilde{p}_0 / \tilde{p}_{0*}$$

These body layer results must be matched to the external layer region 2 results in an intermediate region where both expansions are valid.

* \tilde{v}_0 is not considered since it does not affect the calculation of \tilde{p}, \tilde{y} to error greater than $O(\epsilon^{3/2})$ and is itself very small of $O(\epsilon^{3/2})$.

We now demonstrate matching for the variables p, ρ and u .
 Matching occurs within the intermediate region defined by η .
 In this region

$$\lim_{\epsilon_e \rightarrow 0} y \rightarrow 0 \qquad \lim_{\epsilon_e \rightarrow 0} \tilde{y} \rightarrow \infty$$

In terms of the variables $\hat{\varphi}, \varphi_*$ and $\tilde{\varphi}, \tilde{\varphi}_*$ with $\hat{\varphi}, \tilde{\varphi}$ of $O(1)$ we have from the expression for layer thickness, (7.5),

$$\varphi_* = O(1) \qquad \tilde{\varphi}_* = O(\epsilon_e^{1/2})$$

The order of η must then fall in the range

$$O(\epsilon_e^{1/2}) < \eta < O(1)$$

Following Cole²³, matching will be achieved if for each power of ϵ_e we have

$$\lim_{\epsilon_e \rightarrow 0} (\tilde{f} - f) \Rightarrow 0$$

where f is the variable of interest to be matched. Taking the matching of the pressure first

$$\lim_{\epsilon_e \rightarrow 0} (\tilde{p}(\tilde{\varphi}) - p(\hat{\varphi}, \varphi_* \rightarrow 0)) \Rightarrow 0$$

Therefore, the pressure in the body layer is equal to the pressure at the inner boundary of the external layer. A composite expansion valid in both regions can be determined by subtracting the common term to both expansions which is the pressure at the contact surface. The correct pressure distribution will then be that derived from the external flow. For matching of the density, we must have

$$\lim_{\epsilon_e \rightarrow 0} \left(\tilde{p}(\tilde{\phi}, \tilde{\phi}_* \rightarrow \frac{\eta \phi_\eta}{\epsilon_e^{1/2}}) - p(\hat{\phi}, \phi_* \rightarrow \eta \phi_{*\eta}) \right) \Rightarrow 0$$

From (16.3) and (17.3) we have

$$\tilde{p} = \frac{\tilde{p}_0}{\epsilon_e} + \left(\frac{\tilde{p}_1}{\tilde{p}_0} + 1 + \frac{1}{M_\infty^2 \epsilon_e} \right) \tilde{p}_0$$

Since \tilde{p}_0 and \tilde{p}_1 are just functions of $\tilde{\phi}$ then $\tilde{p}(\tilde{\phi})$; therefore

$$\lim_{\epsilon_e \rightarrow 0} \left(\tilde{p}(\tilde{\phi}) - p(\hat{\phi}, 0) \right) \Rightarrow 0$$

The density within the body layer is then equal to that at the inner boundary of the external layer. As in the case of the pressure distribution, the uniformly valid density distribution is simply given by that derived for the external layer. The velocity now has to be matched. Once again, as for p and ρ , we must find

$$\lim_{\epsilon_e \rightarrow 0} \left(\tilde{u}(\tilde{\phi}, \tilde{\phi}_* \rightarrow \infty) - u(\tilde{\phi}, \phi_* \rightarrow 0) \right) \Rightarrow 0$$

For the body layer, we have

$$\begin{aligned} \tilde{u}_{0*} &= \tilde{\theta}_* & \tilde{p}_{0*} &= \tilde{p}_{0*} = 1 & \tilde{u}_{1*} &= 0 \\ \tilde{p}_{1*} &= -1 + \frac{1}{M_{\infty_e}^2 \epsilon_e} & \tilde{p}_{1*} &= 0 \end{aligned}$$

Under the above conditions \tilde{u} from (16.2) and (17.2) becomes

$$\begin{aligned} \tilde{u} &= \epsilon_e^{1/2} \left(\tilde{\theta}_*^2 - 2 \ln \tilde{p}_0(\tilde{\phi}) \right)^{1/2} + \\ &\frac{\epsilon_e \left(-1/\tilde{p}_0(\tilde{\phi}) \left(\tilde{p}_1(\tilde{\phi}) - \tilde{p}_0(\tilde{\phi}) \left(\frac{1}{M_{\infty_e}^2 \epsilon_e} - 1 \right) \right) - \right.}{\left(\tilde{\theta}_*^2 - 2 \ln \tilde{p}_0(\tilde{\phi}) \right)^{1/2}} \\ &\quad \left. \left(\frac{1}{M_{\infty_e}^2 \epsilon_e} - 1 \right) \ln \tilde{p}_0(\tilde{\phi}) \right) \end{aligned}$$

The near shock expression for the velocity is from (11.3) and (12.3)

$$u = \theta_* - \frac{\epsilon_e}{\theta_*} \frac{p_{0*}}{\beta_*} \ln p_0/p_{0*}$$

For matching in the intermediate region η we transform the independent variables such that

$$\tilde{\theta}_* = \frac{\theta_* \eta \eta_*}{\epsilon_e^{1/2}} \Rightarrow \infty \quad \epsilon_e \Rightarrow 0$$

$$\theta_* = \theta_* \eta \eta \Rightarrow 0 \quad \phi_* = \phi_* \eta \eta \Rightarrow 0 \quad \epsilon_e \Rightarrow 0$$

The matching condition then becomes

$$\begin{aligned} \lim_{\epsilon_e \rightarrow 0} \left(\epsilon_e^{1/2} \left(\frac{\theta_* \eta \eta}{\epsilon_e^{1/2}} - \frac{\epsilon_e^{1/2} \ln \tilde{p}_0}{\theta_* \eta \eta} - \frac{(\ln \tilde{p}_0)^2 \epsilon_e^{3/2}}{2 \theta_*^3 \eta^3} + \dots \right. \right. \\ \left. \left. + \epsilon_e \frac{(-\tilde{p}_2/\tilde{p}_0 + 1/M_{\infty}^2 \epsilon_e - 1 - (1/M_{\infty}^2 \epsilon_e - 1) \ln \tilde{p}_0)}{\left(\frac{\tilde{\theta}_* \eta \eta}{\epsilon_e^{1/2}} - \frac{\ln \tilde{p}_0 \epsilon_e^{1/2}}{\tilde{\theta}_* \eta \eta} - \frac{(\ln \tilde{p}_0)^2 \epsilon_e^{3/2}}{2 \tilde{\theta}_*^3 \eta^3} + \dots \right)} \right. \\ \left. - \theta_* \eta \eta + \frac{\epsilon_e \ln p_0(\hat{\phi}, 0)}{\theta_* \eta \eta} \right) \Rightarrow 0 \end{aligned}$$

The above can be seen to match to error $O(\epsilon_e^{3/2})$. A composite expansion valid in both regions is then

$$\begin{aligned} u = \left(\theta_*^2 - 2 \epsilon_e \ln p_0(\hat{\phi}, 0) \right)^{1/2} - \\ \frac{\epsilon_e \left(p_{0*}/p_{0*} \ln p_0/p_{0*} - \ln p_0(\hat{\phi}, 0) \right)}{\left(\theta_*^2 - 2 \epsilon_e \ln p_0(\hat{\phi}, 0) \right)^{1/2}} \end{aligned} \quad (18.1)$$

The layer thickness can now be calculated from

$$y = \int_0^{\psi} \frac{d\psi}{\rho u r}$$

Once the radius of curvature and position of the shock are known, then all the layer properties may be calculated.

Now that we have the results for the external flow away from the axis, we will now determine if they apply in the region near the axis. From the external flow, the velocity parallel to the shock is given by

$$u = \Theta_* - 2\epsilon_e \ln p_0(\hat{\phi}, 0)$$

As we approach the axis both $\hat{\phi}$ and ϕ_* , as well as Θ_* become smaller than $O(1)$. For this situation, the expansions based on the above quantities being of order one are then no longer valid and new expansions must be obtained. It is of importance to develop an accurate solution in this near axis region as the final matching of the external stream layer flow and jet layer flow depend on knowing the initial locations and radii of curvature of the shock surfaces near the axis of symmetry.

External Layer - Region 1 Analysis

To establish these initial values for the external flow, it is convenient to determine the shock layer thickness and contact surface pressure distribution in an analytic form. This leads us to describe the external shock as an expansion in even powers of $\hat{\phi}$ for the region near the axis. The expansion is

$$R = 1 + a_e \hat{\phi}^2 + b_e \hat{\phi}^4 + \dots$$

It is sufficient to retain only the first two of the above terms for accuracy consistent with the number of terms in the dependent variable expansions. The expansions for the dependent variables which give the relevant physical behavior in the near axis case and are consistent with the shock relations are

$$\begin{aligned}
 p &= p_0' + \epsilon_e p_1' + \dots \\
 \rho &= \rho_0'/\epsilon_e + \rho_1' + \dots \\
 u &= \epsilon_e^{1/2} u_0' + \epsilon_e^{3/2} u_1' + \dots \\
 v &= \epsilon_e v_0' + \epsilon_e^2 v_1' + \dots \\
 x &= \epsilon_e^{1/2} x' \quad y = \epsilon_e y'
 \end{aligned}$$

Inserting the above in equations (7.1) - (7.5), we obtain for the first order results

$$\frac{\partial p_0'}{\partial \Psi'} = 0 \quad (19.1)$$

$$p_0'/\rho_0' = p_{0*}'/\rho_{0*}' \quad (19.2)$$

$$u_0' = u_{0*}' \quad (19.3)$$

$$v_0' = u_0' \frac{\partial y_0'}{\partial x'} \quad (19.4)$$

$$y_0' = \int_0^{\Psi'} \frac{d\Psi'}{\rho_0' u_0' r_0'} \quad (19.5)$$

For the second order, we obtain

$$r_0' \frac{\partial p_1'}{\partial \Psi'} = \kappa_0' u_0' + \frac{\partial v_0'}{\partial x'} \quad (20.1)$$

$$p_1' = \frac{p_0'}{p_{0*}'} p_{1*}' + \left(\frac{p_1'}{p_0'} - \frac{p_{1*}'}{p_{0*}'} \right) p_{0*}' \frac{p_0'}{p_{0*}'} \quad (20.2)$$

$$2u_0' u_1' + v_0'^2 = 2u_{0*}' u_{1*}' + v_{0*}'^2 - 2 \left(\frac{\rho_1'}{\rho_0'} - \frac{\rho_{1*}'}{\rho_{0*}'} \right) \quad (20.3)$$

$$y_1' = \int_0^{\Psi'} \frac{d\Psi'}{\rho_0' u_0' r_0'} \left(\frac{\rho_1'}{\rho_0'} + \frac{u_1'}{u_0'} + \frac{r_1'}{r_0'} \right) \quad (20.4)$$

The boundary conditions obtained from (1.1) - (1.4) are

$$\rho_{0*}' = \rho_0' = 1 \quad u_{0*}' = \varphi_*'(1-2ae) \quad v_{0*}' = 1$$

$$\rho_{1*}' = - \left(1 + \varphi_*'^2 (1-2ae)^2 - 1/M_{\infty e}^2 \epsilon_e \right)$$

$$\rho_{1*}' = - \frac{\varphi_*'^2 (1-2ae)^2}{M_{\infty e}^2 \epsilon_e} \quad u_{1*}' = - \varphi_*'^3 (1-2ae)^3 / 6$$

For $R = 1 + ae \hat{\varphi}'^2$ (19.1 to 19.5) and (20.1 to 20.4) give for first order

$$\rho_0' = \rho_0' = 1 \quad (21.1)$$

$$u_0' = (1-2ae) \varphi_*' \quad (21.2)$$

$$v_0' = (\varphi_*' / \hat{\varphi}')^2 \quad (21.3)$$

$$y_0' = \frac{1}{(1-2ae)} \left(1 - \varphi_*' / \hat{\varphi}' \right) \quad (21.4)$$

For second order, we have

$$\rho_1' = - \left(1 + \hat{\varphi}'^2 (1-2ae)^2 - 1/M_{\infty e}^2 \epsilon_e \right) - \left((1-2ae)^2 (\hat{\varphi}'^2 - \varphi_*'^3 / \hat{\varphi}') / 3 - (1 - (\varphi_*' / \hat{\varphi}')^4) / 2 \right) \quad (22.1)$$

$$\rho_{1*}' = \frac{(1-2ae)^2 \varphi_*'^2}{M_{\infty e}^2 \epsilon_e} + (\varphi_*'^2 - \hat{\varphi}'^2) (1-2ae)^2 - \left((1-2ae)^2 \hat{\varphi}'^2 - \varphi_*'^3 / \hat{\varphi}' - \frac{1}{2} (1 - (\varphi_*' / \hat{\varphi}')^4) \right) \quad (22.3)$$

$$u_1' = \frac{1}{(1-2ae) 2 \varphi_*'} \left(- \frac{(1-2ae)^4 \varphi_*'^4}{3} - 2 \left(- \hat{\varphi}'^2 (1-2ae)^2 + (1-2ae)^2 (\hat{\varphi}'^2 - \varphi_*'^3 / \hat{\varphi}') / 3 - (1 - (\varphi_*' / \hat{\varphi}')^4) / 2 \right) \right) \quad (22.4)$$

External Layer - Region 3 Analysis

As in the case away from the axis, we must develop a body layer solution near the contact surface. The relevant expansions for the variables in this region are

$$\begin{aligned} p &= p_0'' + \epsilon_e p_1'' + \dots \\ \rho &= \rho_0''/\epsilon_e + \rho_1'' + \dots \\ u &= \epsilon_e u_0'' + \dots \\ v &= \epsilon_e^2 v_0'' + \dots \\ x &= \epsilon_e x'' \quad y = \epsilon_e^{3/2} y'' \end{aligned}$$

Substituting the above in the equations (7.1) to (7.5), and collecting terms of like power in ϵ_e , we obtain for first order results

$$\frac{\partial p_0''}{\partial \psi''} = 0 \quad (23.1)$$

$$p_0''/\rho_0'' = p_0''^*/\rho_0''^* \quad (23.2)$$

For second order results

$$\frac{\partial p_1''}{\partial \psi''} = 0 \quad (24.1)$$

$$u_0''^2 = u_0''^{*2} + 2(p_1''^* - p_1'') \quad (24.2)$$

$$p_1'' = \frac{p_0'' p_1''^*}{\rho_0''} + \left(\frac{p_1''^*}{\rho_0''} - \frac{p_1''^*}{\rho_0''^*} \right) \frac{\rho_0''^* p_0''}{\rho_0''} \quad (24.3)$$

The boundary conditions which must be applied are

$$p_0''^* = \rho_0''^* = 1 \quad u_0''^* = (1 - 2\alpha\epsilon) \Phi_0''^*$$

$$p_{1*}'' = 1/M_{\infty}^2 \epsilon_e - 1$$

The final results which must be matched to the near axis outer region case are then

$$p_0'' = p_0''(x) \quad (25.1)$$

$$\rho_0'' = \rho_0''(x) \quad (25.2)$$

$$p_1'' = p_1''(x) \quad (25.3)$$

$$\rho_1'' = \rho_1''(x) \quad (25.4)$$

$$u_0'' = ((1-2a_e)^2 \Phi_*''^2 + 2(p_{1*}'' - p_1'')) \quad (25.5)$$

Following the same procedure as in the away from the axis case, matching requires that

$$p_0''(x) = p_0' = 1 \quad (26.1)$$

$$\rho_0''(x) = \rho_0' = 1 \quad (26.2)$$

$$p_1'' = p_1'(\hat{\Phi}, 0) = -\left(\frac{1}{2} + \frac{4}{3}\hat{\Phi}'^2(1-2a_e)^2 - \frac{1}{M_{\infty}^2 \epsilon_e}\right) \quad (26.3)$$

$$\rho_1'' = \rho_1'(\hat{\Phi}, 0) = -\frac{4}{3}\hat{\Phi}'^2(1-2a_e)^2 + \frac{1}{2} \quad (26.4)$$

The values obtained for (26.3) and (26.4) are simply those derived from the near shock region expressions evaluated at the contact surface. The value of u_0'' is then

$$u_0'' = \left((1-2a_e)^2 \Phi_*''^2 + 2\left(-\frac{1}{2} + \frac{4}{3}\hat{\Phi}'^2(1-2a_e)^2\right)^{1/2} \right) \quad (26.5)$$

Matching to outer layer results, we require that

$$\begin{aligned} \lim_{\epsilon_e \rightarrow 0} (u' - u'') &\Rightarrow 0 \\ \lim_{\epsilon_e \rightarrow 0} \left(\epsilon_e^{1/2} (1-2a_e) \phi_n' \eta + \frac{\epsilon_e^{3/2}}{2(1-2a_e)} (-2(1-2a_e)^4 \phi_n'^3 \eta^3 / 6 - \right. \\ &\quad \left. \frac{2}{\phi_n \eta} (-\hat{\phi}'^2 (1-2a_e)^2 + (1-2a_e)^2 (\hat{\phi}'^2 - \phi_n'^3 \eta^3 / \hat{\phi}')) / 3 - \right. \\ &\quad \left. \frac{1}{2} (1 - \phi_n'^4 \eta^4 / \hat{\phi}'^4) \right) - \epsilon_e ((1-2a_e)^2 \frac{\phi_n^2 \eta^2}{\epsilon_e} + \\ &\quad \left. 2 \left(\frac{4}{3} \hat{\phi}'^2 (1-2a_e)^2 - \frac{1}{2} \right) \right) + \frac{\epsilon_e^3}{2(1-2a_e)} \frac{\phi_n^3 \eta^3}{\epsilon_e^{3/2}} \left(-\frac{1}{3} \right)^{**} \Rightarrow 0 \end{aligned}$$

Expanding the square root

$$\begin{aligned} \lim_{\epsilon_e \rightarrow 0} \left(\epsilon_e^{1/2} (1-2a_e) \phi_n' \eta + \frac{\epsilon_e^{3/2}}{2(1-2a_e)} \left(\frac{-2(1-2a_e)^4 \phi_n'^3 \eta^3}{6} - \right. \right. \\ \left. \frac{2}{\phi_n \eta} (-\hat{\phi}'^2 (1-2a_e)^2 + (1-2a_e)^2 (\hat{\phi}'^2 - \phi_n'^3 \eta^3 / \hat{\phi}')) / 3 - \right. \\ \left. \frac{1}{2} (1 - \phi_n'^4 \eta^4 / \hat{\phi}'^4) - \epsilon_e ((1-2a_e) \phi_n \eta / \epsilon_e^{1/2} + \right. \\ \left. \epsilon_e^{1/2} (4/3 \hat{\phi}'^2 (1-2a_e)^2 - 1/2) / (1-2a_e) \phi_n \eta - \right. \\ \left. \frac{\epsilon_e^3}{2 \phi_n^3 \eta^3} (4/3 \hat{\phi}'^2 (1-2a_e)^2 - 1/2) + \frac{\epsilon_e^3 \phi_n^3 \eta^3}{2(1-2a_e)} \left(-\frac{2}{6} \right) \right) \Rightarrow 0 \end{aligned}$$

** From boundary conditions derived on the basis of mass flow through body layer

It is seen that matching is assured. A uniformly valid result for velocity in both regions is then

$$u = \left(\epsilon_e^{1/2} \left((1-2a_e)^2 \varphi_*'^2 + 2\epsilon_e \left(\frac{4}{3} \hat{\varphi}'^2 (1-2a_e)^2 - \frac{1}{2} \right) \right)^{1/2} \right. \\ \left. + \epsilon_e^{3/2} \left(-\frac{2}{6} (1-2a_e)^4 \varphi_*'^4 - 2 \left(-\hat{\varphi}'^2 (1-2a_e)^2 + (1-2a_e)^2 (\hat{\varphi}'^2 - \varphi_*'^3 / \hat{\varphi}') / 3 - \frac{1}{2} (1 - \varphi_*'^4 / \hat{\varphi}'^4) \right) - \frac{4}{3} \left(\hat{\varphi}'^2 (1-2a_e)^2 - \frac{1}{2} \right) \right) \right. \\ \left. 2 \left((1-2a_e)^2 \varphi_*'^2 + 2\epsilon_e \left(\frac{4}{3} \hat{\varphi}'^2 (1-2a_e)^2 - \frac{1}{2} \right) \right)^{1/2} \right) \quad (27.1)$$

Using the uniformly valid results, we calculate the layer thickness from (22.2) (27.1) and (7.5), which gives

$$y' = \frac{\epsilon_e}{(1-2a_e)} \left((1 + \frac{8}{3} \epsilon_e)^{1/2} - (\frac{8}{3} \epsilon_e)^{1/2} \right) + \epsilon_e^2 \frac{2.6}{(1-2a_e)} \\ + \epsilon_e (1-2a_e) \left(\frac{1}{18} + \frac{11}{12} + \frac{1}{3 M_{\infty}^2 \epsilon_e} \right) \hat{\varphi}'^2 \quad (28.1)$$

The contact surface pressure distribution is given by (21.1) and (22.1)

$$p_{cs}' = 1 - \frac{\epsilon_e}{2} - (1-2a_e)^2 \frac{4}{3} \hat{\varphi}'^2 \epsilon_e + \frac{\epsilon_e}{M_{\infty}^2 \epsilon_e} \quad (28.2)$$

Expressions (28.1) and (28.2) are then used in a scheme, outlined in Appendix A, which determines the external shock radius of curvature and position along the axis of symmetry, for given external flow and jet conditions. These values are then used as initial conditions for determining flow properties away from the axis.

The solutions found for regions 1 and 3 as the variable

$\hat{\phi}'$ tends to infinity must match the solution found for regions 2 and 4 as $\hat{\phi}$ vanishes. If matching is achieved, then we have proof that the expansions for the region near the axis was the correct one.

For this analysis, a composite expansion for the near axis and away from axis regions is not sought. Therefore a matching of these regions for the special case of a spherical shock will demonstrate the consistency of the expansions and will involve a much smaller calculational effort than if the general shock case were attempted.

The away from axis results, equations (12.1), (12.2), (18.1), for a spherical shock and small $\hat{\phi}$ are

$$u^2 = \phi_*^2 - \phi_*^4/3 + 2\epsilon_c \left(\hat{\phi}^2 \frac{4}{3} - \phi_*^3/3\hat{\phi} - \phi_*^2 \right)$$

$$\begin{aligned} p = 1 - \frac{\epsilon_c}{2} - \frac{4}{3}\hat{\phi}^2 + \frac{\phi_*^3}{3\hat{\phi}} - \frac{1}{12}\hat{\phi}^2\epsilon_c - \frac{\epsilon_c\hat{\phi}^2}{M_{\infty}^2\epsilon_c} \\ + \frac{4}{3}\epsilon_c\phi_*\hat{\phi} - \frac{\epsilon_c}{12}\frac{\phi_*^4}{\hat{\phi}^2} - \frac{\epsilon_c}{3}\frac{\phi_*^3}{\hat{\phi}} + \frac{\epsilon_c}{M_{\infty}^2\epsilon_c} - \frac{\epsilon_c}{2}\frac{\phi_*^4}{\hat{\phi}^4} \\ + \frac{2}{3}\epsilon_c\frac{\phi_*^3}{\hat{\phi}^3} - \frac{\epsilon_c}{2}\frac{\phi_*^4}{\hat{\phi}^2} \end{aligned}$$

$$\begin{aligned} p = 1 - \frac{4}{3}\hat{\phi}^2 + \frac{\phi_*^3}{3\hat{\phi}} - \phi_*^2 \left(\frac{1}{M_{\infty}^2\epsilon_c} - 1 \right) + \\ \epsilon_c \left(-1 + \hat{\phi}^2 \left(1 - \frac{1}{M_{\infty}^2\epsilon_c} - \frac{13}{12} \right) + \frac{1}{2} + \frac{4}{3}\hat{\phi}\phi_* - \frac{7}{12}\frac{\phi_*^4}{\hat{\phi}^2} \right. \\ \left. - \frac{\phi_*^3}{3\hat{\phi}} - \frac{1}{2}\frac{\phi_*^4}{\hat{\phi}^4} + \frac{2}{3}\frac{\phi_*^3}{\hat{\phi}} + \frac{4}{3}\hat{\phi}^2 - \frac{\phi_*^3}{3\hat{\phi}} + \left(1 + \frac{\phi_*^2}{M_{\infty}^2\epsilon_c} \right. \right. \\ \left. \left. - \phi_*^2 \right) + \phi_*^2 \left(1 - \frac{1}{M_{\infty}^2\epsilon_c} \right) \right) \left(1 - \frac{\phi_*^2}{M_{\infty}^2\epsilon_c} - \frac{4}{3}\hat{\phi}^2 + \phi_* \left(\frac{\phi_*}{3\hat{\phi}} + 2 \right) \right) \end{aligned}$$

The near axis results for a spherical shock, $a_e = 0$, from equations (27.1), (21.1), (22.1) and (22.2) are given by

$$u^2 = \epsilon_e \varphi_*'^2 + 2\epsilon_e^2 \left(-\frac{\varphi_*'^4}{3} - 2 \left(-\hat{\varphi}'^2 + \frac{\hat{\varphi}'^2 - \varphi_*'^3/\hat{\varphi}'}{3} \right) - \left(1 - (\varphi_*'/\hat{\varphi}')^4 \right) \right)$$

$$\rho = 1 - \epsilon_e/2 - 4/3 \epsilon_e \hat{\varphi}'^2 + \epsilon_e \varphi_*'^3/3 \hat{\varphi}' + \epsilon_e/M_{\infty}^2 \epsilon_e - \epsilon_e \varphi_*'^4/\hat{\varphi}'^4$$

$$\rho = 1 + \epsilon_e \varphi_*'^2/M_{\infty}^2 \epsilon_e + \epsilon_e (\varphi_*'^2 - \hat{\varphi}'^2) - \epsilon_e \left(\frac{\hat{\varphi}'^2 - \varphi_*'^3/\hat{\varphi}'}{3} - \frac{1}{2} \left(1 - (\varphi_*'/\hat{\varphi}')^4 \right) \right)$$

Following the same matching procedure as was outlined for regions 1 and 3 and 2 and 4, we define a variable η which describes an intermediate region where both the away from axis and near axis expansions are valid. For this case, $O(\epsilon_e^{1/2}) \eta < O(1)$ and therefore for u^2 matching

$$\lim_{\epsilon_e \rightarrow 0} \left(\varphi_{*\eta}^2 \eta^2 - \frac{1}{3} \varphi_{*\eta}^4 \eta^4 + 2\epsilon_e \left(\hat{\varphi}_\eta^2 \eta^2 \frac{4}{3} - \frac{\varphi_{*\eta}^3 \eta^3 - \varphi_{*\eta}^2 \eta^2}{3\hat{\varphi}_\eta} \right) - \epsilon_e \frac{\varphi_{*\eta}^2 \eta^2}{\epsilon_e} - \epsilon_e^2 \left(-\frac{1}{3} \frac{\varphi_{*\eta}^4 \eta^4}{\epsilon_e^2} + 1 - \left(\frac{\varphi_{*\eta}}{\hat{\varphi}_\eta} \right)^4 - 2 \left(\frac{\varphi_{*\eta}^2 \eta^2}{\epsilon_e} - \frac{\hat{\varphi}_\eta^2 \eta^2}{\epsilon_e} - \left(\frac{\hat{\varphi}_\eta^2 \eta^2}{3\epsilon_e} - \frac{\varphi_{*\eta}^3 \eta^2}{3\epsilon_e \hat{\varphi}_\eta} \right) + \frac{1}{2} \left(1 - \left(\frac{\varphi_{*\eta}}{\hat{\varphi}_\eta} \right)^4 \right) \right) \right) \Rightarrow 0$$

Matching is assured for u^2 .

For p we have

$$\begin{aligned} \lim_{\epsilon_c \rightarrow 0} & \left(1 - \epsilon_c/2 - 4\hat{\varphi}_\eta^2 \eta^2/3 + \varphi_{*\eta}^3 \eta^2/3\hat{\varphi}_\eta - \frac{\hat{\varphi}_\eta^2 \eta^2 \epsilon_c}{12} \right. \\ & - \epsilon_c \hat{\varphi}_\eta^2 \eta^2 / M_{\omega_c}^2 \epsilon_c + 4\epsilon_c \varphi_{*\eta} \hat{\varphi}_\eta \eta^2/3 - \epsilon_c \varphi_{*\eta}^4 \eta^2 / 12 \hat{\varphi}_\eta^2 \\ & - \epsilon_c \varphi_{*\eta}^3 \eta^2 / 3 \hat{\varphi}_\eta + \epsilon_c / \epsilon_c M_{\omega_c}^2 - \epsilon_c \varphi_{*\eta}^4 / 2 \hat{\varphi}_\eta^4 + \\ & 2\epsilon_c \varphi_{*\eta}^3 \eta^2 / 3 \hat{\varphi}_\eta^3 - \epsilon_c \varphi_{*\eta}^4 \eta^2 / 2 \hat{\varphi}_\eta^2 - 1 + \epsilon_c/2 + \\ & 4\hat{\varphi}_\eta^2 \eta^2/3 - \epsilon_c \varphi_{*\eta}^3 \eta^2 / 3 \hat{\varphi}_\eta \epsilon_c - \epsilon_c / \epsilon_c M_{\omega_c}^2 + \\ & \left. \epsilon_c \varphi_{*\eta}^4 / 2 \hat{\varphi}_\eta^4 \right) \Rightarrow 0 \end{aligned}$$

Therefore, matching of p to this order is assured.

For ρ we have

$$\begin{aligned} \lim_{\epsilon_c \rightarrow 0} & \left(1 - 4\hat{\varphi}_\eta^2 \eta^2/3 + \varphi_{*\eta}^3 \eta^2/3\hat{\varphi}_\eta - \varphi_{*\eta}^2 \eta^2 (1/M_{\omega_c}^2 \epsilon_c - 1) \right. \\ & + \epsilon_c (-1 + \eta^2 \varphi_\eta^2 (1 - 1/M_{\omega_c}^2 \epsilon_c - 13/12)) + 1/2 + \\ & 4\hat{\varphi}_\eta \varphi_{*\eta} \eta^2/3 - 7\varphi_{*\eta}^4 \eta^2 / \hat{\varphi}_\eta^2 12 - \varphi_{*\eta}^3 \eta^2 / 3 \hat{\varphi}_\eta - \varphi_{*\eta}^4 / 2 \hat{\varphi}_\eta^4 \\ & + 2\varphi_{*\eta}^3 \eta^2 / 3 \hat{\varphi}_\eta + \epsilon_c/2 - \epsilon_c \varphi_{*\eta}^4 / \hat{\varphi}_\eta^4 - 1 - \\ & \varphi_{*\eta}^2 \eta^2 / M_{\omega_c}^2 \epsilon_c - (\varphi_{*\eta}^2 - \hat{\varphi}_\eta^2) \eta^2 + (\hat{\varphi}_\eta^2 \eta^2/3 - \varphi_{*\eta}^3 \eta^2 / 3 \hat{\varphi}_\eta \\ & \left. - \epsilon_c/2 (1 - \varphi_{*\eta}^4 / \hat{\varphi}_\eta^4)) \right) \Rightarrow 0 \end{aligned}$$

Therefore, matching ρ to this order is assured.

Internal Layer - Region 6 Analysis

We start the analysis from the shock relations, which are:

$$\hat{p} = \hat{p}_{\infty i} + \gamma_i \hat{p}_{\infty i} \hat{M}_{\infty i}^2 \sin^2 \hat{\beta} (1 - \hat{\epsilon}) \quad (29.1)$$

$$\hat{p} = \hat{p}_{\infty i} / \hat{\epsilon} \quad (29.2)$$

$$\hat{u} = U_{\infty i} \cos \hat{\beta} \quad (29.3)$$

$$\hat{v} = \hat{\epsilon} U_{\infty i} \sin \hat{\beta} \quad (29.4)$$

$$\hat{\epsilon} = \frac{\gamma_i - 1}{\gamma_i + 1} + \frac{2}{(\gamma_i + 1) \hat{M}_{\infty i}^2 \sin^2 \hat{\beta}} \quad (29.5)$$

Unlike the external uniform stream case $\hat{p}_{\infty i}$, $\hat{M}_{\infty i}$, $\hat{p}_{\infty i}$ are not constants but functions of the undisturbed plume flow. Their functional relationships are determined by the assumed source distribution

$$\hat{p}_{\infty i} = p_{\infty i 0} \frac{\cos^n \frac{\pi \hat{\phi}}{2\theta_{\infty}}}{R^2} \quad (30.1)$$

$$\hat{p}_{\infty i} = p_{\infty i 0} (p_{\infty i} / p_{\infty i 0})^{\gamma_i} \quad (30.2)$$

$$\hat{M}_{\infty i} = \left(\frac{2}{\gamma_i - 1} \left(\frac{\cos^n \frac{\pi \hat{\phi}}{2\theta_{\infty}}}{R^2} \right)^{1-\gamma_i} \left(1 + \frac{\gamma_i - 1}{2\epsilon_{i0}} M_{\infty i 0}^2 \epsilon_{i0} \right) - \frac{2}{\gamma_i - 1} \right)^{1/2} \quad (30.3)$$

where $n = b/(\gamma_i - 1)$

$$\theta_{\infty} = \left(\sqrt{\frac{\gamma_i + 1}{\gamma_i - 1}} - 1 \right) \frac{\pi}{2} - \sqrt{\frac{\gamma_i + 1}{\gamma_i - 1}} \left(\tan^{-1} \sqrt{\frac{\gamma_i - 1}{\gamma_i + 1} (M_{\infty i}^2 - 1)} + \tan^{-1} \sqrt{M_{\infty i}^2 - 1} \right)$$

We now expand the boundary conditions for $\epsilon_{i0} \rightarrow 0, M_{\infty i 0} \rightarrow \infty$ such that

$$\epsilon_{i0} M_{\infty i 0}^2 \rightarrow O(1) \quad . \quad \text{This will then indicate the orders}$$

of magnitude of the variables within the layer near the shock.

It is hoped that the orders of magnitude found for the variables will be valid through to the contact surface. If this is not the case, then the solution based on the orders of magnitude near the shock will break down and a second expansion valid near the contact surface will be required. Expanding the undisturbed plume parameters, we find that

$$n = \left(\frac{\epsilon_{i0} b}{\gamma_i - 1} \right) \frac{1}{\epsilon_{i0}} \sim O\left(\frac{1}{\epsilon_{i0}}\right)$$

$$\theta_{\infty} = \sqrt{\frac{\gamma_i + 1}{\gamma_i - 1} \epsilon_{i0}} \left(1 - \tan^{-1} \sqrt{\frac{\gamma_i - 1}{\gamma_i + 1} (M_{\infty i}^2 - 1)} \right) - \frac{\pi}{2} + \tan^{-1} \sqrt{M_{\infty i}^2 - 1} \sim O\left(\frac{1}{\epsilon_{i0}^{1/2}}\right)$$

When applied to (30.1), (30.2) and (30.3), we obtain

$$\hat{p}_{\infty i} = p_{\infty i0} \frac{\cos^n \frac{\pi \hat{\theta}}{2\theta_{\infty}}}{R^2} \sim O(1) \quad (31.1)$$

$$\hat{p}_{\infty i} = p_{\infty i0} \frac{\cos^n \frac{\pi \hat{\theta}}{2\theta_{\infty}}}{R^2} \sim O(1) \quad (31.2)$$

$$\hat{M}_{\infty i}^2 = \frac{2}{\gamma_i - 1} \left(\frac{\cos^n \frac{\pi \hat{\theta}}{2\theta_{\infty}}}{R^2} \right)^{1-\gamma_i} \left(1 + \frac{\gamma_i - 1}{\epsilon_{i0}^2} M_{\infty i0}^2 \epsilon_{i0} \right) - \frac{2}{\gamma_i - 1} \sim O\left(\frac{1}{\epsilon_{i0}}\right) \quad (31.3)$$

The first order expressions, (31.1), (31.2), and (31.3), are then introduced into the expanded form of the Rankine-Hugoniot relations, (29.1), (29.2), (29.3), (29.4) and (29.5), which then give the order of magnitude results

$$\hat{p} \sim O\left(\frac{1}{\epsilon_{i0}}\right) p_{\infty i0} \quad \hat{p} \sim O(1) p_{\infty i0} U_{\infty i}^2$$

$$\hat{u} \sim O(\theta) U_{\infty i} \quad \hat{v} \sim O(\epsilon_{i0}) U_{\infty i}$$

where θ is the angle the free stream makes with the direction normal to the shock.

At the axis of symmetry, ϵ_{i0} is the density ratio across the shock and is given by $\epsilon_{i0} = \frac{\gamma_i - 1}{\gamma_i + 1} + \frac{1}{M_{\infty i}^2}$. Up to this point, the magnitude of the velocity \hat{u} parallel to the shock has not been determined in terms of ϵ_{i0} ; however, its lower bound can be determined from the condition that the shock layer is of zero thickness in the limit as $\epsilon_{i0} \rightarrow 0$ and, therefore, the flow must be turned 90 degrees upon crossing the shock. The deflection angle is given by

$$\tan \delta = \frac{(\hat{M}_{\infty i}^2 \sin^2 \hat{\beta} - 1) \cot \hat{\beta}}{\frac{\gamma_i + 1}{2} \hat{M}_{\infty i}^2 - (\hat{M}_{\infty i}^2 \sin^2 \hat{\beta} - 1)}$$

where $\hat{\beta} = \frac{\pi}{2} - \theta$ for near normal shock $\theta \ll 1$ $\hat{M}_{\infty i} \gg 1$

$$\tan \delta = \frac{\cos^2 \theta \tan \theta}{\left(\frac{\gamma_i + 1}{2} - \cos^2 \theta\right)} = \frac{\theta}{\frac{\gamma_i + 1}{2} - 1 + \theta^2} \Rightarrow \infty$$

This then yields

$$\lim_{\epsilon_{i0} \rightarrow 0} \frac{\theta}{O\left(\frac{\gamma_i + 1}{2} \epsilon_{i0} + \theta^2\right)} \Rightarrow \infty$$

We can conclude that $\theta > O(\epsilon_{i0})$ and is obviously less than $O(1)$. This result can be written as

$$u = O(\epsilon_{i0}^m) \quad 1 > m > 0$$

The dependent variables can now be expanded in terms of ϵ_{i0} ,

following the first order magnitudes found from the shock relations. The non-dimensionalized expansions will then be:

$$\begin{aligned} p/\rho_{\infty} u_{\infty}^2 &= p_0 + \epsilon_{i_0}^m p_1 + \epsilon_{i_0} p_2 + \dots \\ \rho/\rho_{\infty} &= \rho_0/\epsilon_{i_0} + \epsilon_{i_0}^{m-1} \rho_1 + \epsilon_{i_0}^{2m-1} \rho_2 + \dots \\ u/u_{\infty} &= \epsilon_{i_0}^m u_0 + \epsilon_{i_0}^{2m} u_1 + \epsilon_{i_0}^{3m} u_2 + \dots \\ v/u_{\infty} &= \epsilon_{i_0} v_0 + \epsilon_{i_0}^{m+1} v_1 + \epsilon_{i_0}^{2m+1} v_2 + \dots \end{aligned}$$

It is assumed that x will be of order one, from geometry, and y will depend on ϵ_{i_0} to some power n' . The unknown powers m and n' will be determined by requiring that the governing equations, when written in terms of ϵ_{i_0} , yield a physically reasonable non-trivial system of equations. The governing equations are:

$$\begin{aligned} \frac{\partial \rho v_r}{\partial x} + \frac{\partial \rho v_r H}{\partial y} &= 0 && \text{continuity} \\ u \frac{\partial u}{\partial x} + H v \frac{\partial u}{\partial y} - \kappa u v + \frac{1}{\rho} \frac{\partial p}{\partial x} &= 0 && x \text{ momentum} \\ u \frac{\partial v}{\partial x} + H v \frac{\partial v}{\partial y} + \kappa u^2 + \frac{H}{\rho} \frac{\partial p}{\partial y} &= 0 && y \text{ momentum} \\ u \frac{\partial p/\rho^\gamma}{\partial x} + H v \frac{\partial p/\rho^\gamma}{\partial y} &= 0 && \text{energy} \end{aligned}$$

where κ is the radii of curvature of the shock surface and $H = 1 - \kappa y$ is the ratio of the radius of curvature of a constant y surface, with respect to the shock curvature at a given value of x .

Substituting the expansions into the governing equations, we obtain the following results relating the unknowns m and n' :

$$\begin{aligned} \frac{\partial p_0}{\partial x} &= O(\epsilon_{i_0}^{2m-1}) && x \text{ momentum} \\ y &= O(\epsilon_{i_0}^{n'}) = O(\epsilon_{i_0}^m) && y \text{ momentum} \\ \epsilon_{i_0}^m &= O(\epsilon_{i_0}^{1-n'}) && \text{continuity} \end{aligned}$$

Applying the source condition $\frac{\partial p_0}{\partial x} = O(1)$ we find that $m = \frac{1}{2}$. It then follows that $n' = \frac{1}{2}$ from the other two relationships. Since $\theta = \frac{\pi}{2} - \beta$ is now found to be proportional to $\epsilon_{i_0}^{1/2}$, then in the limit as $\epsilon_{i_0} \rightarrow 0$, β must equal $\pi/2$. The shock surface is then a spherical shell which is centered at the jet exit. The magnitude of the perturbation from this spherical shell will then be derived by the use of the known value of $\theta = O(\epsilon_{i_0}^{1/2})$. The radius can be written as $R = 1 + G(x)$. From this, the value of θ can be calculated $R'(x) = G'(x) = \epsilon_{i_0}^{1/2} \theta$. The magnitude of $G(x)$ is then $O(\epsilon_{i_0}^{1/2})$ which then leads to the result $R(x) = 1 + F(x) \epsilon_{i_0}^{1/2}$. This will be the form used for $R(x)$. With the values of m and n' established the expansions are

$$\begin{aligned} \bar{p} &= p_0 + p_1 \epsilon_{i_0}^{1/2} + p_2 \epsilon_{i_0} + \dots \\ \bar{\rho} &= \rho_0 / \epsilon_{i_0} + \rho_1 / \epsilon_{i_0}^{1/2} + \rho_2 + \dots \\ \bar{u} &= \epsilon_{i_0}^{1/2} u_0 + \epsilon_{i_0} u_1 + \epsilon_{i_0}^{3/2} u_2 + \dots \\ \bar{v} &= \epsilon_{i_0} v_0 + \epsilon_{i_0}^{3/2} v_1 + \epsilon_{i_0}^2 v_2 + \dots \\ \bar{y} &= \epsilon_{i_0}^{1/2} y \quad \bar{x} = x \end{aligned}$$

The flow equations become considerably simplified for integration across the layer if they are written in terms of the Mises variables α, Ψ .

The distance downstream is α and Ψ is the streamfunction.

The flow equations in this coordinate system are

$$Hr \frac{\partial p}{\partial \Psi} = \kappa u + \frac{\partial v}{\partial \alpha} \quad (32.1) \text{ } y \text{ momentum equation}$$

$$\frac{u^2 + v^2}{2} + \frac{r_i}{r-1} \frac{p}{\rho} = C(\Psi) \quad (32.2) \text{ integrated } \alpha \text{ momentum}$$

$$p/\rho^\gamma = D(\Psi) \quad (32.3) \text{ energy equation}$$

$$\frac{\partial y}{\partial \Psi} = -\frac{1}{\rho u r} \quad (32.4) \text{ streamfunction definitions which satisfies continuity directly}$$

$$H = 1 - \kappa y$$

$$\frac{\partial y}{\partial \alpha} = H \frac{v}{u} \quad (32.5)$$

After substitution of these expansions and introducing an expansion for y and r in terms of α and Ψ and collecting terms of like order, we then develop the following system of equations.

First Order Expressions

Momentum equation across layer

$$\frac{\partial p_0}{\partial \Psi} = 0 \quad (33.1)$$

Integrated momentum equation

$$u_0^2 = u_{0*}^2 - \frac{2p_{0*}}{\rho_{0*}} \ln \frac{p_0}{p_{0*}} \quad (33.2)$$

Integrated energy equation

$$p_0 = p_0 \quad (33.3)$$

Definitions of streamfunction equations

$$\frac{\partial y_0}{\partial \psi} = - \frac{1}{\rho_0 u_0 r_0} \quad (33.4)$$

Definition of streamfunction

$$\frac{\partial y_0}{\partial x} = \frac{v_0}{u_0} \quad (33.5)$$

For the second order results, we obtain for the momentum equation across layer

$$\frac{\partial p_1}{\partial \psi} = \frac{\kappa_0 u_0}{r_0} \quad (34.1)$$

Integrated momentum equation

$$2u_0 u_1 = 2u_{0*} u_{1*} - \frac{2p_{0*} p_1}{\rho_{0*} p_0} \quad (34.2)$$

Integrated energy equation

$$p_1 = \rho_1 \quad (34.3)$$

Definition of streamfunction equations

$$\frac{\partial y_1}{\partial \psi} = \frac{1}{\rho_0 u_0 r_0} \left(\frac{p_1}{\rho_0} + \frac{u_1}{u_0} + \frac{r_1}{r_0} \right) \quad (34.4)$$

Definition of streamfunction

$$\frac{\partial y_1}{\partial x} = \kappa_0 y_0 \frac{v_0}{u_0} + \frac{v_1}{u_0} - \frac{v_0 u_1}{u_0^2} \quad (34.5)$$

For the third order results, we obtain momentum equation across layer

$$\frac{\partial p_1}{\partial \psi} = \frac{\kappa_0 u_1}{r_0} + \frac{1}{r_0} \frac{\partial v_0}{\partial x} + \frac{u_0 \kappa_0}{r_0^2} (r_0 \kappa_0 y_0 - r_1) \quad (35.1)$$

Integrated momentum equation

$$u_1^2 + 2u_1 u_0 + v_0^2 = 2u_{1*} u_{0*} + u_{1*}^2 + (35.2)$$

$$v_{0*}^2 + \frac{2\rho_{0*} \rho_{2*}}{\rho_{0*}^2} \ln \frac{\rho_0}{\rho_{0*}} - \frac{2\rho_{2*}}{\rho_{0*}} \ln \frac{\rho_0}{\rho_{0*}} -$$

$$2 \frac{\rho_{0*}}{\rho_{0*}} \left(\frac{p_1}{\rho_0} - \frac{p_{2*}}{\rho_{0*}} \right) - \frac{\gamma_0 - 1}{\epsilon_{i0}} \left(\ln \frac{\rho_0}{\rho_{0*}} \right)^2$$

Integrated energy equation

$$\frac{p_2}{p_0} - \frac{p_1 p_2}{\rho_0^2} - \frac{p_2}{\rho_0} + \left(\frac{p_2}{\rho_0}\right)^2 = \frac{p_{2*}}{\rho_{0*}} - \frac{p_{2**}}{\rho_{0**}} + \frac{\gamma_i - 1}{2\epsilon_{i0}} \left(\ln \frac{p_2}{\rho_{0**}}\right)^2 \quad (35.3)$$

Definitions of streamfunction

$$\frac{\partial y_2}{\partial \psi} = -\frac{1}{\rho_0 u_0 r_0} \left(-\left(\frac{p_2}{\rho_0} + \frac{u_2}{u_0} + \frac{r_2}{r_0} + \frac{p_2 r_2}{\rho_0 r_0} + \frac{p_2 u_2}{\rho_0 u_0} + \frac{u_2 r_2}{u_0 r_0}\right) + \left(\frac{p_2}{\rho_0} + \frac{r_2}{r_0} + \frac{u_2}{u_0}\right)^2 \right) \quad (35.4)$$

We must apply the expanded shock boundary conditions to the outer edge of the layer. In the limit as $\epsilon_{i0} \rightarrow 0$, $M_{\infty i0} \rightarrow \infty$ such that $\epsilon_{i0} M_{\infty i0}^2 \rightarrow O(1)$ we obtain

First order results

$$\hat{p}_0 = \cos^n \frac{\pi \hat{\phi}}{2\theta_\infty} \quad (36.1)$$

$$\hat{\rho}_0 = \cos^n \frac{\pi \hat{\phi}}{2\theta_\infty} \quad (36.2)$$

$$\hat{u}_0 = F'(\hat{\phi}) \quad (36.3)$$

$$\hat{v}_0 = 1 \quad (36.4)$$

$$\hat{y}_0 = 0 \quad (36.5)$$

Second order results

$$\hat{p}_1 = -2F \cos^n \frac{\pi \hat{\phi}}{2\theta_\infty} \quad (37.1)$$

$$\hat{\rho}_1 = -2F \cos^n \frac{\pi \hat{\phi}}{2\theta_\infty} \quad (37.2)$$

$$\hat{u}_1 = -F'F \quad (37.3)$$

$$\hat{y}_1 = 0 \quad (37.4)$$

Third order results

$$\hat{p}_2 = \cos^n \frac{\Pi \hat{\phi}}{2\theta_\infty} \left(3F^2 - 1 - F'^2 + \frac{1}{M_{\infty i_0}^2 \epsilon_{i_0}} \right) \quad (38.1)$$

$$\hat{p}_2 = \cos^n \frac{\Pi \hat{\phi}}{2\theta_\infty} \left(3F^2 + \frac{1}{M_{\infty i_0}^2 \epsilon_{i_0}} \left(1 + \frac{2\epsilon_{i_0}}{(\gamma_i - 1) M_{\infty i_0}^2} \right) \chi \right. \\ \left. b^2 \hat{\phi}^2 (\gamma_i - 1) / 4\epsilon_{i_0} - F'^2 \right) \quad (38.2)$$

$$\hat{u}_2 = FF' - F'^3/6 \quad (38.3)$$

$$\hat{y}_2 = 0 \quad (38.4)$$

Before we integrate the equations, we introduce another transformation of the independent variable Ψ . This variable describes the streamfunction in terms of the position at which the streamline has crossed the shock. It is defined from the source conditions as:

$$\Psi = \int_0^{\varphi_*} \cos^n \frac{\Pi \varphi_*}{2\theta_\infty} \sin \varphi_* d\varphi_* \quad (39.1)$$

A point within the layer will then be described by the coordinates $(\hat{\phi}, \varphi_*)$. Substituting (36.1 to 39.1) in the equations (33.1 to 35.4) and integrating across the layer we obtain

First order system

$$p_0 = \cos^n \frac{\pi \hat{\phi}}{2\theta_\infty} \quad (40.1)$$

$$\rho_0 = \cos^n \frac{\pi \hat{\phi}}{2\theta_\infty} \quad (40.2)$$

$$u_0 = (F'^2 - 2 \ln p_0 / p_{0*})^{1/2} \quad (40.3)$$

$$y_0 = \frac{1}{\rho_0 r_0} \int_{\phi_*}^{\hat{\phi}} \cos^n \frac{\pi \phi_*}{2\theta_\infty} \frac{\sin \phi_* d\phi_*}{u_0} \quad (40.4)$$

$$v_0 = u_0 \frac{\partial y_0}{\partial \hat{\phi}} \quad (40.5)$$

Second order system

$$p_1 = -2F \cos^n \frac{\pi \hat{\phi}}{2\theta_\infty} + \frac{\kappa}{r_0} \int_{\phi_*}^{\hat{\phi}} u_0 \cos^n \frac{\pi \phi_*}{2\theta_\infty} \sin \phi_* d\phi_* \quad (41.1)$$

$$u_1 = \frac{1}{2u_0} (-2F'^2 F - 2p_1 / p_0) \quad (41.2)$$

$$p_1 = p_1 \frac{\partial}{\partial \hat{\phi}} \quad (41.3)$$

$$y_1 = \frac{1}{\rho_0 r_0} \int_{\phi_*}^{\hat{\phi}} \cos^n \frac{\pi \phi_*}{2\theta_\infty} \frac{\sin \phi_* d\phi_*}{u_0} \left(\frac{p_1}{p_0} + \frac{u_1}{u_0} + \frac{r_1}{r_0} \right) \quad (41.4)$$

$$v_1 = u_0 \left(\frac{\partial y_1}{\partial \hat{\phi}} - \frac{\kappa y_0 v_0}{u_0} + \frac{v_0 u_1}{u_0^2} \right) \quad (41.5)$$

Third order system

$$p_2 = \cos^n \frac{\pi \hat{\phi}}{2\theta_\infty} (3F^2 - 1 - F'^2 + \quad (42.1)$$

$$\frac{1}{M_{\infty}^2 \epsilon_{i0}}) + \int_{\phi_*}^{\hat{\phi}} \left(\frac{\kappa u_1}{r_0} + \frac{1}{r_0} \frac{\partial v_0}{\partial \hat{\phi}} + \frac{u_0 \kappa}{r_0^2} \chi \right.$$

$$\left. (r_0 \kappa y_0 - r_2) \right) \cos^n \frac{\pi \phi_*}{2\theta_\infty} \sin \phi_* d\phi_*$$

$$\rho_2 = \rho_0 \left(P_2/P_0 - P_1 \rho_1 / \rho_0^2 + (\rho_1 / \rho_0)^2 - \left(P_{2*} / P_{0*} - \rho_{2*} / \rho_{0*} + \frac{\delta_i - 1}{\epsilon_i} \ln \frac{P_0}{P_{0*}} \right) \right) \quad (42.2)$$

$$u_2 = 1/2 u_0 \left(2 u_{2*} u_{0*} + u_{1*}^2 + v_{0*}^2 - u_1^2 - v_0^2 + (2 \rho_{0*} / \rho_0^2) \rho_{2*} \ln P_0 / P_{0*} - 2 \rho_{2*} / \rho_{0*} \ln P_0 / P_{0*} - (42.3) \right. \\ \left. 2 \rho_{0*} / \rho_{0*} (P_2 / P_0 - P_{2*} / P_{0*}) - \frac{\delta_i - 1}{\epsilon_i} (\ln P_0 / P_{0*})^2 \right)$$

$$y_2 = 1/r_0 \rho_0 \int_{\varphi_*}^{\hat{\varphi}} \frac{\cos^n \frac{\pi \varphi_*}{2\theta_{\infty}} \sin \varphi_* d\varphi_*}{u_0} \left(- \left(\frac{\rho_2}{\rho_0} + \frac{u_2}{u_0} + \frac{r_2}{r_0} + \frac{\rho_1 r_1}{\rho_0 r_0} + \frac{\rho_1 u_1}{\rho_0 u_0} + \frac{u_1 r_1}{u_0 r_0} \right) + \left(\frac{\rho_1}{\rho_0} + \frac{u_1}{u_0} + \frac{r_1}{r_0} \right)^2 \right) \quad (42.4)$$

Examining the above integrals, we note that the calculated variables remain finite and non-zero from the vicinity of the shock through to the contact surface. This indicates that the solution is uniformly valid. We now must examine the behavior of the solution as we approach the axis of symmetry. This is important since in order to evaluate the matching of the shock layers we must determine the initial radius of curvature of the shock surface, as well as

its position in space. This requires that we know both layer thickness and contact surface pressure in an analytic form so that the matching of contact surface pressure and position can be determined. For the case when $R(x) = 1.0$ the variables can be expanded in even powers of φ near the axis, and then integrated across the layer. These results will then be used to illustrate the change in order of magnitude of some of the dependent variables near the axis of symmetry.

From the source conditions, we can write for small φ_* , $\hat{\varphi}$

$$\hat{p}_0 = \hat{f}_0 = 1 - n\left(\frac{\pi}{2\theta_\infty}\right)^2 \hat{\varphi}^2$$

which then leads to the first order results

$$p_0 = f_0 = 1 - n\left(\frac{\pi}{2\theta_\infty}\right)^2 \hat{\varphi}^2$$

$$u_0 = \left(n\left(\frac{\pi}{2\theta_\infty}\right)^2 (\hat{\varphi}^2 - \varphi_*^2) \right)^{1/2}$$

$$y_0 = \left(\frac{1}{n} \left(\frac{2\theta_\infty}{\pi} \right)^2 (1 - (\varphi_*/\hat{\varphi})^2) \right)^{1/2}$$

$$v_0 = (\varphi_*/\hat{\varphi})^2$$

The second order results then become

$$p_1 = \frac{\sqrt{n}}{3\theta_\infty} \frac{\pi}{2\theta_\infty} (\hat{\varphi}^2 - \varphi_*^2)^{3/2}$$

$$f_1 = \frac{\sqrt{n}}{3\theta_\infty} \frac{\pi}{2\theta_\infty} (\hat{\varphi}^2 - \varphi_*^2)^{3/2}$$

$$u_1 = 1/3 \hat{\varphi} (\hat{\varphi}^2 - \varphi_*^2)$$

It can be seen that as we approach the axis $\varphi_*, \hat{\varphi} \rightarrow O(\epsilon_{i_0}^{1/2})$
and

$$u \approx \epsilon_{i_0}^{1/2} u_0 \approx O(\epsilon_{i_0})$$

$$v \approx \epsilon_{i_0} v_0 \approx O(\epsilon_{i_0})$$

$$p \approx p_0 + \epsilon_{i_0} p_1 \approx 1 + O(\epsilon_{i_0})$$

$$\rho \approx \rho_0/\epsilon_{i_0} + \rho_1/\epsilon_{i_0}^{1/2} \approx O(1/\epsilon_{i_0}) + O(1)$$

$$x \approx O(\epsilon_{i_0}^{1/2}) \quad y \approx O(\epsilon_{i_0}^{1/2})$$

The change in orders of magnitude of the variables then necessitates that a new expansion procedure be applied. To first order p, ρ and v do not change; however, u and x are altered and the new expansions must reflect this.

Internal Layer - Region 5 Analysis

The shock position in this region is described by an expansion in terms of even powers of $\hat{\phi}$ away from the axis; i.e.,

$$R = 1 + a_1 \epsilon_{i0} \hat{\phi}^2 + a_2 \epsilon_{i0}^2 \hat{\phi}^4 + \dots$$

Based once again on the shock relations, we can expand the dependent variables in the form

$$u = \epsilon_{i0} \bar{u}_0 + \epsilon_{i0}^3 \bar{u}_1 + \dots$$

$$v = \epsilon_{i0} \bar{v}_0 + \epsilon_{i0}^3 \bar{v}_1 + \dots$$

$$p = \bar{p}_0 + \epsilon_{i0} \bar{p}_1 + \dots$$

$$\rho = \bar{\rho}_0 / \epsilon_{i0} + \bar{\rho}_1 + \dots$$

$$x = \bar{x} \epsilon_{i0}^{1/2} \quad y = \bar{y} \epsilon_{i0}^{1/2}$$

Substituting the above in the governing equations, we obtain the first order system

$$\frac{\partial \bar{u}_0 \bar{\rho}_0}{\partial \bar{x}} + \frac{\partial \bar{v}_0 \bar{\rho}_0}{\partial \bar{y}} = 0$$

$$\bar{\rho}_0 = \bar{p}_0 = 1$$

$$\bar{u}_0 \frac{\partial \bar{u}_0}{\partial \bar{x}} + \bar{v}_0 \frac{\partial \bar{u}_0}{\partial \bar{y}} + \frac{1}{\bar{\rho}_0} \frac{\partial \bar{p}_1}{\partial \bar{x}} = 0$$

$$\bar{u}_0 \frac{\partial \bar{v}_0}{\partial \bar{x}} + \bar{v}_0 \frac{\partial \bar{v}_0}{\partial \bar{y}} + \frac{1}{\bar{\rho}_0} \frac{\partial \bar{p}_1}{\partial \bar{y}} = 0$$

These are of the same form as the constant density flow equations.

We therefore apply a constant density flow solution method to this first order system. A streamfunction is defined which will satisfy the continuity equation identically. This is

$$\frac{\partial \bar{\Psi}}{\partial y} = -\bar{r}_0 \bar{u}_0 \quad \frac{\partial \bar{\Psi}}{\partial x} = \bar{r}_0 \bar{v}_0$$

If $\bar{\Psi}$ is known throughout the layer, then \bar{u}_0 and \bar{v}_0 can be calculated. The equation for $\bar{\Psi}$ to this order of approximation is

$$\frac{\partial}{\partial x} \left(\frac{\bar{\Psi}}{x} \right) + \frac{\partial}{\partial y} \left(\frac{\bar{\Psi}}{x^2 y} \right) = -\bar{\xi}$$

Where $\bar{\xi}$ is the vorticity within the layer. For an incompressible flow, the circulation must remain constant throughout the flow region and this leads to the constancy of the product of vorticity and distance away from the axis. Noting this, we can then develop the vorticity inside the layer in terms of its value at the shock and its radial position within the flow. The result is

$$\bar{\xi} = \bar{\xi}_s \frac{\bar{r}_0}{\bar{r}} = - \left(\eta \left(\frac{\Pi}{2\theta_\infty} \right)^2 + 4a_i \right) \bar{\phi} \bar{r}$$

The equation that must be solved is then

$$\bar{\phi} \frac{\partial}{\partial \bar{\phi}} \left(\frac{\bar{\Psi}}{\bar{\phi}} \right) + \frac{\partial^2 \bar{\Psi}}{\partial \bar{y}^2} = - \left(\eta \left(\frac{\Pi}{2\theta_\infty} \right)^2 + 4a_i \right) \bar{\phi}^{-2} \quad (43.1)$$

Substituting in a streamfunction of the form

$$\bar{\Psi} = A\bar{\phi}^2\bar{y}^2 + B\bar{\phi} + C\bar{\phi}^2 + D\bar{y} + E\bar{y}^2 + F + G\bar{\phi}^2\bar{y} \quad (44.1)$$

we find from (43.1) that

$$A = -\frac{1}{2} \left(n \left(\frac{\Pi}{2\theta_\infty} \right)^2 + 4a_i \right)$$

From the definition of the streamfunction we have

$$\frac{\partial \bar{\Psi}}{\partial \bar{\phi}} = \bar{r}_0 \bar{v}_0 \quad (45.1)$$

$$\frac{\partial \bar{\Psi}}{\partial \bar{y}} = -\bar{r}_0 \bar{u}_0 \quad (45.2)$$

From (45.1) we find

$$-\left(n \left(\frac{\Pi}{2\theta_\infty} \right)^2 + 4a_i \right) \bar{\phi} \bar{y}_0^2 + 2C\bar{\phi} + 2G\bar{\phi} \bar{y}_0 = \bar{r}_0 \bar{v}_0 \quad (46.1)$$

At $\bar{y}_0 = 0$ which is the shock surface, we have $\bar{v}_0 = 1$

which then gives from (46.1) $C = 1/2$

From (45.2) we find $-\left(n \left(\frac{\Pi}{2\theta_\infty} \right)^2 + 4a_i \right) \bar{\phi}^2 \bar{y} + D + G\bar{\phi}^2 = -\bar{r}_0 \bar{u}_0$

at the shock $\bar{y}_0 = 0$ $\bar{u}_0 = 2a_i \bar{\phi}$ and from (47.1)

we obtain

$$D = 0 \quad G = -2a_i$$

These results then give us the first order velocity components in this region.

$$\bar{v}_0 = 1 - 4ai\bar{y} - \left(n\left(\frac{\pi}{2\theta_\infty}\right)^2 + 4ai\right)\bar{y}^2 \quad (48.1)$$

$$\bar{u}_0 = \bar{\phi} \left(\left(n\left(\frac{\pi}{2\theta_\infty}\right)^2 + 4ai\right)\bar{y} + 2ai \right) \quad (48.2)$$

and $\rho_0 = \rho_0 = 1$

The normal coordinate \bar{y} to first order as a function of $\bar{\phi}_*$ and $\bar{\phi}$ can now be calculated from

$$\frac{\partial \bar{y}_0}{\partial \bar{\phi}} = \frac{\bar{v}_0}{\bar{u}_0} \quad (49.1)$$

Substituting in \bar{v}_0 and \bar{u}_0 in (49.1) and integrating, we obtain after applying the shock boundary conditions

$$1 - 4ai\bar{y}_0 - \left(n\left(\frac{\pi}{2\theta_\infty}\right)^2 + 4ai\right)\bar{y}_0^2 = \left(\bar{\phi}_*/\bar{\phi}\right)^2$$

or

$$\bar{y}_0 = \frac{-4ai + \sqrt{16a^2i^2 - 4\left(n\left(\frac{\pi}{2\theta_\infty}\right)^2 + 4ai\right)\left(\left(\frac{\bar{\phi}_*}{\bar{\phi}}\right)^2 - 1\right)}}{2\left(n\left(\frac{\pi}{2\theta_\infty}\right)^2 + 4ai\right)} \quad (50.1)$$

The pressure field can now be calculated from the known velocity field given by (48.1) and (48.2). We must integrate the streamwise momentum equation to obtain the variation of pressure along the streamlines with velocity. This result is

$$\bar{u}_0^2 + \bar{v}_0^2 = \bar{u}_{0*}^2 + \bar{v}_{0*}^2 - 2(\bar{p}_1 - \bar{p}_{1*}) \quad (51.1)$$

From the shock relations

$$\bar{p}_{1*} = \frac{1}{M_{\omega_{i_0}}^2 \epsilon_{i_0}} - \left(\frac{n}{2} \left(\frac{\pi}{2\theta_{\infty}} \right)^2 + 2ai \right) \bar{\phi}^2 - 1$$

Applying this to (51.1), we then obtain

$$\begin{aligned} \bar{p}_1 = & -1/2 + 1/M_{\omega_{i_0}}^2 \epsilon_{i_0} - \bar{\phi}^2/2 \left(\left(n \left(\frac{\pi}{2\theta_{\infty}} \right)^2 + 4ai \right) \bar{y}_0 + 2ai \right)^2 \\ & - \left(1 - 4ai \bar{y}_0 - \left(n \left(\frac{\pi}{2\theta_{\infty}} \right)^2 + 4ai \right) \bar{y}_0^2 \right)^2/2 \quad (52.1) \end{aligned}$$

From the conservation of entropy along streamlines relationship, we also have

$$\bar{p}_1 = \bar{p}_1 - \bar{p}_{1*} + \bar{p}_{1*} \quad (53.1)$$

Making use of the value of $\bar{p}_1 - \bar{p}_{1*}$ and noting from the shock relations that $\bar{p}_{1*} = - \left(\frac{n}{2} \left(\frac{\pi}{2\theta_{\infty}} \right)^2 + 2ai \right) \bar{\phi}_*^2$ we can then write for (53.1)

$$\begin{aligned} \bar{p}_1 = & 2ai^2 \bar{\phi}_*^2 - \left(1 - 4ai \bar{y}_0 - \left(n \left(\frac{\pi}{2\theta_{\infty}} \right)^2 + 4ai \right) \bar{y}_0^2 \right)^2/2 \\ & - \bar{\phi}^2 \left(\left(n \left(\frac{\pi}{2\theta_{\infty}} \right)^2 + 4ai \right) \bar{y}_0 + 2ai \right)^2/2 + 1/2 - \\ & \left(\frac{n}{2} \left(\frac{\pi}{2\theta_{\infty}} \right)^2 + 2ai \right) \bar{\phi}_*^2 \end{aligned}$$

The complete expansions for the dependent variables in the near axis region can now be written

$$u = \epsilon_{i_0} \bar{u}_0 + O(\epsilon_{i_0}^3) \quad (55.1)$$

$$v = \epsilon_{i_0} \bar{v}_0 + O(\epsilon_{i_0}^3) \quad (55.2)$$

$$\begin{aligned}
\rho &= 1 + \epsilon_{i0} \left(-\frac{1}{2} + \frac{1}{M_{\infty i0}^2 \epsilon_{i0}} - \frac{\bar{\Phi}^2}{2} \left(\left(n \left(\frac{\pi}{2\theta_{\infty}} \right)^2 + 4ai \right) \bar{y}_0 + 2ai \right)^2 \right. \\
&\quad \left. - \left(1 - 4ai \bar{y}_0 - \left(n \left(\frac{\pi}{2\theta_{\infty}} \right)^2 + 4ai \right) \bar{y}_0^2 \right)^2 + O(\epsilon_{i0}^2) \right) \\
\rho &= 1/\epsilon_{i0} + 2ai^2 \bar{\Phi}_*^2 - \left(1 - 4ai \bar{y}_0 - \left(n \left(\frac{\pi}{2\theta_{\infty}} \right)^2 + 4ai \right) \bar{y}_0^2 \right)^2 / 2 \\
&\quad - \bar{\Phi}^2 \left(\left(n \left(\frac{\pi}{2\theta_{\infty}} \right)^2 + 4ai \right) \bar{y}_0 + 2ai \right)^2 / 2 + 1/2 - \\
&\quad \left(\frac{n}{2} \left(\frac{\pi}{2\theta_{\infty}} \right)^2 + 2ai \right) \bar{\Phi}_*^2 + O(\epsilon_{i0}) \quad (55.4)
\end{aligned}$$

These variables in the limit as $\bar{\Phi}, \bar{\Phi}_*$ tend to infinity must match the variables obtained from the equations away from the axis as the variables $\hat{\Phi}, \hat{\Phi}_*$ vanish. If matching is achieved, then we have proof that the expansion for the region near the axis was the correct one. Since in this analysis a composite expansion for the near and far away from the axis regions is not sought, then a matching of the solutions for a special case will be adequate to indicate the correctness of the expansions and will be easier to perform than a general matching procedure. The special case chosen is that for a spherical shock. For this case $ai = 0$ and the inner expansions can be written as

$$\rho = 1 - \frac{\epsilon_{i0}}{2} - \epsilon_{i0} \left(n \left(\frac{\pi}{2\theta_{\infty}} \right)^2 \frac{\bar{\Phi}^2 \bar{y}_0^2}{2} + \left(1 - n \left(\frac{\pi}{2\theta_{\infty}} \right)^2 \bar{y}_0^2 \right) \frac{1}{2} - \frac{n \left(\frac{\pi}{2\theta_{\infty}} \right)^2 \bar{\Phi}_*^2}{2} \right) \quad (56.1)$$

$$\rho = \frac{1}{\epsilon_{i0}} + \frac{1}{2} \left(1 - \left(1 - n \left(\frac{\pi}{2\theta_{\infty}} \right)^2 \bar{y}_0^2 \right)^2 \right) - \frac{\bar{\Phi}^2}{2} \left(n \left(\frac{\pi}{2\theta_{\infty}} \right)^2 \bar{y}_0 \right)^2 - \frac{n \left(\frac{\pi}{2\theta_{\infty}} \right)^2 \bar{\Phi}_*^2}{2} \quad (56.2)$$

$$u = \epsilon_{i0} n \left(\frac{\pi}{2\theta_{\infty}} \right)^2 \bar{\Phi} \bar{y}_0 + O(\epsilon_{i0})^2 \quad (56.3)$$

$$v = \epsilon_{i0} \left(1 - n \left(\frac{\pi}{2\theta_{\infty}} \right)^2 \bar{y}_0^2 \right) + O(\epsilon_{i0})^2 \quad (56.4)$$

For the away from axis region, we have the following equations for small $\hat{\phi}, \varphi_*$

$$p = 1 - \frac{\eta}{2} \left(\frac{\pi}{2\theta_\infty} \right)^2 \hat{\phi}^2 + O(\epsilon_{i_0}) \quad (57.1)$$

$$\rho = \left(1 - \frac{\eta}{2} \left(\frac{\pi}{2\theta_\infty} \right)^2 \hat{\phi}^2 \right) / \epsilon_{i_0} + O(\epsilon_{i_0}^{1/2}) \quad (57.2)$$

$$u = \epsilon_{i_0}^{1/2} \frac{\sqrt{\eta}}{2} \left(\frac{\pi}{2\theta_\infty} \right) \hat{\phi} \left(1 - (\varphi_*/\hat{\phi})^2 \right)^{1/2} + O(\epsilon_{i_0}) \quad (57.3)$$

$$v = \epsilon_{i_0} (\varphi_*/\hat{\phi})^2 + O(\epsilon_{i_0}^{3/2}) \quad (57.4)$$

Following the same matching procedure as that for the external layer flow, we define a variable η which describes an intermediate region where both the away from axis and near axis expansions are valid.

Since $\hat{\phi} = O(1)$ and $\hat{\psi} = O(\epsilon_{i_0}^{1/2})$ then $O(\epsilon_{i_0}^{1/2}) < \eta < O(1)$

In this region, we have

$$\hat{\phi} = \eta \hat{\phi}_\eta \quad \hat{\psi} = \eta \hat{\psi}_\eta / \epsilon_{i_0}^{1/2}$$

then $\lim_{\epsilon_{i_0} \rightarrow 0} \hat{\phi} \rightarrow 0$ and $\lim_{\epsilon_{i_0} \rightarrow 0} \hat{\psi} \rightarrow \infty$

Applying the above limiting procedure in the region of common validity, we must have

$$\lim_{\substack{\epsilon_{i_0} \rightarrow 0 \\ \varphi_\eta \text{ fixed}}} (f_o - f_i) \rightarrow 0$$

Where f_o and f_i denotes the various expansions for the variables for the outer and inner region respectively.

Matching v

$$\lim_{\epsilon_{i0} \rightarrow 0} \left(\epsilon_{i0} \left(\frac{\Phi_{*n}}{\hat{\Phi}_n} \right)^2 - \epsilon_{i0} \left(1 - n \left(\frac{\pi}{2\theta_{\infty}} \right)^2 \bar{y}_0^2 \right)^{1/2} \right)$$

In the intermediate region, it is known that

$$\bar{y}_0^2 = \frac{1}{n} \left(\frac{2\theta_{\infty}}{\pi} \right)^2 \left(1 - \left(\frac{\Phi_{*n}}{\hat{\Phi}_n} \right)^2 \right)$$

Therefore the above is zero in the limit, assuring matching.

Matching u we can write

$$\lim_{\epsilon_{i0} \rightarrow 0} \left(\epsilon_{i0} n \left(\frac{\pi}{2\theta_{\infty}} \right)^2 \frac{\hat{\Phi}_n \bar{y}_0 \eta}{\epsilon_{i0}^{1/2}} - \epsilon_{i0}^{1/2} \frac{\sqrt{n}}{2} \left(\frac{\pi}{2\theta_{\infty}} \right) \hat{\Phi}_n \eta \left(1 - \left(\frac{\Phi_{*n}}{\hat{\Phi}_n} \right)^2 \right)^{1/2} \right)$$

Again, making use of the expression for \bar{y}_0 we obtain matching for u .

Matching p

$$\lim_{\epsilon_{i0} \rightarrow 0} \left(1 - \frac{n \left(\frac{\pi}{2\theta_{\infty}} \right)^2 \hat{\Phi}_n^2 \eta^2}{2} - \left(1 - \frac{\epsilon_{i0}}{2} - \epsilon_{i0} \left(n \left(\frac{\pi}{2\theta_{\infty}} \right)^2 \frac{\hat{\Phi}_n^2 \eta^2 \bar{y}_0^2}{\epsilon_{i0}} \right) \right. \right. \\ \left. \left. + \frac{\left(1 - n \left(\frac{\pi}{2\theta_{\infty}} \right)^2 \bar{y}_0^2 \right)}{2} - \frac{n \left(\frac{\pi}{2\theta_{\infty}} \right)^2 \Phi_{*n}^2 \eta^2 \epsilon_{i0}}{\epsilon_{i0}} \right)$$

Introducing y_0 again, we then achieve matching for p .

The above matching process has demonstrated the correctness of the near axis expansion. We now use the more general expansions, (55.1 to 55.4) to determine the layer thickness and contact surface pressure distribution near the axis. The results are .

$$\begin{aligned}
y = & \epsilon_{i0}^{1/2} \left(\sqrt{16a_i^2 + 4(4a_i + n(\frac{\pi}{2\theta_{00}})^2) - 4a_i} \right) 2/B^2 - \epsilon_{i0}(1-2a_i)(4a_i((c^2-1)^{1/2} - c) \\
& + B/2) 2/B^2 b - \frac{\epsilon_{i0}^{3/2}}{b} \left(\frac{1}{2}(c - (c^2-1)^{1/2}) - \left(\frac{a_i^2 8\sqrt{2}}{B^2} + \sqrt{\frac{1}{2}} \right)^2 (c - (c^2-1)^{1/2}) + \right. \\
& (4a_i^2 + 1)(c^3 - (c^2-1)^{3/2})/3 \left. \right) + \left(-\frac{\epsilon_{i0}(1-2a_i)2}{bB} \left(\epsilon_{i0} n(\frac{\pi}{2\theta_{00}})^2 (4a_i(-\frac{2}{3}((c^2-1)^{3/2} \right. \right. \right. \\
& \left. \left. - c^3) - (c^2-1)^{1/2}) - B/4 \right) - \epsilon_{i0}^{3/2}/b \left(\left(\frac{2}{3}(c^3 - (c^2-1)^{3/2}) - (c^2-1)^{1/2} \right) \times \right. \right. \\
& \left. \left. (2a_i^2 - (\frac{n(\frac{\pi}{2\theta_{00}})^2}{2} + 2a_i) - \left(\frac{a_i^2 8\sqrt{2}}{B^2} + \sqrt{\frac{1}{2}} \right)^2 \left(-\frac{n(\frac{\pi}{2\theta_{00}})^2}{2} \right) \left(\frac{2}{3}(c^3 - (c^2-1)^{3/2}) - \right. \right. \right. \right. \\
& \left. \left. (c^2-1)^{1/2} \right) \right) - (4a_i^2 + 1) \frac{n(\frac{\pi}{2\theta_{00}})^2}{2} \left(\frac{2}{15} c^3 - \frac{1}{3} (c^2-1)^{3/2} \right) - \frac{B^2}{24} (c^3 - (c^2-1)^{3/2}) \right) \hat{\phi}^2
\end{aligned}$$

$$p = 1 + \epsilon_{i0}(-1/2 + 2/M_{\infty}^2 \epsilon_{i0} - \hat{\phi}^2/2 \left((n(\frac{\pi}{2\theta_{00}})^2 + 4a_i) y_0 + 2a_i \right)^2$$

$$y_0 = \frac{-4a_i + \sqrt{16a_i^2 + 4(n(\frac{\pi}{2\theta_{00}})^2 + 4a_i)}}{2(n(\frac{\pi}{2\theta_{00}})^2 + 4a_i)} \quad B = \sqrt{4(n(\frac{\pi}{2\theta_{00}})^2 + 4a_i)}$$

$$c^2 = \frac{4a_i^2 + n(\frac{\pi}{2\theta_{00}})^2 + 4a_i}{n(\frac{\pi}{2\theta_{00}})^2 + 4a_i} \quad b = \sqrt{n(\frac{\pi}{2\theta_{00}})^2 + 4a_i - 4a_i^2}$$

These expressions (y and p) will then be used in Appendix (A) to derive matching conditions for the internal and external layer near the axis of symmetry. From this procedure, we can extract internal shock and external shock radii of curvature and the positions of the shocks in space.

This information will be sufficient starting conditions for an integration across the layer of the away from the axis equations. By this procedure, the full bow region, from the axis to the corner region, may be calculated.

DISCUSSION OF RESULTS

From the analytical bow region results scaling parameters are defined which can be used in experimental simulations and in extensions of calculated results to other conditions. They can be obtained by examining the first order results of the bow analysis. For the internal flow, we find to the first approximation that the geometry of the layer (i.e., shock position and layer thickness) depends on the parameters n , ϵ_{i0} , $\theta_{\infty}(M_j, \theta_n, \chi_j)$ and $R_{s_{i0}}(\pi, \theta_{\infty}, n, \chi_j)$. To this list, we must add external layer parameters ϵ_e and R_{s_e} . However, from the matching of contact surface position, it is determined that R_{s_e} is a function of $R_{s_{i0}}, \theta_{\infty}, n, \epsilon_{i0}$ and therefore only ϵ_e is added, giving as the significant defining parameters of the bow region $\theta_{\infty}, n, \epsilon_{i0}, \epsilon_e, R_{s_{i0}}$. These may be further reduced if we consider very high Mach number flow for which ϵ_{i0} and ϵ_e reduce to χ_j and χ_e . The geometry of the flow is now independent of stream Mach number. For a correct experimental simulation, all of the above parameters should be matched between the actual system and the experimental setup.

Also, for a given system with fixed ambient and exhaust gas composition (i.e., fixed χ_j, χ_e) and nozzle conditions (i.e., fixed θ_{∞}, n) the bow geometry will scale with $R_{s_{i0}}$ or $\pi^{1/2}$ for all flight conditions (i.e., altitude, velocity) and system

thrusts (i.e., P_o). This last effect is illustrated in figure 4 which compares in a coordinate system which is reduced by the scale R_{sio} experimentally determined^{3,7,24} bow region geometries obtained at different values of π . Also shown in figure (4) is a comparison between experimental results carried out at nearly the same π but with different external flow Mach numbers. As can be seen, the agreement in positions both for varying π and $M_{\infty e}$ is very good, indicating that the scaling parameters are correct, and also that for high Mach numbers the geometry is effectively independent of stream Mach numbers.

The correctness of the scaling is further substantiated by examining figure (6) in Charwat and Faulmann². In this figure, many experimental values of axial bow layer thickness divided by R_{sio} are plotted versus π . For both $M_{\infty e} = 2.75$ and 7.1 it is shown that the above ratio becomes constant as π becomes large, indicating the correctness of the scaling parameter R_{sio} . It should also be mentioned that the value of the ratio reached for $\pi \gg 1$ and $M_{\infty e} = 7.1$ is in agreement with the value obtained from figure (4).

Having established that the geometries of the shocks and contact surface are fixed in a reduced coordinate system, we then note that to first approximation all the nondimensionalized flow variables will also scale since they are only functions of $\phi, R/R_{sio}, n, \theta_{\infty}, \gamma_j, \gamma_e$ which are fixed quantities for any

given point in the flow if the nozzle conditions and exhaust and ambient gas composition are fixed.

Another result of the analytic analysis of the bow region is that it defines the accuracy of the Newtonian impact approximation which was applied by Laurmann⁶ to this problem. In his technique, the contact surface position is determined by the balancing of Newtonian impact pressure along the contact surface.

This approximation has been shown to yield good results for surface pressure for the external bow region flow²⁵.

For the internal bow region layer flow, we must examine our analytic solution to establish the accuracy of the Newtonian impact theory in describing the surface pressure. From the first order results, the layer thickness is a constant. Also, to first order pressure is constant across the layer. The actual contact surface pressure will then be determined by the shock shape, which for constant layer thickness is the same as the contact surface. Therefore, we would expect the Newtonian impact analysis to give reasonably good results for the internal as well as the external flow contact surface pressure. The contact surface shape in the bow region, as determined by the matching of the impact pressure across it, should then be reasonably well predicted by Laurmann's⁶ analysis.

To test this hypothesis the contact surface position predicted by Newtonian impact analysis is compared in figure (5) with the predictions made in this study and in reference (7) for a characteristic bow interaction. The agreement shown is very good, indicating the usefulness of this approximation to quickly obtain bow region geometry. The success of the technique in this axisymmetric case gives one confidence in extending this simple technique to asymmetric bow region flows where the angle of attack of the jet to the free stream is not large. For the transonic corner and supersonic far field regions, Laurmann's⁶ technique must necessarily fail due to the thickening of the layers and the acceleration of the flow in these regions.

A number of calculations of the bow region flow have been carried out, utilizing the analyses outlined in the preceding section and in Appendix A. These calculations have attempted to: (i) compare predicted bow interactions with results from an existing numerical technique; (ii) compare predictions with an experimental result by Zakkay⁷; (iii) determine the variation of bow region geometries and pressure distributions with variations in Θ_∞ and δ_j (primary jet flow parameters); (iv) give detailed predicted properties for two cases which are characteristic of "cold" jet and actual jet operation.

In the comparison of the present predictions with those of Rudman and Vaglio-Laurin⁷ identical stream and undisturbed plume parameters were utilized. Predictions, which included terms with errors $O(\epsilon_{i_0})$ and $O(\epsilon_{i_0}^{3/2})$ were made of flow field geometry and pressure, as well as the other variables of interest. As can be seen from figure (6), the present results and those calculated by the numerical technique of reference (7) do not agree very well in position, although shapes are similar. Also, the comparison of pressure distributions in figure (7) do not agree very well. There are two possible sources of error which could cause the poor agreement shown. The first possibility is that the example calculated, with $\delta_e, \delta_j = 1.4$ is just too difficult a test for the present theory, which is based on having $\delta_e, \delta_j \approx 1.0$. Since the internal flow solution proceeds in half powers of ϵ_{i_0} then for the example calculated terms higher than the first are really not very small. This causes poor convergence of the solution, which is indicated by diminishing oscillations of the variables about their correct values as higher order terms are added to the solution. This type of behavior is observed in figure (7). However, figure (6) does not show this effect; and, therefore, this cannot be the total explanation for the lack of agreement.

A possible source of error in the technique of reference (7) is the imposition of a point interaction (i.e., non penetra-

tion) for the corner region in the calculations of reference (7). As will be explained further in the section on the corner region, the point interaction assumption puts a constraint on the bow region calculation, which could possibly over-emphasize the corner region flows upstream influence on the bow layer properties. This could result in the large difference in internal layer thickness which is observed in figure (6). Taking the above two effects together, it is possible, within the bounds of error of the present results, to show agreement between geometry and pressure distribution.

It should be mentioned that the results of reference (7) have been compared favorably with the experimental results of Zakay⁷. However, the comparison is not definitive since the analytical plume flow model used had an exponent of 2.5, which has been shown in the section on jet exhaust models to be in large error for the case calculated.

Good agreement between the prediction of bow region geometry and the experimental results of Zakay⁷ is shown in figure (8). No linear scale was given in the experimental schlieren photograph; and, therefore, it was necessary to arbitrarily scale the experimental and predicted results by setting the jet to internal shock distances equal to each other. The contact surface pressure distribution for this same case is

shown in figure (9). Two other calculations were made for these same conditions with the only difference being that in the analytic plume model, exponents $n = 5.0$ and 2.5 were used instead of the more correct 4.17 value. In figure (10), these predictions show a marked sensitivity of bow region geometry (i.e., shock and contact surface position) to plume model exponent. The variation of the bow geometry with plume exponent is larger than the error bounds of the solution indicating that if accurate predictions of bow region properties are to be obtained then the plume model used must also be very accurate.

In noting the good agreement between the predicted and experimental geometry, one is tempted to state that the calculated flow properties must also be in good agreement with experimental values. However, this is risky in that experience with co-flowing plumes and the good agreement of the calculated results of reference (7), using an incorrect plume model, with experimental results show that the coarse geometry of the interaction (i.e., shocks and contact surface) can be predicted relatively easily but in all probability the detailed experimental flow properties are not so easily matched by calculations.

Figures (11), (12), (13) and (14) show the effect of varying θ_∞ and δ_j on bow geometry and contact surface pressure distribution.

From figure (11) it can be seen that increasing Θ_{∞} from 125.5 degrees to 185.0 degrees, which could be accomplished by either increasing Θ_n or decreasing M_j , results in a definite increase in layer thickness both for the internal and external flow. Since external layer thickness is directly proportional to contact surface radius of curvature, then an increase of layer thickness indicates an increase in radius of curvature. Consistent with the increase in contact surface radius of curvature, we note from figure (12) an increase in contact surface pressure with an increase in Θ_{∞} . In general increases in Θ_{∞} with all other parameters fixed give increases in contact surface radius of curvature, yielding a more blunt bow region interaction. In figures (13) and (14) we can see the effect of increasing γ_j with all other parameters fixed. Increasing γ_j from 1.2 to 1.4 in figure (13) causes a definite thickening of the internal and external layers. Also, from the contact surface pressure curves in figure (14) we note that increasing γ_j results in an increased pressure level. Both of these effects are primarily the result of an increase in radius of curvature of the contact surface. In conclusion, an increase in either Θ_{∞} or γ_j for all other parameters fixed causes an increase in radius of curvature of the contact surface resulting in a more blunt bow interaction. In this case, pressure, density and temperature within the layers do not decay as rapidly as in the less blunt interaction case.

In figures (15-18) detailed distributions of flow properties for a "cold" jet and actual jet operation are given. The cold jet case, shown in figures (15,16) would be representative of a wind tunnel simulation where the ratio of jet to freestream stagnation temperature is 2.0 and air is used as the jet gas. The actual jet case shown in figures (17,18) is representative of a real system that is operating at 150,000 ft. altitude, whose jet gases are composed primarily of H₂O and CO₂ which is modeled by setting $\gamma_j = 1.24$. The ratio of jet to free-stream stagnation temperature is .75, which is representative of the actual system.

As can be seen from figures (15) and (17), the flow geometry, streamlines and isobars for the two cases are very similar. However, from figures (16) and (18) we note wide differences between the two cases. In figure (16) it can be seen that the velocity discontinuity between the internal and external flow is very small at the contact surface and consequently, mixing effects along it will be small. We also note a moderate jump in density as we go from the external to internal flow. Since pressure is equal across this surface, then the above result indicates that we have a less dense and hotter external layer flowing past a more dense and cooler internal layer. In figure (18) we note some significant differences from the "cold" jet case of figure (16). Here, we find that there is a large velocity discontinuity which leads to strong

mixing effects. Also, the very large discontinuity in density indicates that a very hot and low density external layer is flowing past a much cooler and denser internal layer.

If heat transfer were allowed, there would be a heating up of the cooler internal layer by the hot external layer. It can be concluded that in the actual case mixing and heat transfer effects will be much larger than the experimental simulation case.

ANALYSIS OF CORNER REGION

For an exact treatment of this region, the inviscid external and internal layer bow flows, as well as the relatively motionless core and the viscous mixing region separating the core and bow flows, must be simultaneously calculated. The reasons for utilizing this coupled approach have been discussed previously in references (2) and (3). Such a complex treatment is beyond the scope of the present study and simplified analyses are applied. Unlike the bow region and downstream region analysis (to be discussed), the corner region flow is not amenable to analytic treatment because of its transonic nature and complicated coupling with the core flow and the viscous layer separating these regions.

An approach is then taken which will provide an estimate of some of the flow characteristics within the corner region and will also assess the significance of the corner region flow on the bow and downstream region solutions. In brief, this section will outline: (i) the significance of the corner region flow on the bow region and downstream flow properties as calculated by their respective analyses; (ii) an engineering estimate of the pressure level in the core region; (iii) the location of the plume boundary based on this core pressure; (iv) the qualitative penetration of the intercepting shock layer mass flow into the internal layer, and the location of the internal layer sonic line.

Before establishing the significance of the corner region flow to the bow and downstream flow solutions, a brief description of the flow in the corner region will be given. Referring to figure (19), the jet gases upon exiting the nozzle expand into the low, nearly constant pressure core flow. An intercepting shock and shock layer form which are identical to those for a plume in a quiescent ambient of the same pressure. This intercepting shock and layer eventually intersect the strong internal shock, resulting in a triple point shock configuration similar to that found at the Mach disc for plumes in a quiescent or co-flowing ambient. A complex system of shocks and expansions are then generated within the internal and intercepting shock layer, which accelerates and turns the flow in the downstream direction. The viscous layer separating the core and internal flow reattaches at a downstream location, recompressing the flow to a pressure greater than that of the core. All of the above flow processes interact, establishing a unique geometry for the corner region.

Having defined the corner interaction an order of magnitude assessment of its effect on the bow and downstream flow solutions will now be given.

Significance of the Corner Region on the Bow and Downstream Solution

Since the bow region layers are thin and bounded by strong shocks, then the flow properties within the layers are strongly influenced by the local shock conditions and only weakly influenced by the conditions in the corner region near the sonic point. We can therefore conclude that the bow layer properties can be calculated independently of the corner region without incurring serious error. Since, as is discussed in the next section, the downstream flow depends on the balancing of jet and external flow interaction forces along the contact surface, then the significance of the corner region flow on the downstream solution is assessed by determining the axial force balance that would occur if the corner region flow is included or neglected. For the case when it is neglected, the jet flow is assumed to expand to its vacuum limiting angle, θ_∞ .

The particular example studied herein is that given in a report by Rudman and Vaglio-Laurin⁷. The axial force created by the jet flow is given by

$$F_x = - \int \rho \vec{q} (\vec{q} \cdot \vec{n}_x) dA - \int p \vec{n}_x dA$$

Applying this to the cases with and without the corner region and taking their difference divided by the total force of the jet, we obtain

$$\frac{\Delta F_x}{F_{x \text{ total}}} = \frac{\int_{\phi_{RS}}^{\theta_\infty} \cos^n \frac{\pi \phi}{2\theta_\infty} \sin \phi \cos \phi d\phi - \xi \cos \nu \int_{\phi_{RS}}^{\theta_\infty} \cos^n \frac{\pi \phi}{2\theta_\infty} \sin \phi d\phi}{\int_0^{\theta_\infty} \cos^n \frac{\pi \phi}{2\theta_\infty} \sin \phi \cos \phi d\phi}$$

where $\frac{1}{2} < \xi < 1$ and $0 < \nu < \varphi_{RS}$
 Substituting in the numerical values $\Theta_{\infty} = 130.45$, $\varphi_{RS} = 55$ de-
 grees, $n = 4.17$, $\xi \cos \nu = \frac{1}{3}$ we obtain

$$\frac{\Delta F_x}{F_{x \text{ total}}} = .0425 \text{ or } 4 \text{ percent}$$

This error is well below that created by using the approximate analytical source flow expression (1) which in some cases can be in considerable error¹⁵.

Since the details of the corner region flow are not significant to the calculation of bow or downstream properties, then engineering estimates of core pressure, plume boundary and penetration will be sufficient to approximate the corner region flow for this study.

Core Pressure

Qualitatively, the external and internal flows do not bend immediately downstream after passing the intercepting shock layer boundary due to the considerable lateral momentum imparted to the layers in the bow region. Instead, the external shock moves continuously outward along with the bulk of the external and internal layer mass flow, leaving behind in its "wake" a low pressure (with respect to the shock value) flow adjacent to the core region. On this basis, we would expect the core pressure to be low and of the same order as ambient pressure.

In determining the core pressure, the experimental results of Finley³, Charwat and Faulmann², and Jarvinen and Adams²⁶ will be utilized. From figure (7) of Finley, it can be seen that as π is increased, the core pressure drops to a nearly constant value. This behavior is also consistent with figure (11) in Jarvinen and Adams and figure (15) in Charwat and Faulmann. In our analysis, which is the limiting case when $\pi \gg 1$, the core pressure will then be at a constant level for all values of π .

These results are for exit Mach numbers of 1.0, 2.6, 3.1, 3.9, and 4.3 and freestream Mach numbers of 2.5, 2.75, .6 and 2.0. We therefore conclude that this behavior with π does not depend on exit or freestream Mach number.

Noting the lack of dependency of the core pressure on π for $\pi \gg 1$ we can now correlate all experimental results to establish the best value for P_{core} . From figure (20), it is seen that the most general result, especially for high external Mach number, would be $P_{\text{core}} = 1$. This result is reasonable considering the wide variety of M_{∞}, M_j under which $\frac{P_{\text{core}}}{P_{\infty}}$ has been obtained and also in consideration of the nonuniformity in pressure throughout the core region.

Plume Boundary

As was mentioned previously, the plume develops in a region of nearly constant pressure and, therefore, it is analogous to the case of an underexpanded jet into a still ambient. Various analytical approaches describing the location of the boundary of the plume have been developed. (for eg. see reference 27 and reference 23). Most of them give reasonable results near the nozzle exit but diverge considerably from the actual boundary away from the exit. For this study, an analytical technique²⁹ is used which assumes a fixed plume shape for all nozzles when the coordinates are nondimensionalized with respect to plume boundary maximum radius and its axial coordinate. The advantage of this method is that it gives the correct boundary location not just near the nozzle exit but far from it as well. The method relies on setting up momentum and force balances between the exhaust and core region gases. The shape of the plume when nondimensionalized is represented well by

$$y/y_m = \frac{2j}{2j-1} \left((x/x_m)^{1/2} - 1/2n(x/x_m)^j \right)$$

where $j = 2.5$ gives the "best" fit with numerical data. The balance of lateral and axial momentum give respectively

$$2 P_{core} \int_0^{x_m} y dx = P_{oj} A_* f_1(x_m/r_*)$$

$$P_{core} \pi r_*^2 x_m^2 = P_{oj} A_* f_2(x_m/r_*)$$

where f_1 and f_2 are functions of the nozzle geometry and exhaust gas conditions. From the above expressions x_m/r_* and y_m/r_* can be found for any jet exit and ambient condition, thereby giving the plume boundary. This technique was utilized in locating the plume boundary for the example given in Rudman and Vaglio-Laurin's ⁷ study. Good agreement is found with experimental results as can be seen in figure (8). Since we are dealing with highly underexpanded plumes (i.e., $\pi \gg 1$) where the intercepting shock layer is thin, then this boundary location is also assumed to be a good approximation for the intercepting shock location.

Penetration of the Internal Layer

Referring to figure (19), we can establish a qualitative description of the corner region flow. The reflected shock emanating from the triple point, at a, crosses the intercepting shock layer and intersects the plume boundary at c. Since the boundary must be at constant core pressure, then the shock must be reversed and reflected as an expansion c-b. Crossing the layer, this expansion then intersects the slip stream surface at b, being once again reflected and partially transmitted as an expansion into the slightly supersonic internal layer flow d. The surface b-a remains nearly straight since only a small drop to sonic pressure over this region is expected, which requires very little turning along b-a of the supersonic flow in region a-b-c. The internal flow sonic point occurs at b because if it were sonic before this point

the non divergence of the streamlines in this region would unrealistically prevent the flow from accelerating further. Also, the sonic point cannot lie beyond b because the diverging nature of the flow would not allow sonic velocity to be achieved from the initial subsonic state.

Within the slightly supersonic flow region, d, the transmitted expansions b-c are reflected off the nearly constant pressure sonic line surface as compressions. These return to the intercepting shock layer and are transmitted to the core region. The continual process of reflection, transmission and interaction of these waves results in the rapid turning of the flow in the downstream direction as is illustrated in figure (19). Some idea of the shape of the sonic line and its limiting characteristics can be obtained by applying the ideas developed by Hayes and Probstein³⁰ for blunt body flows.

Taking ω as the angle that the contact or slip stream surface makes with the sonic line at these respective surfaces, we can write

$$\tan \omega = - \frac{\left(\frac{\partial q}{\partial s}\right)_{b,e}}{\left(\frac{\partial q}{\partial n}\right)_{b,e}}$$

where

$$\left(\frac{\partial q}{\partial n}\right)_{b,e} = -\zeta_{b,e} - q_{b,e}^2/R_{b,e}$$

and $q_{b,e}$ is streamline velocity, $\zeta_{b,e}$ vorticity and s and n are the coordinates along and perpendicular to the slip stream and contact surface. At point b we have nearly a straight

slip stream b-a and therefore the second term in $(\frac{\partial q}{\partial r})_b$ is negligible. Also, the shock is nearly spherical and in the vicinity of point a the vorticity generated is small. Under these conditions, $(\frac{\partial q}{\partial r})_b \approx 0$ and therefore $\omega \approx \pi/2$ at b. At the contact surface, point e, different conditions prevail. Using the first order expressions derived in the bow region analysis section and assuming for simplicity that the internal shock and contact surface are spherical in nature, then we can write in terms of nondimensionalized variables.

$$\xi_e = n \left(\frac{\pi}{2\theta_\infty} \right)^2 \hat{\phi} \quad q_e = \sqrt{n} \frac{\pi}{2\theta_\infty} \hat{\phi}$$

Using Rudman's⁷ example, we can write

$$\left(\frac{\partial q}{\partial r} \right)_e = -\hat{\phi} \left(n \left(\frac{\pi}{2\theta_\infty} \right)^2 - \sqrt{n} \frac{\pi}{2\theta_\infty} \right) = -.83 \hat{\phi}$$

also, we have

$$\left(\frac{\partial q}{\partial s} \right)_e = \sqrt{n} \frac{\pi}{2\theta_\infty} = 1.54$$

The ratio of these expressions gives

$$\tan \omega = \frac{1.85}{\hat{\phi}} \text{ which for } \hat{\phi} = 55^\circ \text{ gives } \omega = 62 \text{ degrees}$$

Now that the sonic line angles are estimated at both boundaries, we can then sketch its location throughout the layer as shown in figure (19). The initial turning of the sonic line in the downstream direction from point b, due to centrifugal pressure gradient effects, is typical of the rapid transonic expansion occurring in d and gives the sonic line its

characteristic s shape. The last limiting characteristic lines which originate in regions d and f are also shown in figure (19). Having obtained a qualitative estimate of the penetration of the intercepting shock layer into the internal layer, we can now make an estimate of the actual penetration for the example calculated by Rudman and Vaglio-Laurin⁷. The first step is to estimate the intercepting shock layer thickness which can be determined on the basis of mass flow considerations. Subscripting layer properties by ℓ and utilizing standard notation for undisturbed plume quantities, we can write

$$\rho_{\ell} u_{\ell} 2\pi R_s \sin\theta_{\ell} \delta_{\ell} = \int_{\theta_{\ell}}^{\theta_{\infty}} \rho_{\infty i} u_{\infty i} 2\pi R_s^2 \sin\phi d\phi$$

Substituting in the analytic expressions for $\rho_{\infty i}$ and $u_{\infty i}$ which can be derived from the analytical plume flow model, and, letting

$$\rho_{\ell} = \frac{\rho_{\infty i}}{\epsilon_{i0}} (1 + 1/2) \quad u_{\ell} = u_{\infty i} (1 + \epsilon_{i0}/\tan 17^{\circ})/2$$

we obtain

$$\frac{\delta_{\ell}}{R_{s_{i0}}} = \frac{4}{3} \frac{\epsilon_{i0} \int_{\theta_{\ell}}^{\theta_{\infty}} \cos^n \frac{\pi\phi}{2\theta_{\infty}} \sin\phi d\phi}{\cos^n \frac{\pi\theta_{\ell}}{2\theta_{\infty}} \sin\theta_{\ell} (1 + \epsilon_{i0}/\tan 17^{\circ})}$$

For $\theta_{\infty} = 130.45^{\circ}$ $\theta_{\ell} = 55^{\circ}$ and $\epsilon_{i0} = \frac{1}{6}$ we have $\frac{\delta_{\ell}}{R_{s_{i0}}} = .0627$

This value is characteristic of plumes where $\pi \gg 1$. The second step involves determining the reflected shock position from the triple point solution. Using the initial conditions

$$M_{\infty i} = 9.2, \beta = 86^{\circ} \quad \text{for the strong shock and } \beta = 20^{\circ}$$

for the intercepting shock, we obtain the reflected shock position from D'Attorre³¹ which is shown in figure (8).

Assuming that the Mach number downstream from the reflected shock is constant, we can then determine the initial reflected expansion wave's position and intersection with the slip stream surface. The position of this wave as shown in figure (8) defines the extent of the penetration into the internal layer. Unlike the point interaction or zero penetration model proposed by Rudman and Vaglio-Laurin⁷, we note a considerable penetration of the internal layer by the intercepting shock layer flow. This fact is borne out experimentally in a study³² on the similar problem of a jet impinging normally and at an angle to a flat plate. The constraints on the numerical solution of Rudman and Vaglio-Laurin⁷ imposed by their assumption of a point interaction (i.e., zero penetration) for the corner region could be a source of considerable error in their calculation of the bow region.

It should be mentioned that the large penetration indicated in this study does not necessarily mean that the bow region flow is strongly influenced by the corner region penetration. This is because, in the absence of the corner region flow, the internal flow streamlines would penetrate the layer much like the slip stream separating the internal and intercepting shock layer flows. This can be seen by comparing streamlines obtained from the bow analysis in figure (17) with the slip stream position shown in figure (8).

From the results presented a scaling criteria for the corner region is now outlined. The major characteristic to be scaled is the undisturbed plume boundary, which for a given nozzle and exhaust gas composition depends on $P_{0j}/P_{\infty e}$. For an exact simulation of the plume boundary, this ratio must be matched. If, for a given system, it can be shown that the plume boundary coordinates are proportional to R_{sio} or $\pi^{1/2}$ then the plume boundary will scale like the bow region. The technique²⁹ used to locate the plume boundary normalizes the geometry by r_m and x_m the plume maximum radius and its axial location. When these are plotted as a function of

$P_{0j}/P_{\infty e}$ it is found that

$$\frac{r_m}{r_*}, \frac{x_m}{r_*} \propto (P_{0j}/P_{\infty e})^{1/2}$$

Since π is proportional to $P_{0j}/P_{\infty e} M_{\infty e}^2$ then

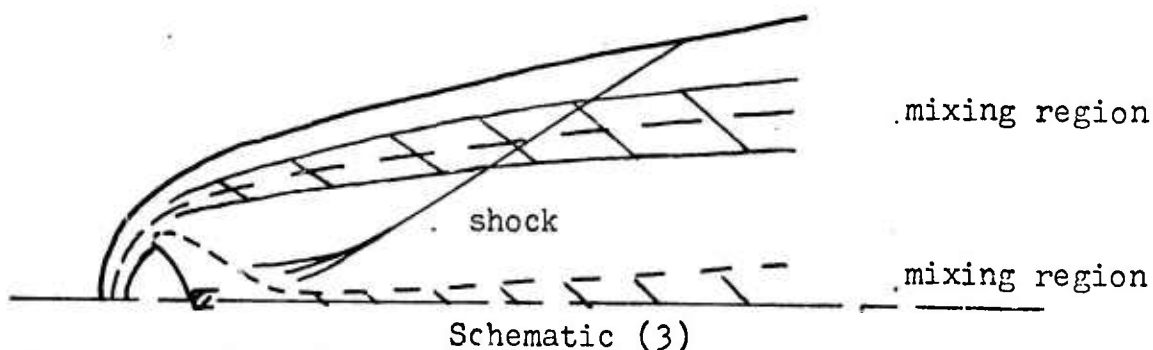
$$\frac{r_m}{r_*}, \frac{x_m}{r_*} \propto \pi^{1/2} M_{\infty e}$$

Thus, if $M_{\infty e}$ is fixed, then the plume boundary will scale with R_{sio} . The scaling of the bow region and plume boundary then requires that $\delta_j, \delta_e, \theta_{\infty}, \eta$, and $M_{\infty e}$ be fixed over the entire flight range. Since $M_{\infty e}$ does not vary greatly over a typical system trajectory, then the above scaling requirements are satisfied for some systems of interest.

This scaling result is substantiated by some experimental^{3, 7, 24} data in which the plume boundary triple point distance away from the axis, when divided by the scale length R_{sio} is nearly constant for values of π from 30 to 627.

FAR FIELD REGION ANALYSIS

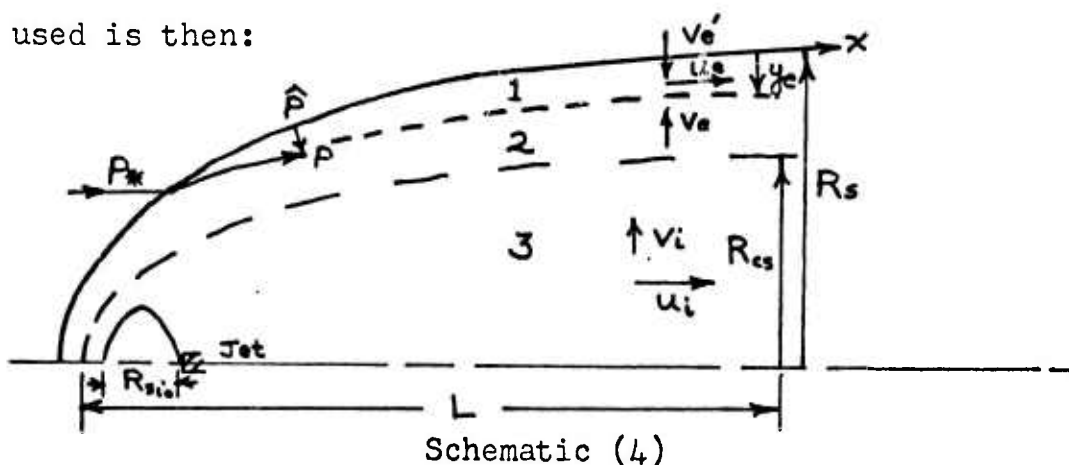
The downstream flow region between the external shock and axis of symmetry consists of supersonic layers bounded by mixing regions and crossed by a wake recompression shock as is illustrated in schematic (3)



This general problem cannot be handled by approximate analytical techniques; therefore, we will seek to solve a reduced problem within the framework of the assumptions listed in the introduction. This problem will involve:

- 1) the neglect of all mixing regions (wake and shear surface)
- 2) the neglect of the recompression shock

Assumption 1) will be valid at moderate altitudes and 2) will be reasonable since the recompression shock is weak compared to the external shock. A schematic of the flow and notation used is then:



The numerical matching criteria between the internal and external flow requires that static pressure and flow deflection must be equal at the contact surface. Also, the stagnation pressures will be equal due to the upstream matching condition.

The particular region of interest in this downstream analysis will be at a point characterized by the distance L , where

$L \gg R_s, R_{cs}$. The ratio of R_s to L will be a significant parameter for the downstream problem and we denote it by the symbol $\delta_e = R_s/L$. Once again, as in the bow region, we will be considering the case when $M_{\infty i}, M_{\infty e} \gg 1, \epsilon_i, \epsilon_e \ll 1$. An approximate analytical method of solution is available for the external layer flow near the shock surface in region 1. This method was first applied by Cole³³ and involves taking the limits in the inviscid flow equations as the perturbation quantities.

$$M_{\infty e} \rightarrow \infty, \quad \epsilon_e \rightarrow 0, \quad \delta_e \rightarrow 0$$

$$M_{\infty e} \delta_e \rightarrow \infty \quad M_{\infty e}^2 \delta_e^2 \epsilon_e \rightarrow O(1)$$

The solution found by this procedure is valid to a distance of $O(\epsilon_e \delta_e L)$ measured inward from the shock surface. For attached shocks, this solution would be valid throughout the external layer. However, if the shock has a blunt nearly normal forward region, the external layer becomes thicker than the above order of magnitude and the solution breaks down away from the shock toward the contact surface. This is due to the viola-

tion in the blunt region of the assumption that the shock makes small angles with the free stream. As was pointed out by Cheng and Kirsch³⁴ in the equivalent unsteady case, a region of thickness $O(\delta_e L)$, denoted 2 in schematic (4), is then found near the contact surface which requires a different expansion in order to develop a valid solution in this region. The solution found in this "entropy wake" matches with the outer layer, and the composite expansions for the entire external layer will be given.

For the internal layer, we have two conditions imposed by the external flow at the contact surface, which can be used to establish the orders of magnitude of the flow variables within region 3, the interior layer. They are:

$$P_{cs_e} = P_{cs_i}$$

$$\left(\frac{dR_{cs}}{dx}\right)_e = \left(\frac{dR_{cs}}{dx}\right)_i$$

Based on these conditions, we can then prescribe expansions for the flow variables in terms of perturbation parameters that will lead to a system of analytical solutions for the inner layer.

Like the external "entropy wake" the internal layer is of thickness $O(\delta_e L)$. Utilizing the orders of magnitude found from the contact surface and upstream bow region conditions, we

then develop expansions which will be solved giving expressions for layer thickness and other variables of interest. Numerically matching these expressions with those of the external flow, along the contact surface, we then achieve analytic solutions in the far downstream region. These results are found to depend on the upstream bow interaction between the plume and external stream. Taking results from the bow region consistent with the accuracy of the downstream region, we then find the complete solution for the downstream flow. In the following discussion for the external flow, frequent reference will be made to the work of Cheng and Kirsch³⁴. They solved an unsteady problem that in many ways is analogous to our external layer problem by the application of the hypersonic equivalence principle. For details of the external layer analysis, the Cheng and Kirsch paper should be consulted.

External Layer - Region 1 Analysis

Utilizing the notation illustrated in schematic (4), the following general set of equations and boundary conditions for the downstream problem in terms of von Mises variables are.

$$\frac{\partial R_e}{\partial x_e} = \frac{V_e}{U_e} \quad (1.1) \text{ stream-} \\ \text{line slope}$$

$$\frac{\partial R_e}{\partial \Psi_e} = \frac{1}{\rho_e U_e R_e} \quad (1.2) \text{ continu-} \\ \text{ity}$$

$$\frac{1}{R_e} \frac{\partial V_e}{\partial x_e} + \frac{\partial p_e}{\partial \Psi_e} = 0 \quad (1.3) \text{ momentum} \\ \text{normal to} \\ \text{streamline}$$

$$U_e^2 + V_e^2 + \frac{2\gamma_e}{\gamma_e - 1} \frac{p_e}{\rho_e} = g(\Psi_e) \quad (1.4) \text{ Bernoulli} \\ \text{integral}$$

$$p_e / \rho_e^{\gamma_e} = f(\Psi_e) \quad (1.5) \text{ entropy} \\ \text{integral}$$

Boundary conditions at external shock

$$\hat{p}_e = p_{\infty e} + \frac{2\gamma_e}{\gamma_e + 1} p_{\infty e} (M_{\infty e}^2 \sin^2 \beta_e - 1) \quad (1.6)$$

$$\hat{\rho}_e = \rho_{\infty e} / \left(\frac{\gamma_e - 1}{\gamma_e + 1} + \frac{2}{(\gamma_e + 1) M_{\infty e}^2 \sin^2 \beta_e} \right) = \rho_{\infty e} / \epsilon'_e \quad (1.7)$$

$$\hat{U}_e = U_{\infty e} (1 - 2(M_{\infty e}^2 \sin^2 \beta_e - 1) / (\gamma_e + 1) M_{\infty e}^2) \quad (1.8)$$

$$\hat{V}_e = U_{\infty e} (2(M_{\infty e}^2 \sin^2 \beta_e - 1) \cot \beta_e / (\gamma_e + 1) M_{\infty e}^2) \quad (1.9)$$

Boundary conditions at contact surface

$$P_{e cs} = P_{i cs} \quad (1.10)$$

$$\frac{dR_{e cs}}{dx} = \frac{dR_{i cs}}{dx} \quad (1.11)$$

Velocity parallel and normal to the shock are:

$$\hat{u}' = U_{\infty e} \cos \beta_e \quad (1.12)$$

$$\hat{v}' = \epsilon_e' U_{\infty e} \sin \beta_e \quad (1.13)$$

The expanded Rankine-Hugoniot relations lead to the following orders of magnitude for the flow parameters near the shock:

$$\hat{p}_e \sim O(\rho_{\infty e} U_{\infty e}^2 \delta_e^2) \quad (2.1)$$

$$\hat{\rho}_e \sim O(\rho_{\infty e} / \epsilon_e) \quad (2.2)$$

$$\hat{u}_e \sim O(U_{\infty e}) \quad (2.3)$$

$$\hat{v}_e' \sim O(\epsilon_e \delta_e U_{\infty e}) \quad (2.4)$$

where ϵ_e is evaluated at the point where $\beta_e = \pi/2$. These conditions will be the upper boundary values for the external layer. From the orders of the variables near the shock, the dimension normal to the shock can be inferred from continuity considerations.

$$y \sim O(\epsilon_e \delta_e L) \quad (2.5)$$

The dimensions of the streamwise coordinate are easily seen to be

$$x \sim O(L) \quad (2.6)$$

These orders of magnitude, (2.1 to 2.6), are then used to form asymptotic expansions which are

$$p_e = p_{\infty e} U_{\infty e}^2 \delta_e^2 p_{0e} + \dots$$

$$\rho_e = \rho_{\infty e} p_{0e} / \epsilon_e + \dots$$

$$u_e = U_{\infty e} + \delta_e^2 U_{\infty e} U_{0e} + \dots$$

$$v_e' = U_{\infty e} \delta_e \epsilon_e v_{0e} + \dots$$

$$y_e' = L \delta_e \epsilon_e y_{0e} + \dots$$

Substituting these expansions into the equations of motion, (1.1 to 1.5), and boundary conditions, (1.6 to 1.13), we can develop a sequence of equations which can be solved and then summed to yield the solution to any desired accuracy in terms of $\epsilon_e, \delta_e, M_{\infty e}$.

The first order system from the above procedure is

$$\frac{\partial p_{0e}}{\partial \Psi_e} = -\frac{1}{R_{se}} \frac{\partial^2 R_{se}}{\partial x_e^2} \quad (3.1)$$

$$\frac{\partial}{\partial x_e} (p_{0e} / \rho_{0e}) = 0 \quad (3.2)$$

$$\frac{\partial y_{0e}}{\partial \Psi_e} = \frac{1}{\rho_{0e} R_{se}} \quad (3.3)$$

$$v_{0e}' = \frac{\partial y_{0e}}{\partial x_e} \quad (3.4)$$

The boundary conditions on the above at the shock surface are:

$$\hat{p}_{0e} = \left(\frac{d\hat{R}_{se}}{dx} \right)^2 \quad (4.1)$$

$$\hat{p}_{oe} = 1 \quad (4.2)$$

$$\hat{y}_{oe} = 1 \quad (4.3)$$

Integrating (3.1 to 3.4) and applying the boundary conditions (4.1 to 4.3), we obtain:

$$p_{oe} = \left(\frac{d\hat{R}_{se}}{dx_e} \right)^2 + \frac{1}{\hat{R}_{se}} \frac{d^2\hat{R}_{se}}{dx_e^2} (\hat{\Psi}_e - \Psi_{e*}) \quad (5.1)$$

$$p_{oe} = p_{oe} / \left(\frac{dR_{se*}}{dx_e} \right)^2 \quad (5.2)$$

$$y_{oe} = \frac{1}{\hat{R}_{se}} \int_{\Psi_{e*}}^{\hat{\Psi}_e} \frac{d\Psi_e}{p_{oe}} \left(\frac{dR_{se*}}{dx_e} \right)^2 \quad (5.3)$$

$$V_{oc}' = \frac{\partial y_{oe}}{\partial x_e} \quad (5.4)$$

Making the substitution

$$\Psi_{e*} = R_{se*}^2 / 2 \quad (5.5)$$

$$\hat{\Psi}_e = \hat{R}_{se}^2 / 2 \quad (5.6)$$

in the above, we then obtain results identical to those of Cole³³

$$p_{oe} = \left(\frac{d\hat{R}_{se}}{dx_e} \right)^2 + \frac{d^2\hat{R}_{se}}{dx_e^2} \frac{\hat{R}_{se}}{2} \left(1 - \left(\frac{R_{se*}}{\hat{R}_{se}} \right)^2 \right) \quad (6.1)$$

$$p_{oe} = p_{oe} / \left(\frac{dR_{se*}}{dx_e} \right)^2 \quad (6.2)$$

$$y_{oe} = 1/\hat{R}_{se} \int_{R_{se*}}^{\hat{R}_{se}} \frac{R_{se*} dR_{se*}}{p_{oe}} \left(\frac{dR_{se*}}{dx_e} \right)^2 \quad (6.3)$$

$$V_{oc}' = \frac{\partial y_{oe}}{\partial x_e} \quad (6.4)$$

As previously mentioned, these results are expected to hold

near the shock surface; however, their validity near the contact surface has to be examined. From the bow region solution we know that a blunt interaction occurs. Consequently, as we follow the shock surface upstream to the vicinity of the bow region, we note that the shock must become nearly normal in form. Therefore, it invalidates our assumption of small free stream to shock angle, initially made in our above analysis. Under these circumstances, one would not expect our expansion procedure to be valid in such a region; and this turns out to be the case, as was found by Cheng and Kirsch³⁴ for the unsteady problem. What we must do is alter our expansion procedure so as to be consistent with the strong part of the shock.

External Layer-Region 2 Analysis

Following Cheng and Kirsch³⁴ we assume that initially, due to the strong bow interaction of the jet and external flow, the external shock moves out in a blast wave manner. This requires that the external shock take the form:

$$\hat{R}_{se} = Ax_e^{1/2}$$

as $x_e \rightarrow 0$ where A is a function of the upstream bow interaction. A requirement which must be met by the contact surface in the vicinity of the blunt interaction is that:

$$\lim_{x_e \rightarrow 0} R_{cse} / \hat{R}_{se} \rightarrow 0$$

This states that initially the contact surface must move outward slower than the external shock, thus guaranteeing the dominance of the blast wave result for the upstream interaction. Up to this point, we have paralleled the unsteady problem quite closely. The equivalence principle is most accurate near the shock with the streamwise velocity given by:

$$u_e \sim U_{\infty e} + O(U_{\infty e} \delta_e^2)$$

The error involved in assuming $u_e \sim U_{\infty e}$ is seen to be small, of error $O(U_{\infty e} \delta_e^2)$. However, as we approach the contact surface we have for the streamwise layer velocity, from the Bernoulli Integral.

$$u \sim U_{\infty e} + O(U_{\infty e} \delta_e^{2(\frac{\gamma_e - 1}{\gamma_e})})$$

The error involved in taking $u \sim U_{\infty e}$ in order to apply the equivalence principle is seen to be large for $\gamma_e \approx 1$ of $O(U_{\infty e} \delta_e^{2(\frac{\gamma_e - 1}{\gamma_e})})$.

In order to utilize the equivalence principle, we then must stipulate that γ_e cannot equal one but can be near one as long as δ_e is small enough so that the term $\delta_e^{2(\frac{\gamma_e - 1}{\gamma_e})}$ does not become of order one in the downstream region of interest. If these conditions are met, then we can apply the equivalence principle and, therefore, make use of Cheng and Kirsch's³⁴

results within the entropy layer.

Assuming this form of initial behavior, we have then specified the type of breakdown of the solution due to the nearly normal character of the shock in the vicinity of the nose. It was found³⁴ that the expansion for y based on flow near the shock for initial blast wave behavior would be of the form:

$$y \sim o(\ln Y_{0*}) + o(\epsilon_e (\ln Y_{0*})^2)$$

which would then become infinite and invalid as an expansion as $Y_{0*} \rightarrow 0$, or as we approach the contact surface. This form indicates that the expansions cannot be made uniformly valid by simply altering the scale of Y_{0*} by a power of ϵ_e . In his analysis, it was determined that the scale normal to the shock should be in terms of Y_{0*} to some power which is a function of ϵ_e . We can then determine the orders of magnitude of the other variables by applying entropy and energy conservation principles.

Following Cheng and Kirsch³⁴ we then establish a new set of variables, fulfilling all the necessary conditions within the region adjacent to the contact surface. These are:

$$v_e = U_{\infty} \delta_e \bar{v}_{0e} + \dots \quad (7.4)$$

$$u_e = U_{\infty e} + \dots \quad (7.2)$$

$$p_e = \rho_{\infty e} U_{\infty e}^2 \delta_e^2 \bar{p}_{oe} + \dots \quad (7.3)$$

$$\rho_e = \rho_{\infty e} R_{e*}^2 \bar{\rho}_{oe} / \epsilon_e + \dots \quad (7.4)$$

$$y_e = \delta_e L \bar{y}_0 + \dots \quad (7.5)$$

$$x = Lx \quad (7.6)$$

$$\xi = R_{e*}^{4\epsilon_e} / \sigma_0^{2\epsilon_e} \quad (7.7)$$

Substituting these variables into the equations of motion, (1.1 to 1.5), we obtain the following set of first order results:

$$\frac{\partial \bar{p}_{oe}}{\partial \xi} = 0 \quad (8.1)$$

$$\bar{y}_{oe}^2 - \bar{y}_{oe}^2(x,0) = \frac{1}{2} \int_0^{\xi} \frac{d\tau_2}{\bar{\rho}_{oe} \tau_2} \quad (8.2)$$

$$\bar{\rho}_{oe} = \bar{\rho}_{oe} / \sigma_0 \tau_2 \quad (8.3)$$

$$\bar{v}_{oe} = \frac{\partial \bar{y}_{oe}}{\partial x} \quad (8.4)$$

The carrying out of the integration in (8.1) and (8.2) gives

$$\bar{p}_{oe} = \bar{p}_{oe}(x) \quad (9.1)$$

$$\bar{y}_{oe}^2 - \bar{y}_{oe}^2(x,0) = \sigma_0 \tau_2 / \bar{p}_{oe} \quad (9.2)$$

Matching of the inner to the outer solution is carried out by determining the behavior of the solutions in an intermediate region where they are both valid. The results³⁴ of this procedure are:

$$\left(\left(\frac{d\hat{R}_{se}}{dx}\right)^2 + \frac{d^2\hat{R}_{se}}{dx^2} \frac{\hat{R}_{se}}{2}\right) (\hat{R}_{se}^2 - R_{cs}^2) = \frac{\sigma_0}{2} \quad (10.1)$$

$$P_{oe} = \left(\frac{d\hat{R}_{se}}{dx}\right)^2 + \frac{d^2\hat{R}_{se}}{dx^2} \frac{\hat{R}_{se}}{2} \left(1 - \left(\frac{R_{cs}}{\hat{R}_{se}}\right)^2\right) \quad (10.2)$$

Equations (10.1) and (10.2) are nonlinear second order differential equations for the pressure distribution and shock position. If we can obtain an inner layer solution which gives R_{cs} as a function of P_{oe} , then we can combine these results into the above to determine \hat{R}_{se} and R_{cs} .

Internal Layer - Region 3 Analysis

Referring once again to our flow diagram to establish the system of coordinates, we have the following set of equations and boundary conditions for the downstream internal layer problem in terms of von Mises variables.

$$\frac{\partial R_i}{\partial x} = \frac{v_i}{u_i} \quad (11.1) \text{ stream line slope}$$

$$\frac{\partial R_i}{\partial \psi_i} = \frac{1}{\rho_i u_i R_i} \quad (11.2) \text{ continuity}$$

$$\frac{1}{R_i} \frac{\partial v_i}{\partial x_i} + \frac{\partial p_i}{\partial \psi_i} = 0 \quad (11.3) \text{ momentum normal to stream-line}$$

$$u_i^2 + v_i^2 + \frac{2\gamma_i}{\gamma_i - 1} \frac{p_i}{\rho_i} = g(\psi_i) \quad (11.4) \text{ Bernoulli Integral}$$

$$p_i / \rho_i^{\gamma_i} = f(\psi_i) \quad (11.5) \text{ Entropy Integral}$$

Boundary conditions at the internal upstream bow shock are:

$$\hat{p}_i = \hat{p}_{\infty i} + \frac{2\gamma_i}{\gamma_i+1} \hat{p}_{\infty i} (M_{\infty i}^2 \sin^2 \beta_i - 1) \quad (11.6)$$

$$\hat{\rho}_i = \hat{\rho}_{\infty i} / \left(\frac{\gamma_i-1}{\gamma_i+1} + \frac{2}{(\gamma_i+1) M_{\infty i}^2 \sin^2 \beta_i} \right) \quad (11.7)$$

$$\hat{u}_i = U_{\infty i} (1 - 2(\hat{M}_{\infty i}^2 \sin^2 \beta_i - 1) / (\gamma_i+1) \hat{M}_{\infty i}^2) \quad (11.8)$$

$$\hat{v}_i = U_{\infty i} (2(\hat{M}_{\infty i}^2 \sin^2 \beta_i - 1) \cot \beta_i / (\gamma_i+1) \hat{M}_{\infty i}^2) \quad (11.9)$$

Boundary conditions at the contact surface are:

$$p_{ics} = p_{ecs} \quad (11.10)$$

$$\frac{dR_{ics}}{dx} = \frac{dR_{ecs}}{dx} \quad (11.11)$$

At the axis, $R_i = 0$, the symmetry conditions are applied.

Also, in the bow region solution, we note the condition that:

$$p_{i \text{ stagnation}} = p_{e \text{ stagnation}} \quad (11.12)$$

From the external layer results, we can infer the order of magnitude of some inner layer quantities. From the contact surface condition, (11.10), we have

$$p_{ics} = p_{ecs} = O(\rho_{\infty e} U_{\infty e}^2 \delta_e^2)$$

In addition, from the stagnation point condition, (11.12),

$$\rho_{\infty i} U_{\infty i}^2 \approx O(\rho_{\infty e} U_{\infty e}^2)$$

where $\rho_{\infty i}$ is value of density along axis in front of in-

ternal shock, we find

$$\rho_{ics} = O(\rho_{\infty i_0} U_{\infty i}^2 \delta_e^2) \quad (12.1)$$

Since entropy is conserved along streamlines, we can establish the order of magnitude of density in the internal layer near the contact surface from (11.5)

$$\rho_i / \rho_i^{\gamma_i} = \rho_{i*} / \rho_{i*}^{\gamma_i}$$

For $M_{\infty i} \gg 1$, $\sin^2 \beta_i \simeq 1$ the shock conditions, (11.7) and (11.6), for the streamline which wets the contact surface become

$$\rho_{i*} = O(\rho_{\infty i_0} / \epsilon_{i_0}) \quad \rho_{i*}^{\gamma_i} = O(\rho_{\infty i_0} U_{\infty i}^2)$$

Where subscript \circ denotes normal shock location in bow region. When substituted into the entropy equation, (11.5), the result is:

$$\rho_{ics} = O(\rho_{\infty i_0} \delta_e^{2/\gamma_i} / \epsilon_{i_0}) \quad (12.2)$$

From the second contact surface condition, (11.11), we find

$$\frac{dR_{ics}}{dx} = \frac{dR_{eccs}}{dx} = \frac{v_e}{u_e} = O(\delta_e)$$

This also requires that

$$v_i/u_i = o(\delta_e) \quad (12.3)$$

near the contact surface, which is an upper bound on this ratio. Another expression which can be utilized is Bernoulli's equation, (11.4), along a streamline. Substituting (12.1 to 12.3) into this equation and assuming u_i of the form

$$u_i = U_{\infty i} + u_i''$$

we obtain

$$U_{\infty i}^2 + 2U_{\infty i}u_i'' + o(\delta_e^2 U_{\infty i}^2 + 2\delta_e^2 U_{\infty i}u_i'') + \frac{2\delta_i}{\delta_i - 1} o\left(\frac{\epsilon_{i0}}{\rho_{\infty i0}} \rho_{\infty i0} U_{\infty i}^2 \delta_e^{2-2/\delta_i}\right) = U_{\infty i}^2$$

Therefore, we find that

$$u_i'' = o\left(\delta_e^{2\left(\frac{\delta_i-1}{\delta_i}\right)}\right) \quad (12.4)$$

Therefore, we can conclude that for u_i to be constant in the first approximation in the above flow system, it is necessary that $\delta_i \neq 1$ and δ_e be small enough so that the term

$$\delta_e^{2\left(\frac{\delta_i-1}{\delta_i}\right)} \ll o(1) \quad .$$

These are the same conditions which are necessary for the external layer solution to be valid near the contact surface; therefore, we assume that this will be the case in the present problem. This leads to the result

$$u_i = o(U_{\infty i}) \quad (12.5)$$

From the contact surface condition, (12.3), we find

$$v_i = o(U_{\infty i} \delta_e) \quad (12.6)$$

We have now established the orders of magnitude of all interior variables of interest near the contact surface. We now postulate expansions for the variables based on these orders and then substitute them into the equations of motion to yield a sequence of solutions, which can be summed to give the solution to any order of accuracy for the internal layer flow.

The expansions are for $\epsilon_{i_0} \rightarrow 0$, $\delta_e \rightarrow 0$, $M_{\infty i_0} \rightarrow \infty$

$$p_i = \rho_{\infty i_0} U_{\infty i}^2 \delta_e^2 p_{oi} + \dots$$

$$\rho_i = \rho_{\infty i_0} \delta_e^2 \rho_{oi} / \epsilon_{i_0} + \dots$$

$$v_i = U_{\infty i} \delta_e v_{oi} + \dots$$

$$u_i = U_{\infty i} + \dots$$

The first order set of equations is

$$\frac{\partial p_{oi}}{\partial \psi_i} = 0 \quad (13.1)$$

$$\frac{\partial R_{oi}}{\partial \psi_i} = \frac{1}{\rho_{oi} R_{oi}} \quad (13.2)$$

$$\frac{\partial}{\partial x} (p_{oi} / \rho_{oi}) = 0 \quad (13.3)$$

$$v_{oi} = \frac{\partial R_{oi}}{\partial x} \quad (13.4)$$

Integrating, we then have

$$p_{oi} = p_{oi}(x) \quad (14.1)$$

$$R_{oi}^2 = 2 \int_0^{\Psi} \frac{d\Psi^*}{\rho_{oi}} \quad (14.2)$$

$$\rho_{oi} = \rho_{oi} \rho_{oi}^* / \rho_{oi}^* \quad (14.3)$$

Combining (14.1, 14.2 and 14.3), we obtain

$$R_{cs}^2 = \frac{2}{\rho_{oi}(x)} \int_0^{\Psi_{jet}} \frac{\rho_{oi}^*}{\rho_{oi}} d\Psi_i \quad (14.4)$$

Now that we have results for the internal and external flow, we can combine them to determine the location of the shock and contact surface, as well as find the values of the properties across the layers.

From the external flow, we have the results:

$$p_{oecs} = \left(\frac{d\hat{R}_{se}}{dx} \right)^2 + \frac{\hat{R}_{se}}{2} \left(\frac{d^2\hat{R}_{se}}{dx^2} \right) \quad (10.2)$$

$$p_{oecs} (\hat{R}_{se}^2 - R_{cs}^2) = \sigma_0/2 \quad (10.1)$$

Also from the internal flow, we have the result

$$p_{oi}(x) = \frac{2}{R_{cs}^2} \int_0^{\Psi_{jet}} \frac{\rho_{oi}^*}{\rho_{oi}} d\Psi_i \quad (14.4)$$

Since $\rho_{oe} U_{oe}^2 = \rho_{oi} U_{oi}^2$ from the stagnation point condition, then $p_{oecs} = p_{oi}(x)$. We can now combine

these relations (10.1, 10.2 and 14.4) from which property variables can be determined.

Taking (10.1) and (14.4) we have

$$P_{oeCS}(x,0) \left(\hat{R}_{se}^2 - \frac{2 \int_0^{\psi_{jet}} \frac{P_{oi}^*}{\rho_{oi}^*} d\psi_i}{P_{oeCS}} \right) = \sigma_0/2$$

or

$$P_{oeCS} \hat{R}_{se}^2 = \frac{\sigma_0}{2} + 2 \int_0^{\psi_{jet}} \frac{P_{oi}^*}{\rho_{oi}^*} d\psi_i \quad (15.1)$$

Combining (15.1) with (10.2), we then obtain for the shock shape a second order non-linear differential equation

$$\left(\frac{d\hat{R}_{se}}{dx} \right)^2 + \frac{d^2\hat{R}_{se}}{dx^2} \frac{\hat{R}_{se}}{2} \hat{R}_{se}^2 = \frac{\sigma_0}{2} + 2 \int_0^{\psi_{jet}} \frac{P_{oi}^*}{\rho_{oi}^*} d\psi_i \quad (15.2)$$

For $\bar{x}/R_{sio} \gg 1$, which is in the downstream region of interest, (15.2) admits a solution of the form

$$\hat{R}_{se} = C x^{1/2} \quad (15.3)$$

When (15.3) is substituted in (15.2), we find the value of C to be given by

$$C = \left(4\sigma_0 + 16 \int_0^{\psi_{jet}} \frac{P_{oi}^*}{\rho_{oi}^*} d\psi_i \right)^{1/4} \quad (15.4)$$

Using (15.4) in (10.2) to find $P_{oi}(x)$ (14.4) then becomes

$$\frac{C^4}{8R_{so}^2} = \frac{2}{R_{cs}^2} \int_0^{\psi_{jet}} \frac{P_{oi}^*}{\rho_{oi}^*} d\psi_i \quad (15.5)$$

Combining (15.4) and (15.5), we then obtain the following expression for the contact surface shape in terms of the shock shape

$$R_{cs} = \hat{R}_{se} / \left(\frac{\sigma_0}{4 \int_0^{\psi_{jet}} \frac{P_{oi}^*}{\rho_{oi}^*} d\psi_i} + 1 \right)^{1/2} \quad (15.6)$$

We now have determined the values of \hat{R}_{se} , R_{cs} in terms of the functions σ_0 and $\int_0^{\psi_{jet}} \frac{P_{oi}^*}{\rho_{oi}^*} d\psi_i$. These expressions are functions of the blunt interaction between the external and internal layers at the extreme upstream position in the bow region and are a result of the matching of pressures across the upstream contact surface.

We, therefore, must postulate an upstream interaction based on our solution for the bow region flow which is consistent with the approximations made in this downstream region.

For the downstream analysis, we require $\epsilon_{i0}, \epsilon_e \rightarrow 0$ $M_{oi0}, M_{oe} \rightarrow \infty$. These limits must also be applied to our bow region matching conditions which are the equality of pressure and flow deflection along the contact surface. Since our bow region internal

flow is a perturbation of the case where the shock and body surface are a spherical shell, for $\epsilon_{i0} = 0$, then we make the approximation that the upstream interaction region is spherical in nature. For the external flow, it is a well established fact³⁵ that the downstream shock surface does not depend on the details of the pressure distribution along the contact surface, but only on the total integrated pressure distribution (i.e., drag) in the axial direction, adding further validity to the use of the above assumption. Along this surface, the pressure induced by the internal flow must match that of the external flow. To first order, which is the degree of accuracy for the downstream region, the pressure change across the shock layer is zero and, therefore, we can calculate the pressure on the contact surface by simply finding the pressure level behind a spherical shock surrounding the jet flow source. For the case $M_{\infty i} \gg 1$, $\sin \beta_i \approx 1$, the expression for pressure behind the shock reduces to

$$p_i = p_{cs i} = \rho_{\infty i} U_{\infty i}^2 = \frac{\rho_{\infty i}}{\rho_{\infty e}} \rho_{\infty e} U_{\infty e}^2$$

Non-dimensionalized with respect to the external conditions, this relation becomes

$$p_{cs i} = \frac{\rho_{\infty i}}{\rho_{\infty e}} \frac{\rho_{\infty e} U_{\infty e}^2}{\rho_{\infty e} U_{\infty e}^2}$$

From the equality of stagnation pressures, this then reduces to

$$p_{cs i} = \frac{\rho_{\infty i}}{\rho_{\infty e}} = p_{cs e}$$

From the source conditions, we have

$$p_{cse} = \cos^n \frac{\pi\varphi}{2\theta_\infty}$$

With the pressure level and contact surface shape determined, we have satisfied our matching criteria and our next step is to calculate the functions σ_0 and $\int_0^{\psi_{jet}} \frac{p_{oi*}}{\rho_{oi*}} d\psi_i$. Evaluating the integral from the internal layer solution, we find

$$\int_0^{\psi_{jet}} \frac{p_{oi*}}{\rho_{oi*}} d\psi_i = \int_0^{\psi_{jet}} \cos^n \frac{\pi\varphi}{2\theta_\infty} / \cos^n \frac{\pi\varphi}{2\theta_\infty} d\psi_i = \int_0^{\psi_{jet}} d\psi_i = \int_0^{\theta_\infty} \cos^n \frac{\pi\varphi}{2\theta_\infty} \sin\varphi d\varphi$$

In this result, the upper integration limit requires some discussion. Strictly speaking, in order to calculate the pressure and density distributions over the full range of φ one would have to take account of the effect of the plume boundary and the mass flowing in the plume boundary layer on the internal shock. However, for highly underexpanded jets, there is relatively little mass flowing in this layer and, therefore, the integration of the above to the vacuum limit, $\varphi = \theta_\infty$ creates only a small error in the downstream analysis.

We now seek to determine the value of σ_0 . It can be shown that for $\bar{x}/R_{si0} \ll 1$ our postulated initial blast wave behavior for the ³⁶ shock shape can be written as

$$\hat{R}_{se} = \sqrt{2} \left(\frac{C_{DN}}{I_b} \right)^{1/4} x^{1/2}$$

Where I_b to our degree of approximation can be written as

$$I_b = \frac{6\gamma_e - \gamma_e^2 - 1}{4(\gamma_e - 1)(\gamma_e + 1)}$$

In the above C_{DN} is the nose drag coefficient of a hypothetical blunt nosed slender body, which takes on the shape of the contact surface. C_{DN} is directly related to the blunt interaction and is written as

$$C_{DN} = \int_A p_{cs} \bar{n} \cdot \bar{n}_x dA / \frac{1}{2} \rho_{\infty} U_{\infty}^2 \pi R_{sio}^2$$

Since we stipulated that $R_{cs}/\hat{R}_{se} \rightarrow 0$ as $\bar{x}/R_{sio} \rightarrow 0$ then equations(10.1) and (10.2) give

$$\left(\frac{d\hat{R}_{se}}{dx} \right)^2 + \frac{d^2\hat{R}_{se}}{dx^2} \frac{\hat{R}_{se}}{2} \hat{R}_{se}^2 = \sigma_0/2 \quad \text{as} \quad \bar{x}/R_{sio} \rightarrow 0$$

from which
$$\sigma_0 = \frac{C_{DN}}{I_b}$$

We now calculate C_{DN} based on our postulated upstream interaction. For a spherical shell interaction with the pressure distribution given by

$$p = \rho_{\infty} U_{\infty}^2 \cos^n \frac{\pi\varphi}{2\theta_0}$$

then

$$\bar{n} \cdot \bar{n}_x = \cos \varphi$$

and

$$dA = 2\pi R_{sio}^2 \sin\varphi d\varphi$$

which leads to

$$C_{DN} = 4 \int_0^{\Theta_\infty} \cos^n \frac{\pi \varphi_*}{2\Theta_\infty} \sin \varphi_* \cos \varphi_* d\varphi_*$$

As in a previous integration, we use Θ_∞ as the upper limit of integration instead of the exact result. In this case, we are further substantiated in this approximation by the fact that near $\Theta_\infty \sim \frac{\pi}{2}$ the contributions from the above integrand to C_{DN} are near zero due to the $\cos \varphi_*$ factor in the above.

With the previously calculated values, the shock shape can now be written as

$$\hat{R}_{se} = 2 \left(\frac{\int_0^{\Theta_\infty} \cos^n \frac{\pi \varphi_*}{2\Theta_\infty} \sin \varphi_* \cos \varphi_* d\varphi_*}{\frac{(6\gamma_e - \gamma_e^2 - 1)}{4(\gamma_e - 1)(\gamma_e + 1)}} + \int_0^{\Theta_\infty} \cos^n \frac{\pi \varphi_*}{2\Theta_\infty} \sin \varphi_* d\varphi_* \right)^{1/4} \chi^{1/2}$$

Also from (15.6) we have

$$R_{cs} = \hat{R}_{se} / \left(\frac{\int_0^{\Theta_\infty} \cos^n \frac{\pi \varphi_*}{2\Theta_\infty} \sin \varphi_* \cos \varphi_* d\varphi_*}{\frac{(6\gamma_e - \gamma_e^2 - 1)}{4(\gamma_e - 1)(\gamma_e + 1)}} \int_0^{\Theta_\infty} \cos^n \frac{\pi \varphi_*}{2\Theta_\infty} \sin \varphi_* d\varphi_* + 1 \right)^{1/2}$$

We are now in a position to calculate layer properties based on these results. For the external flow we have

$$p_0 = \left(\frac{d\hat{R}_{se}}{dx} \right)^2 + \frac{d^2\hat{R}_{se}}{dx^2} \frac{\hat{R}_{se}}{2} \left(1 - \left(\frac{R_*}{R_{se}} \right)^2 \right)$$

With

$$\hat{R}_{se} = C \chi^{1/2} \quad p_0 = \frac{C^2}{8\chi} (1 + \Psi_*/\hat{\Psi})$$

This distribution will be valid throughout the external layer.

The density distribution is given by

$$\rho_0 = (1 + \psi_*/\hat{\psi})\psi_*/2\hat{\psi}$$

The result is not strictly valid since the density is not zero at the contact surface.

When referenced to values at the shock, the results become

$$\rho_e/\hat{\rho}_e = 1/2 (1 + \psi_*/\hat{\psi}) \quad ** \quad (16.1)$$

$$\rho_e/\hat{\rho}_e = 1/2 (\psi_*/\hat{\psi})(1 + \psi_*/\hat{\psi}) \quad ** \quad (16.2)$$

$$T_e/\hat{T}_e = \hat{\psi}/\psi_* \quad ** \quad (16.3)$$

For the internal flow, we have the following results:

$$\rho_{oi} = C^2/8x \quad (16.4)$$

$$\rho_{oi} = C^2/8x \quad (16.5)$$

$$v_{oi} = \sqrt{16}/C \int_0^{\psi_{jet}} d\psi / 2x^{1/2} = \frac{\sqrt{16}}{C} \frac{\psi_*^{1/2}}{2x^{1/2}} \quad (16.6)$$

When referenced to values at the shock, the above become

$$\rho_i/\hat{\rho}_e = 1/2 \quad (16.7)$$

$$\rho_i/\hat{\rho}_e = \frac{C^2}{8x} \frac{\rho_{oi} \epsilon_e}{\rho_{oe} \epsilon_{io}} \quad (16.8)$$

$$v_i/\hat{v}_e = \frac{\sqrt{16}}{C^2} \psi_* \frac{U_{oi}}{U_{oe}} \quad (16.9)$$

** Not valid at contact surface

The first order solution obtained thusfar from the hypersonic small disturbance form of the Newton-Busemann approximation, is adequate to describe layer thicknesses, pressures, and densities in the far field region near the contact surface. However, due to the assumption of $\gamma_{e,i} \rightarrow 1$ the temperature to the first approximation is in considerable error for $\bar{x}/R_{s,i_0} \gg 1$. This is because the expression for temperature, $\frac{T}{T_s} = \left(\frac{P}{P_s}\right)^{\frac{\gamma-1}{\gamma}}$ gives the unrealistic result that for all $\bar{x}/R_{s,i_0}$, $\frac{T}{T_s} \rightarrow 1$ as $\gamma \rightarrow 1$. This result is acceptable for small $\bar{x}/R_{s,i_0}$, where P/P_s is of order one, however, for $\bar{x}/R_{s,i_0} \gg 1$ P/P_s is small and even for γ near one $\frac{T}{T_s} \ll 1$.

To obtain a more accurate value for temperature near the contact surface, the unexpanded forms of the variables in terms of δ will be retained. Referring to Cheng and Kirsch³⁴, the unexpanded for δ results for the "entropy wake" are

$$\hat{R}_{se}^2 - R_{cs}^2 = \sigma \zeta / P_e^{1/\delta_e} \quad (17.1)$$

$$\rho_e = P_e^{1/\delta_e} / \sigma \zeta \quad (17.2)$$

The retention of the exponent, $1/\delta_e$, in (17.1), (17.2) is justified because the relative errors are smaller than any integral power of ϵ_e ³⁴. Applying the same reasoning to the internal layer expressions, (14.3), (14.4), we obtain

$$\rho_i = \left(\frac{P_i}{P_{i*}}\right)^{1/\delta_i} \rho_{i*} \quad (17.3)$$

$$R_{cs}^2 = \frac{1}{P_i^{1/8i}} \int_0^{\psi_{jet}} \frac{P_{i*}^{1/8i}}{\rho_{i*}} d\psi_i \quad (17.4)$$

Matching (17.1) to the near shock layer results (6.1) and then combining with (17.4) we obtain

$$P_e^{1/8e} (\hat{R}_{se}^2 - R_{cs}^2) = \sigma/2$$

This is the same form as expression (10.1) with P_0 replaced by $P_e^{1/8e}$. To the accuracy needed for $\bar{x}/R_{sio} \gg 1$ it is adequate to use the formal result (10.1) which utilizes P_0 instead of $P_e^{1/8e}$. However, for the distribution of temperature, we use

$$\frac{T}{T_s} = \left(\frac{P}{P_s} \right)^{\frac{\gamma-1}{\gamma}} \quad (17.5)$$

for both the external near the contact surface and internal flow. This expression will give accurate values of $\frac{T}{T_s}$ for small P/P_s as well as for P/P_s near one. To be consistent, we also use the density expression

$$\frac{\rho}{\rho_s} = \left(\frac{P}{P_s} \right)^{1/\gamma} \quad (17.6)$$

instead of $\rho = \rho_s P/P_s$

Making use of (17.5) and (17.6) and the expression for pressure (16.1) the temperature and density distributions near the contact surface for the external flow and within the internal layer are

$$T = T_s \left(\frac{C^2}{8 \times P_s} \right)^{\frac{\gamma-1}{\gamma}}$$

$$\rho = \rho_s \left(\frac{C^2}{8 \times P_s} \right)^{1/\gamma}$$

The above expressions, as well as those previously found, are used to predict geometry and flow properties in the far field region for typical systems of interest.

DISCUSSION OF RESULTS

Examining the far field analytic solution, we find that an experimental simulation of an actual flow requires matching $\gamma_j, \gamma_e, \theta_\infty, n$ and R_{sio} , the same scaling parameters used in the bow region simulation. If, in addition to the above, $P_{oj}/P_{\infty e}$ is matched then the bow, corner and far field geometry will be simulated. For a given system with fixed ambient and exhaust gas composition (i.e., γ_e, γ_j fixed) and nozzle conditions (i.e., θ_∞, n) the flow geometry will scale as does the bow region with R_{sio} or $\gamma^{1/2}$. If $M_{\infty e}$ is also assumed to be fixed, then the bow, corner and far field regions will all scale with R_{sio} . Calculations of far field flow geometry and properties have been carried out and the results appear in figures (21) to (24). As in the bow analysis, the far field geometry is sensitive to the exponent used in the exhaust plume model. From figures (21) and (22) it can be observed that the internal layer occupies a large fraction of the shock layer flow. This is due to the greater amount of strongly shocked, and hence lower density, gas in the internal flow compared to that in the external flow.

As shown in figures (21) and (22), increasing θ_∞ or γ_j results in the moving outward of the shock and contact surfaces. This behavior is consistent with the results from the bow region. Also, near the contact surface, temperature, pressure, and density for the internal and external flow increase for increases in θ_∞ or γ_j .

The effect of the internal layer flow on the external flow pressure, density, and temperature is to maintain them at a higher level than that created by just the bow interaction. This can be seen from expression 15.4 in the far field analysis section where the coefficient for the pressure decay expression consists of the normal bow interaction term plus the effect of inner layer thickness.

In figures (23) and (24) the detailed property distributions across the layers are given for the same "cold" jet and actual jet cases that were analyzed in the bow section.

Consistent with the bow region results, we find that the actual jet case shown in figure (24) has a hot, low density external layer, which flows over a cooler and more dense inner layer. If allowed, considerable heat transfer and mixing between the external and internal layers would occur. The "cold" jet case does not exhibit as sharp a change in flow properties across the contact surface as that of the actual case.

This indicates that "cold" jet experiments must be interpreted carefully in light of the greater mixing and heat transfer effects for the actual system versus the "cold" jet simulation.

CONCLUSIONS

Analytical techniques for predicting flow properties in the bow and far field regions of an opposed hypersonic plume in a hypersonic stream have been developed. It has been shown that they are valid for a wide range of altitude and jet thrusts for typical systems. The influence of the corner region flow on the bow and far field flow predictions has been shown to be negligible. Consequently, only a qualitative outline of the flow processes in this region are given.

Some of the major results of the analyses and calculations are:

1. Experimental simulation depends on the matching of $\gamma_e, \gamma_j, \theta_\infty, n, R_{sio}, P_{oj}/P_{oe}$
2. For a given system with fixed ambient and exhaust composition, external Mach number and nozzle conditions (i.e., fixed $\gamma_e, \gamma_j, \theta_\infty, n, M_{oe}$) the entire flow geometry will scale with R_{sio} or $\pi^{1/2}$.
3. This analysis confirms the good accuracy of the Newtonian impact analysis when applied to the axisymmetric bow region, and suggests that the extension of this simple technique to predict asymmetric bow geometry might be successful.
4. The bow and far field solutions are sensitive to the exhaust plume model exponent used and consequently for accurate predictions of flow properties an accurate plume model must be utilized.

5. Penetration of the intercepting shock layer flow into the internal layer is considerable. However, the influence on the bow and far field properties is small.
6. Good agreement is found between a calculated bow region geometry and an experimental result.
7. Calculations show that mixing and heat transfer effects between the hot external and cooler internal layers are more pronounced in the actual case than in the experimental "cold" jet simulation.
8. Increasing the primary system design parameters Θ_{∞} and γ_j^* with all other parameters fixed results in
 - a. The thickening of internal and external layers in the bow and far field regions
 - b. An increase in radius of curvature of the contact surface and thereby an increase in bluntness for the bow region
 - c. An increase in the angle between the far field external shock and free stream direction
 - d. A higher level of pressure density and temperature both across and along the internal and external layer flows.

* Θ_{∞} is related to nozzle exit Mach number and angle and exhaust gas composition. For a fixed composition, increasing nozzle exit angle or decreasing exit Mach number gives increases in Θ_{∞} . γ_j^* is related to exhaust gas composition which in general will decrease as the degrees of freedom or the complexity of the exhaust molecules increase.

9. The effect of the internal layer on the far field region properties is to maintain the pressure, density, and temperature of the flow at a higher level than that which would be created by the bow region interaction with the far field internal layer flow absent.

For high Reynolds' number flows the present technique may be extended to treat mixing effects along the contact surface by the use of boundary layer methods. Also, equilibrium chemistry effects may be easily incorporated into the present model through use of Mollier charts.

Further extension of the bow layer technique to include viscous chemically reacting and merged layer effects requires considerably more effort than the above extensions. In this regard, an advantage of the present technique over the numerical technique of reference (7) is that a complete solution of the bow region requires approximately 13 seconds on an IBM 360-65, whereas the numerical technique requires 120 seconds on the much faster CDC 6600. This economy may prove to be significant in extending the above techniques to be able to predict viscous chemically reacting or merged layer bow properties where an order of magnitude increase in computational times is expected. This makes the technique of reference (7) uneconomical for use in parametric calculations whereas the present technique would still fall within the practical time limitation for these calculations.

REFERENCES

1. Romeo, D.J. and Sterrett, J.R., "Exploratory Investigation of the Effect of a Forward-Facing Jet on the Bow Shock of a Blunt Body in a Mach 6 Free Stream", NASA TN - D-1605 (1963)
2. Charwat, A.F. and Faulmann, D., "Investigation of the Flow and Drag Due to Control Jets Discharging Upstream into a Supersonic Flow", Proceedings of the XVth International Congress, Warszawa 1964, Vol. III pp. 85-114
3. Finley, P.J., "The Flow of a Jet from a Body Opposing a Supersonic Free Stream", J. Fluid Mech., 26, pp. 337-368, (1966)
4. Cassanova, R.A. and Wu, Ying-Chu Lin, "Flow Field of a Sonic Jet Exhausting Counter to a Low-Density Supersonic Airstream", The Physics of Fluids, 12, pp. 2511-2514 (1969)
5. Smithson, H.K., Price, L.L. and Whitfield, D.L., "Wind Tunnel Testing of Interactions of High Altitude Rocket Plumes with the Free Stream", AEDC-TR-71-118, July 1971
6. Laurmann, J.A., "Elementary Newtonian Theory for the Interaction of Two Opposing Hypersonic Streams", Institute for Defense Analysis, Research Paper P-509, July 1969
7. Rudman, S. and Vaglio-Laurin, R., "Flow Patterns and Regimes for Retro-Plumes", Advanced Technology Laboratories, Inc., Report ATL-TR-154, January 1971
8. Hamel, B.B. and Willis, D.R., "Kinetic Theory of Source Flow Expansion with Application to Free Jet", The Physics of Fluids, 9, pp. 829-841, (1966)
9. Simon, G.A., "Rarefaction Effects in High-Altitude Rocket Plumes", A.I.A.A. J., 10, pp. 296-300 (1972)
10. Bush, W.B., "On the Viscous Hypersonic Blunt Body Problem", J. Fluid Mech., 20, pp. 353-367 (1964)
11. Probststein, R.F., "Shock Wave and Flow Field Development in Hypersonic Re-entry", ARS J., 31, pp. 185-194 (1961)
12. Adams, M. and Probststein, R., "Jet Propulsion", Vol. 28, pp. 86-89, 1958

REFERENCES (continued)

13. Van Dyke, Milton, "Second-Order Compressible Boundary Layer Theory with Application to Blunt Bodies in Hypersonic Flow", Hypersonic Flow Research, Progress in Astronautics and Rocketry, Vol. 7, ed. F. R. Riddell, Academic Press, N.Y., 1962
14. Cheng, H.K., "Recent Advances in Hypersonic Flow Research", A.I.A.A. J., 1, pp. 295-310 (1963)
15. Boynton, F.P., "Highly Underexpanded Jet Structure: Exact and Approximate Calculations", A.I.A.A. J. 5, pp. 1703-1704, (1967)
16. Ashkenas, H., and Sherman, F.S., "The Structure and Utilization of Supersonic Free Jets in Low Density Wind Tunnels", Rarefied Gas Dynamics, Vol. II, ed. J. H. de Leeuw, Academic Press, N.Y., 1966
17. Albin, F.A., "Approximate Computation of Underexpanded Jet Structure", A.I.A.A. J. 3, pp. 1535-1537, (1965)
18. Mirels, H. and Mullen, J.F., "Expansion of Gas Clouds and Hypersonic Jets Bounded by a Vacuum", A.I.A.A. J., 1, pp. 596-602, (1963)
19. Hill, J.A.F. and Habert, R.H., "Gas Dynamics of High Altitude Missile Trails", MITHRAS Inc., Report No. MC61-13-R1, 1963
20. Andrews, E.H., Jr., Vick, A.R. and Craidon, C.B., "Theoretical Boundaries and Internal Characteristics of Exhaust Plumes from Three Different Supersonic Nozzles", TM D-2650, March 1965, NASA Washington, D.C.
21. Chester, W., "Supersonic Flow Past a Bluff Body with a Detached Shock, Part II, Axisymmetric Body, J. Fluid Mech., 1, pp. 490-497, (1956)
22. Freeman, N.C., "On the Theory of Hypersonic Flow Past Plane and Axially Symmetric Bluff Bodies", J. Fluid Mech., 1, pp. 366-387, (1956)
23. Cole, J.D., Perturbation Methods in Applied Mathematics, Blaisdell Publishing Co., Mass., 1968
24. Romeo, D.J. and Sterrett, J.R., "Flow Field for Sonic Jet Exhausting Counter to a Hypersonic Mainstream", A.I.A.A. J., 3, pp. 544-546, (1965)

REFERENCES (continued)

25. Chernyi, G.G., Introduction to Hypersonic Flow, Academic Press, N.Y., 1961
26. Jarvinen, P.O. and Adams, R.H., "The Effects of Retro-rockets on the Aerodynamic Characteristics of Conical Aero-shell Planetary Entry Vehicles", A.I.A.A. 8th Aerospace Sciences Meeting, New York, N.Y., A.I.A.A. Paper No. 70-219, 19-21, January 1970
27. Charwat, A.F., "Boundary of Underexpanded Axisymmetric Jets Issuing Into Still Air", A.I.A.A. J. 2, pp. 161-163, (1964)
28. Latvala, E.K. and Anderson, T.P., "Studies of the Spreading of Rocket Exhaust Jets at High Altitudes", Planetary and Space Science, 4, pp. 77-91, (1961)
29. Luce, R.W. and Jarvinen, P.O., "An Approximate Method for Predicting Plume Sizes for Nozzle Flow into Still Air", A.I.A.A. J., 6, pp. 182-184 (1968)
30. Hayes, W.D. and Probst, R.F., Hypersonic Flow Theory, Academic Press, New York, N.Y., 1959
31. D'Attorre, L., "Experimental and Theoretical Studies of Underexpanded Jets Near the Mach Disc, - Appendix", General Dynamics Astronautics Report GDA-DBE-64-008, February 1964
32. Sterrett, J.R. and Barber, J.B., "A Theoretical and Experimental Investigation of Secondary Jets in a Mach 6 Free Stream with Emphasis on the Structure of the Jet and Separation Ahead of the Jet", Separated Flows Part 2, AGARD Conference Proceedings, No. 4, May 1966
33. Cole, J.D., "Newtonian Flow Theory for Slender Bodies", J. Aero. Science, 24, pp. 448-455, (1957)
34. Cheng, H.K. and Kirsch, J.W., "On the Gas Dynamics of an Intense Explosion with an Expanding Contact Surface", J. Fluid Mech. 39, pp. 289-305, (1969)
35. Cox, R.N. and Crabtree, L.F., Elements of Hypersonic Aerodynamics, Academic Press, New York, N.Y., 1965, page 135
36. Mirels, H., "Hypersonic Flow over Slender Bodies Associated with Power-Law Shocks", Advances in Applied Mechanics, Vol. VII, Academic Press, New York, N.Y. 1962

Appendix (A)
Bow Initializing Scheme

To integrate the bow region equations for points away from the axis, we must first obtain the initial radii of curvatures and positions of the shocks at the axis. Writing equations (28.1), (28.2), (58.1) and (58.2) in the form

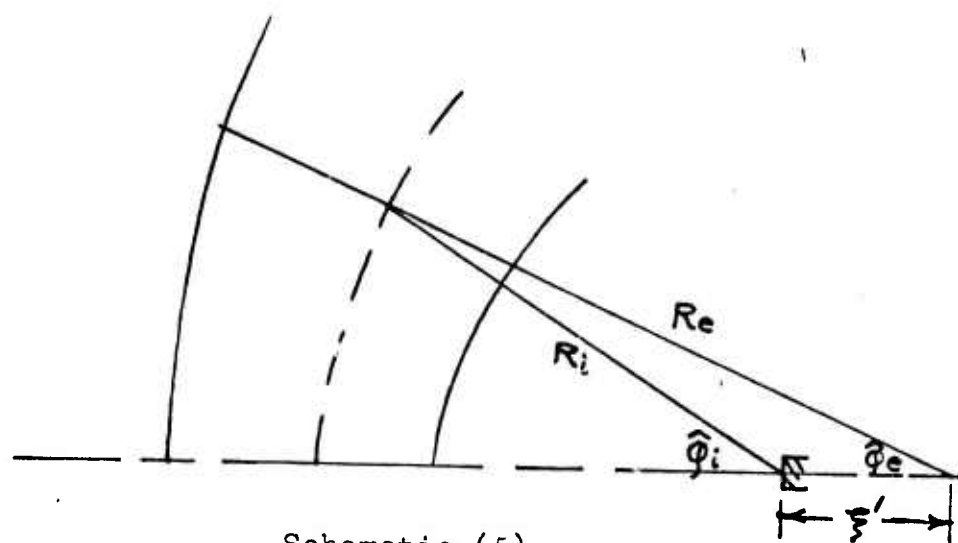
$$y_i = A(a_i) + B(a_i) \hat{\phi}_i^2 \quad (1)$$

$$p_i = C(a_i) + D(a_i) \hat{\phi}_i^2 \quad (2)$$

$$y_e = \bar{A}(a_e) + \bar{B}(a_e) \hat{\phi}_e^2 \quad (3)$$

$$p_e = \bar{C}(a_e) + \bar{D}(a_e) \hat{\phi}_e^2 \quad (4)$$

we develop expressions for $\hat{\phi}_i/\hat{\phi}_e$ and shock radii of curvatures R_{sio}/R_{se} . The geometry which relates the internal flow parameters to those of the external flow is illustrated in schematic (5)



In the above illustration

$$R_i = R_{sio} (1 + a_i \hat{\varphi}_i^2 + A(a_i) + (B(a_i)) \hat{\varphi}_i^2) \quad (5)$$

$$R_e = R_{se} (1 + a_e \hat{\varphi}_e^2 - \bar{A}(a_e) - \bar{B}(a_e) \hat{\varphi}_e^2) \quad (6)$$

Referring to schematic (5) we can write for

Angle matching

$$\hat{\varphi}_i = \hat{\varphi}_e + \frac{2(a_i + B - 2a_i^2 A) \hat{\varphi}_i}{(1+A)} + \frac{2(a_e + 2a_e^2 \bar{A} - \bar{B}) \hat{\varphi}_e}{(1-\bar{A})} \quad (7)$$

Pressure Matching

$$\hat{\varphi}_e / \hat{\varphi}_i = \left(\frac{D\bar{C}}{B\bar{C}} \right)^{1/2} \quad (8)$$

We now have two equations with three unknowns $\hat{\varphi}_e / \hat{\varphi}_i, a_e, a_i$. Consequently, we must relax one of the parameters a_i, a_e in order to obtain a unique solution. Choosing $a_i = 0$ the expressions for $A(a_i), B(a_i), C(a_i)$ and $D(a_i)$ simplify considerably.

Substituting (8) into (7) we obtain a_e which also gives $\hat{\varphi}_e / \hat{\varphi}_i$. From these results the ratio of shock radii of curvatures at the axis, R_{sio} / R_{se} , and the relative position of their centers must be obtained. Referring once again to schematic (5) we have from geometry

$$\frac{\sin(\pi - \hat{\varphi}_i)}{R_e} = \frac{\sin \hat{\varphi}_e}{R_i} = \frac{\sin(\hat{\varphi}_i - \hat{\varphi}_e)}{r'}$$

For small values of the angles we can write

$$\frac{\hat{\varphi}_i}{\hat{\varphi}_e} = \frac{R_{se} (1 - \bar{A} + (a_e - \bar{B}) \hat{\varphi}_e^2)}{R_{sio} (1 + A + B \hat{\varphi}_i^2)}$$

For the initial point, R_{se}/R_{sio} can be obtained.

The distance between their centers is then given by

$$\frac{z'}{R_{se}} = \frac{R_e}{R_{se}} \left(1 - \frac{\hat{\phi}_e}{\phi_i} \right)$$

Having obtained the ratio of the radii of curvatures and their relative positions at the axis, we then use these quantities as input data to the computer program, which predicts bow properties for regions away from the axis of symmetry.

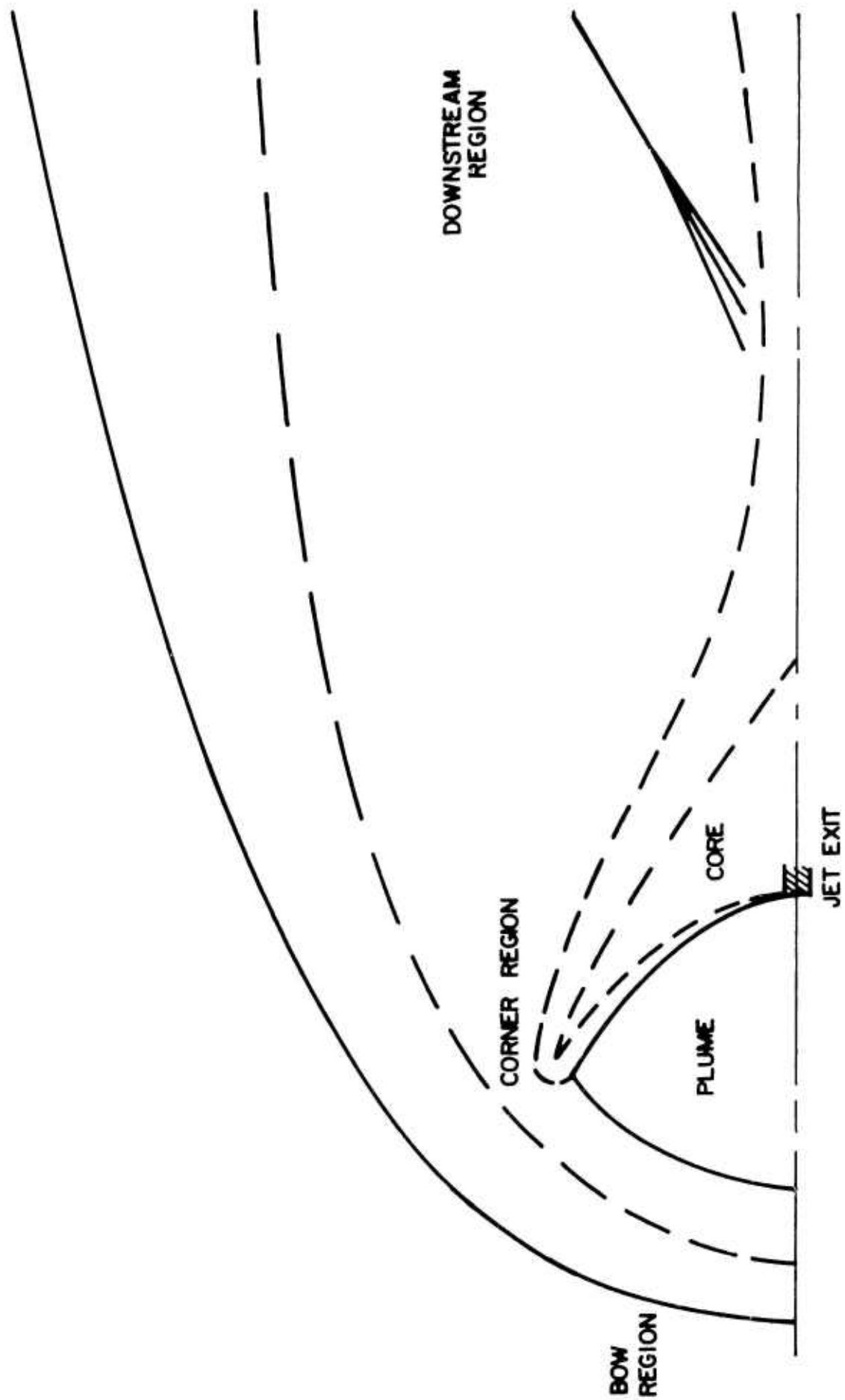


FIG. 1 SCHEMATIC OF JET AND EXTERNAL FLOW INTERACTION

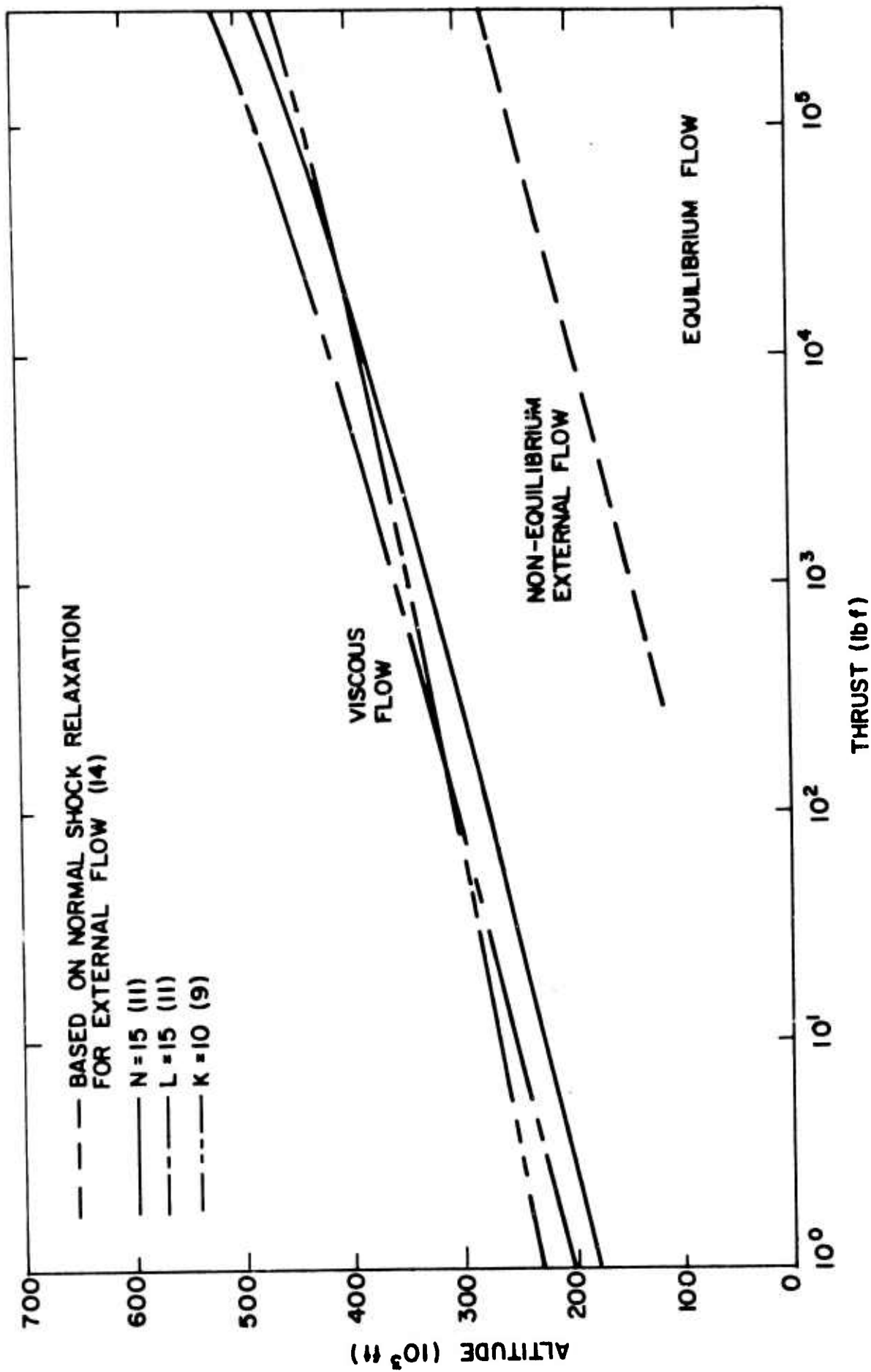


FIG. 2 FLOW REGIMES

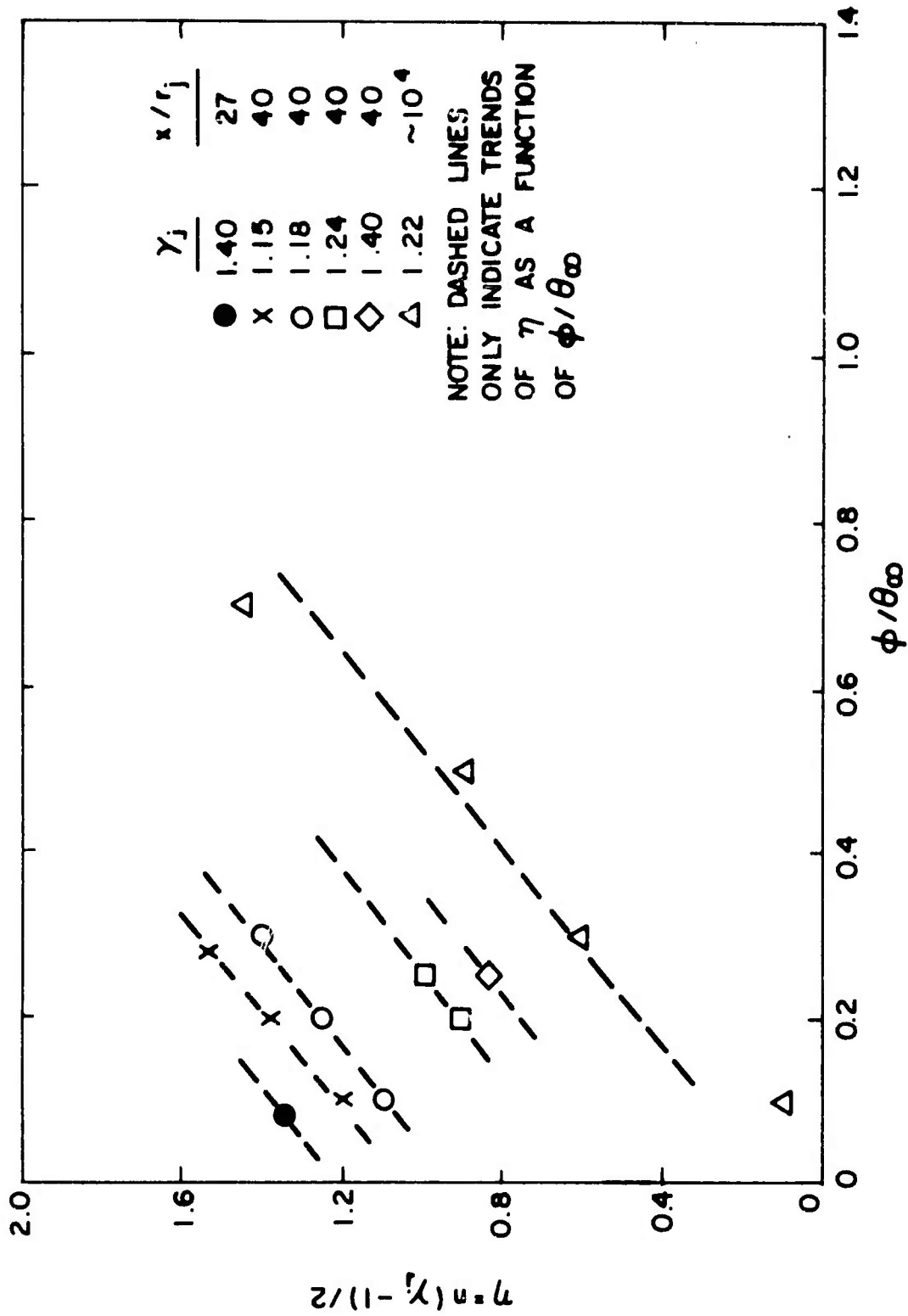


FIG. 3 UNDISTURBED PLUME MODEL EXPONENT AS A FUNCTION OF ANGLE AND DISTANCE

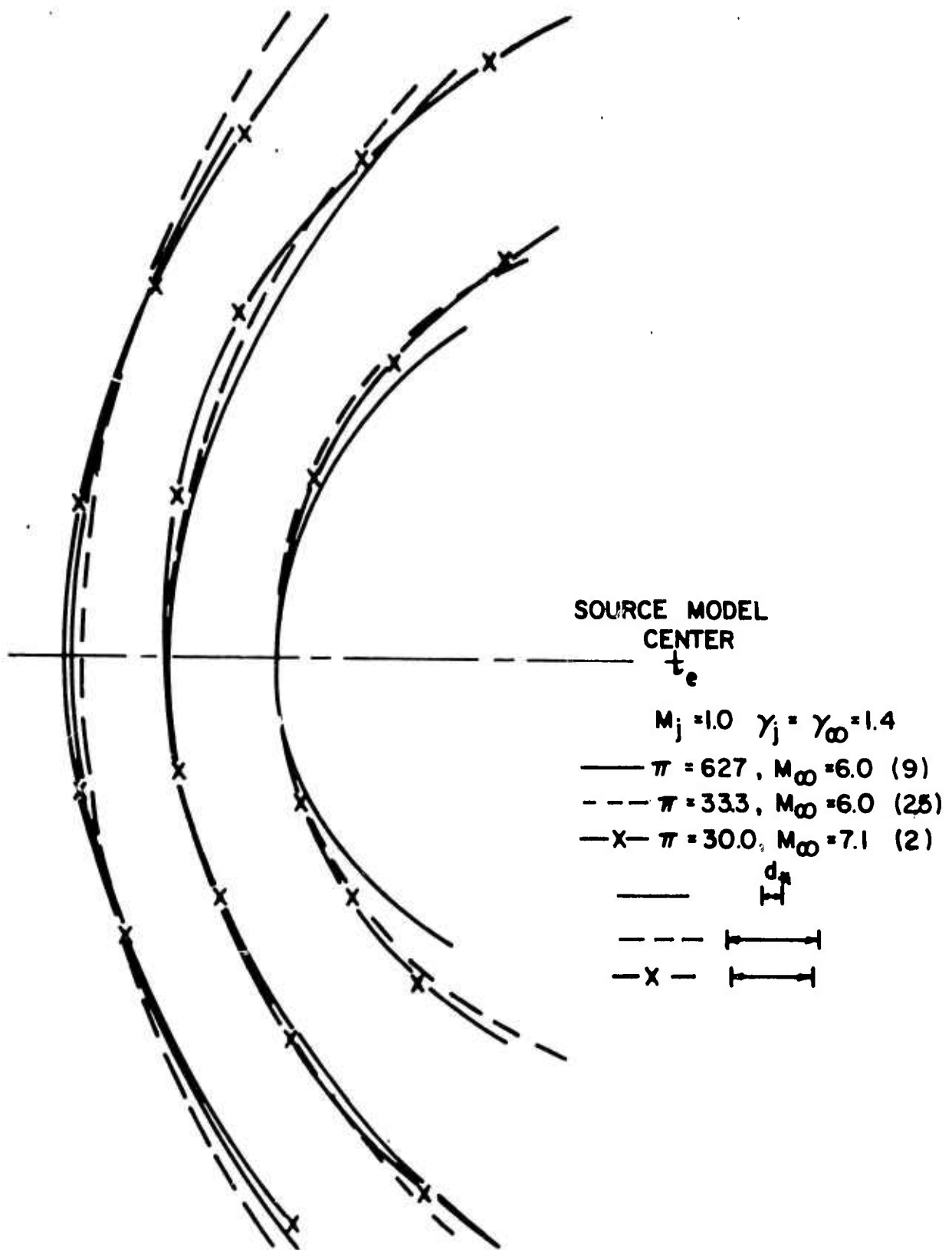
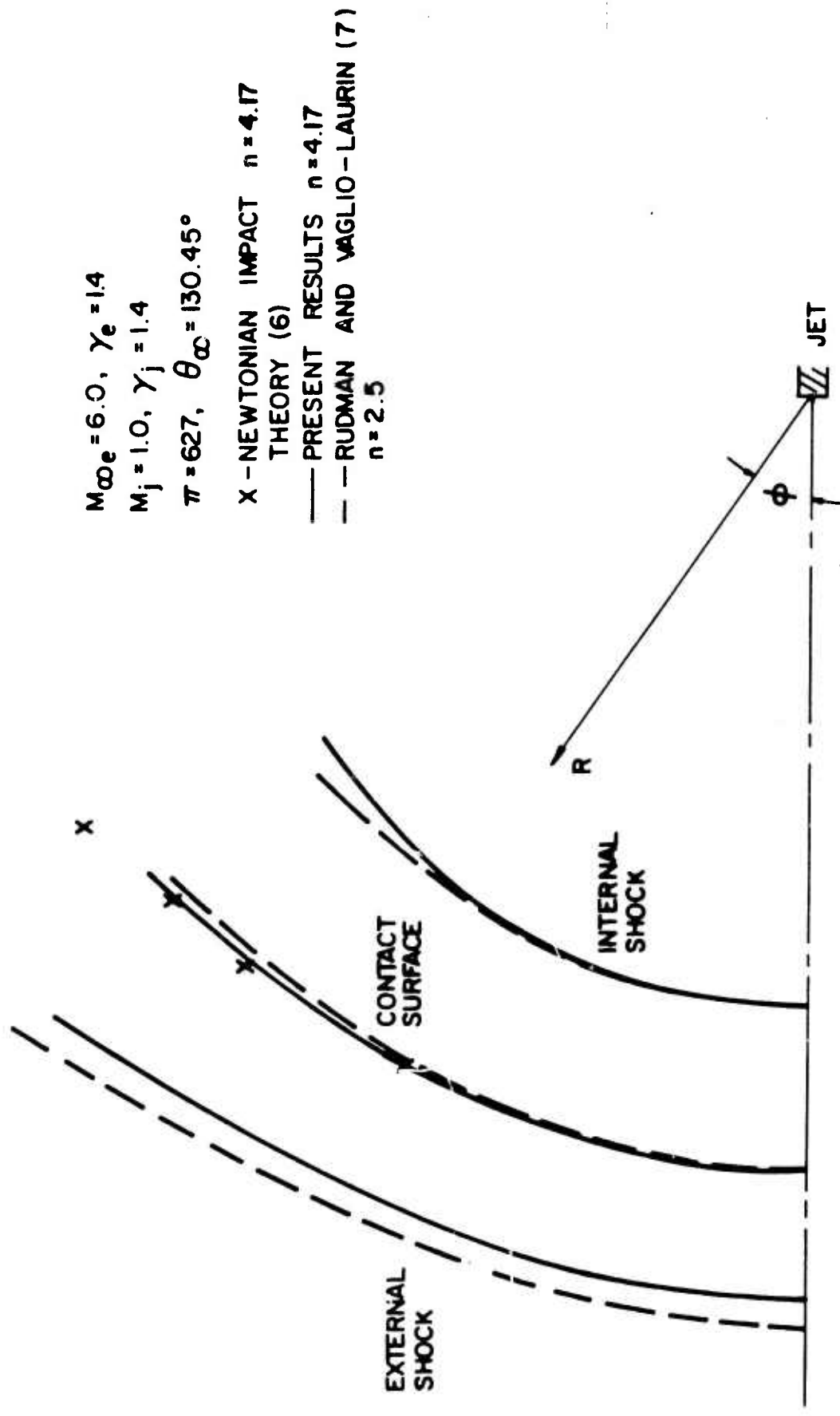


FIG. 4 EXPERIMENTALLY DETERMINED SHOCK AND CONTACT SURFACE LOCATIONS REFERRED TO R_{s10}



$M_{\infty e} = 6.0, \gamma_e = 1.4$

$M_j = 1.0, \gamma_j = 1.4$

$\pi = 627, \theta_{\infty} = 130.45^\circ$

X - NEWTONIAN IMPACT $n = 4.17$
THEORY (6)

— PRESENT RESULTS $n = 4.17$

- - - RUDMAN AND VAGLIO-LAURIN (7)
 $n = 2.5$

FIG. 5 PREDICTED CONTACT SURFACE SHAPES

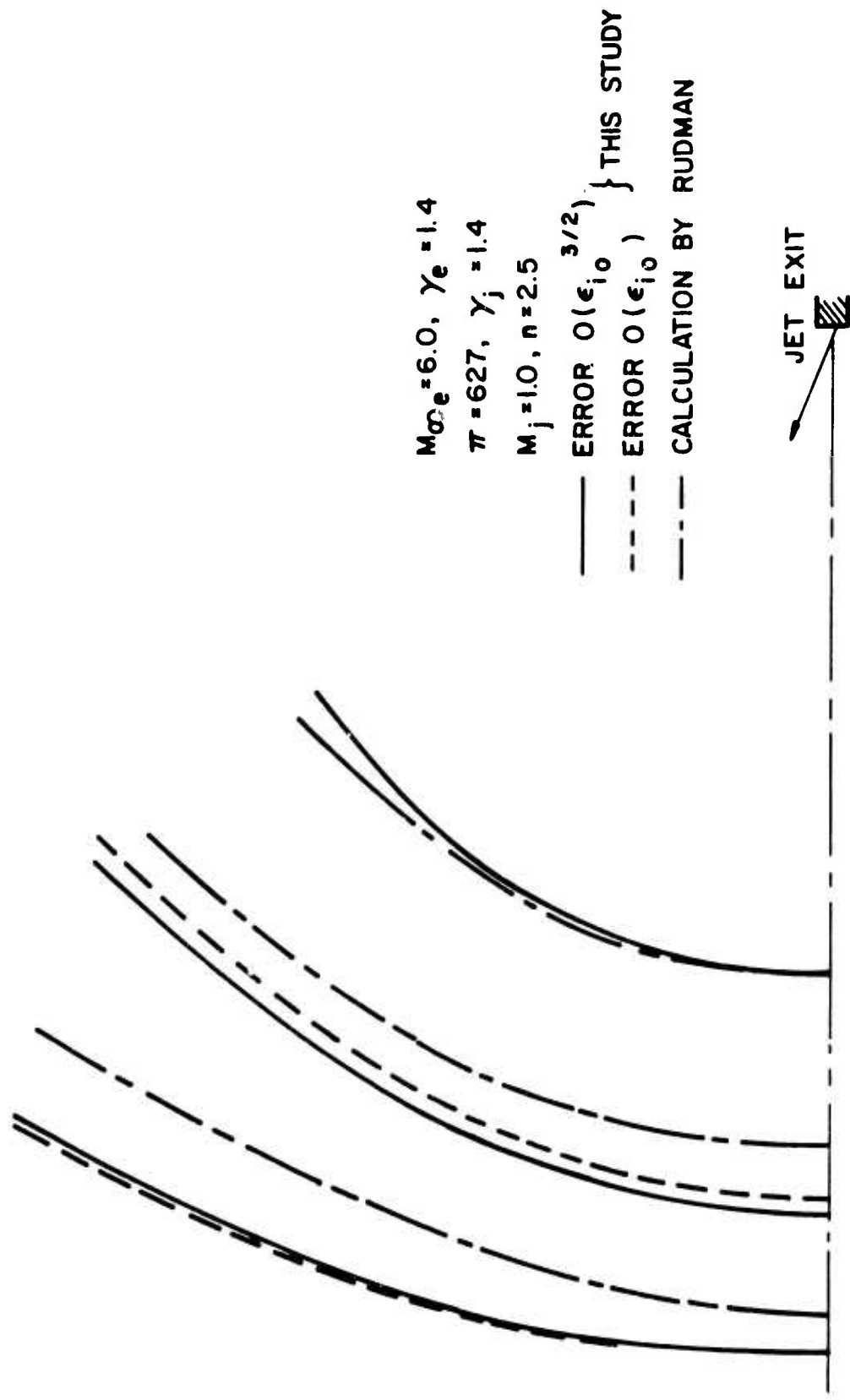


FIG. 6 COMPARISON OF SHOCK AND CONTACT SURFACE POSITIONS

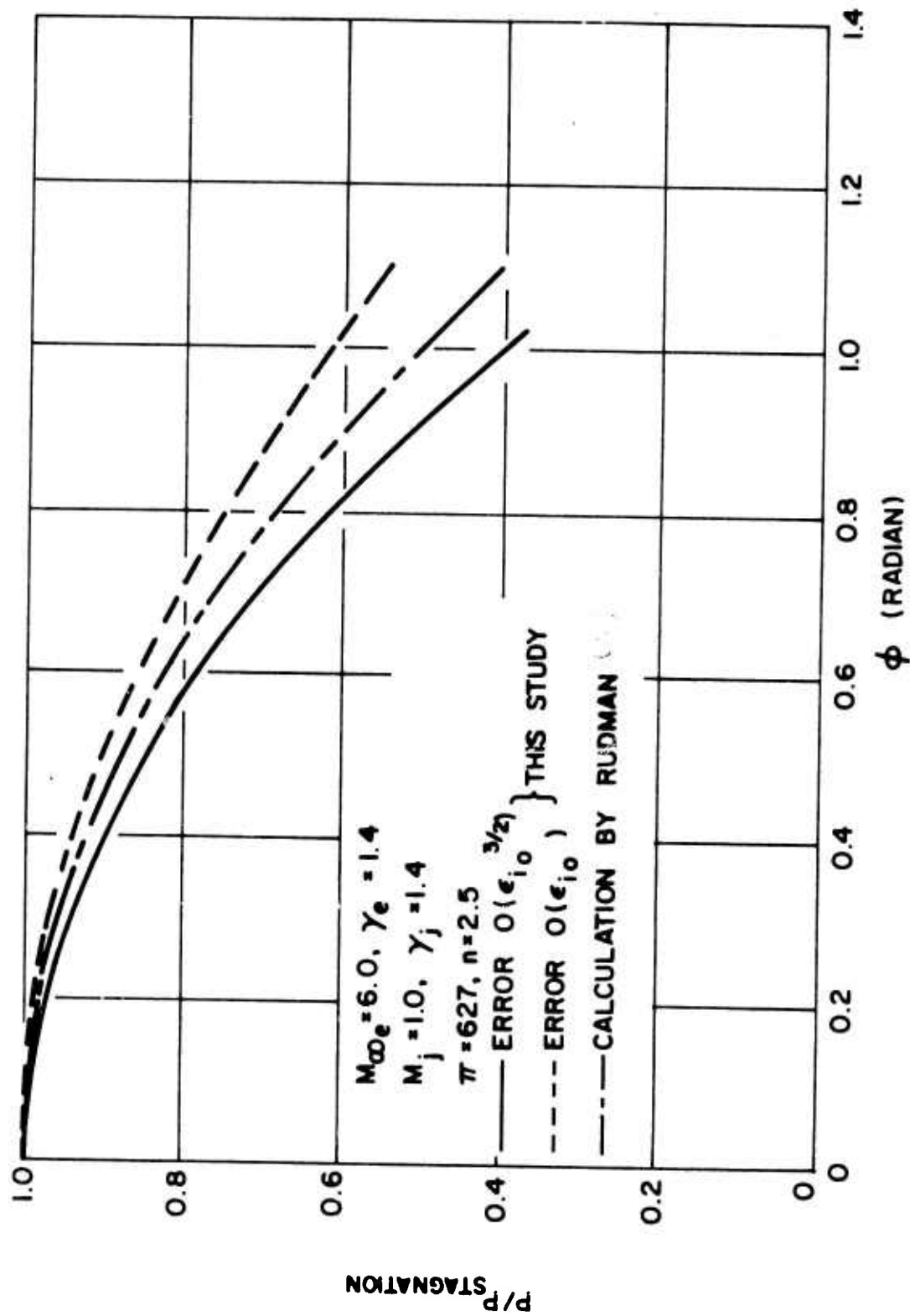


FIG. 7 COMPARISON OF CONTACT SURFACE PRESSURE DISTRIBUTIONS

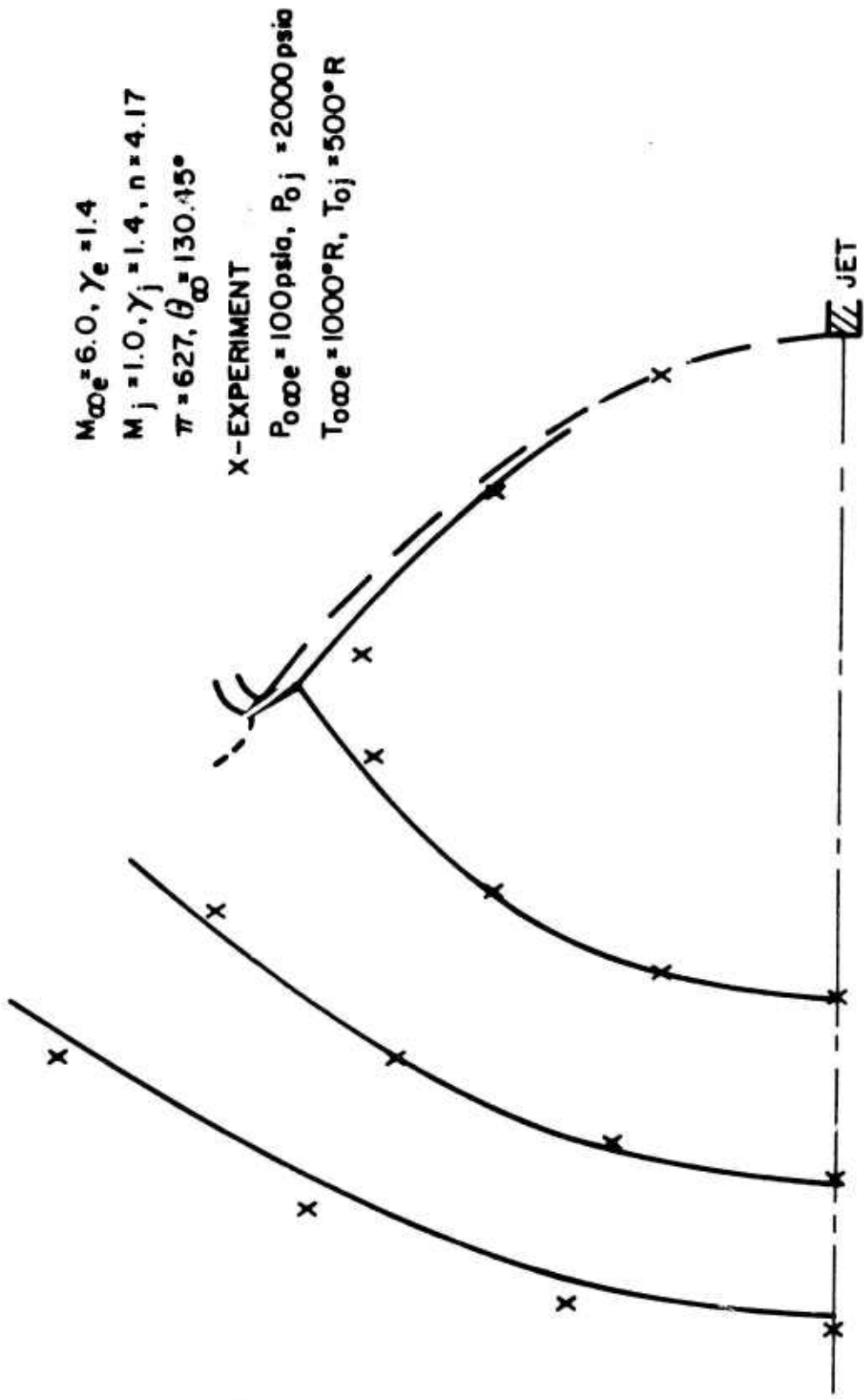


FIG. 8 COMPARISON OF CALCULATED SHOCKS AND CONTACT SURFACE POSITIONS WITH EXPERIMENTAL RESULTS OF ZAKKAY

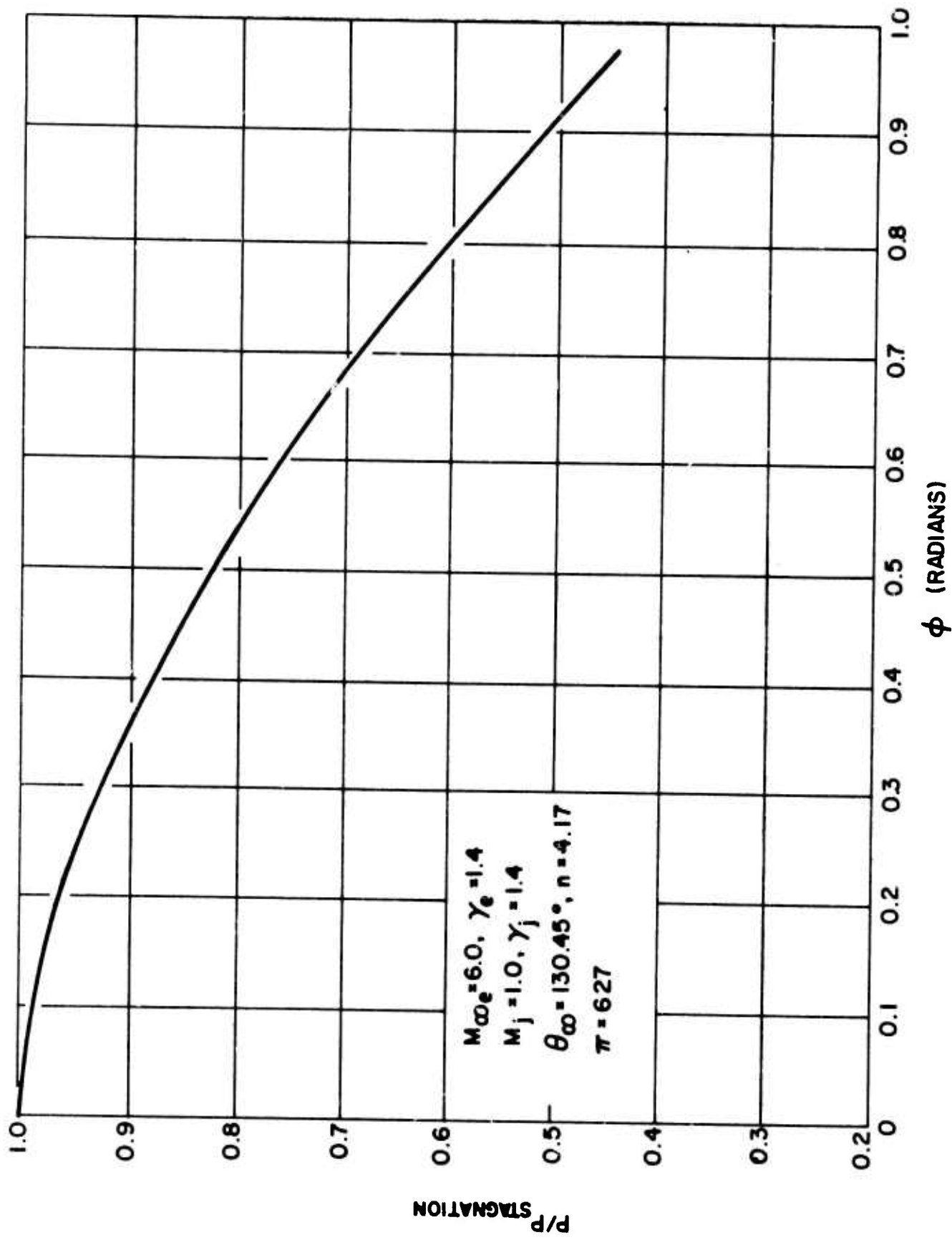


FIG. 9 CONTACT SURFACE PRESSURE DISTRIBUTION

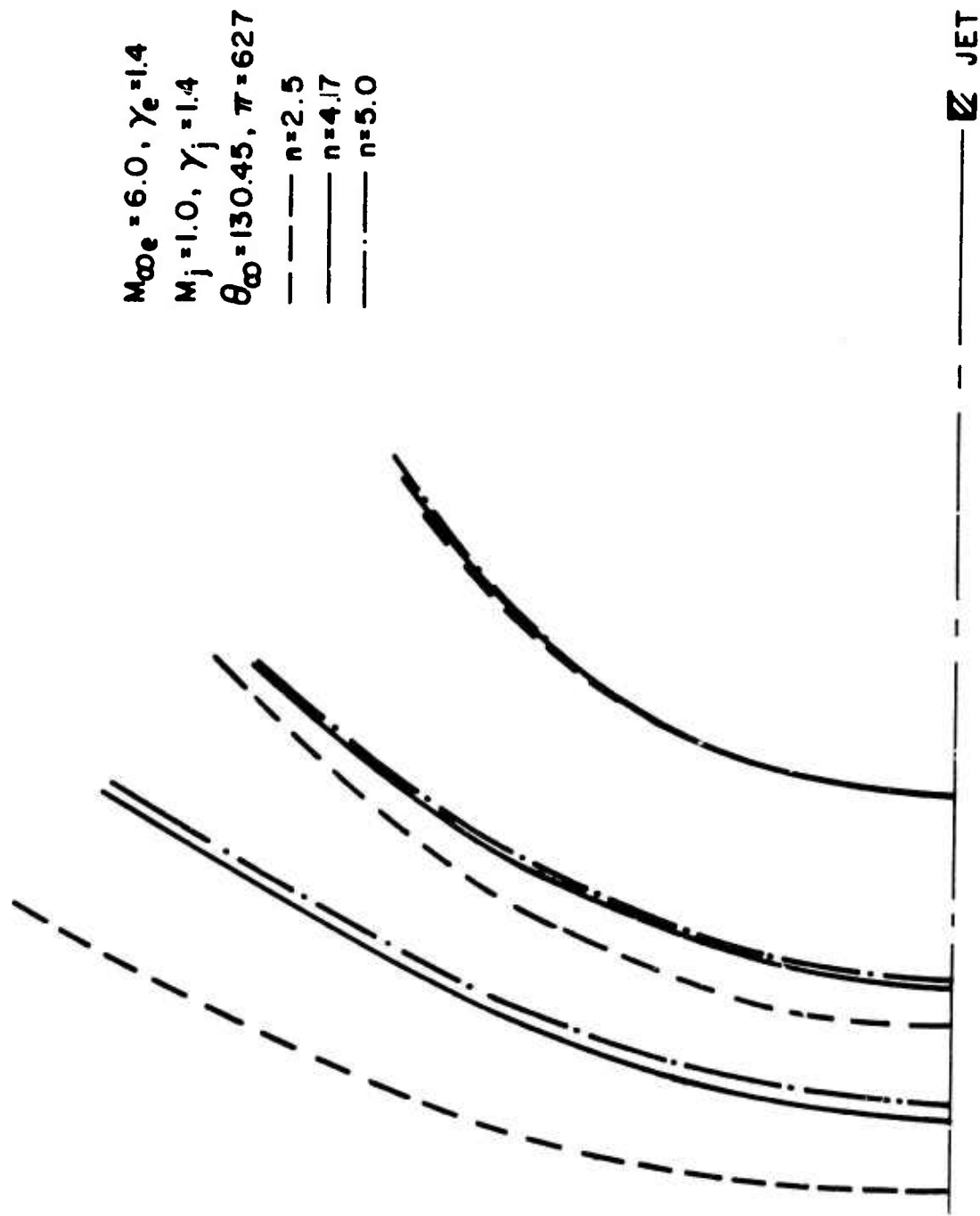


FIG. 10 VARIATION OF BOW GEOMETRY WITH n

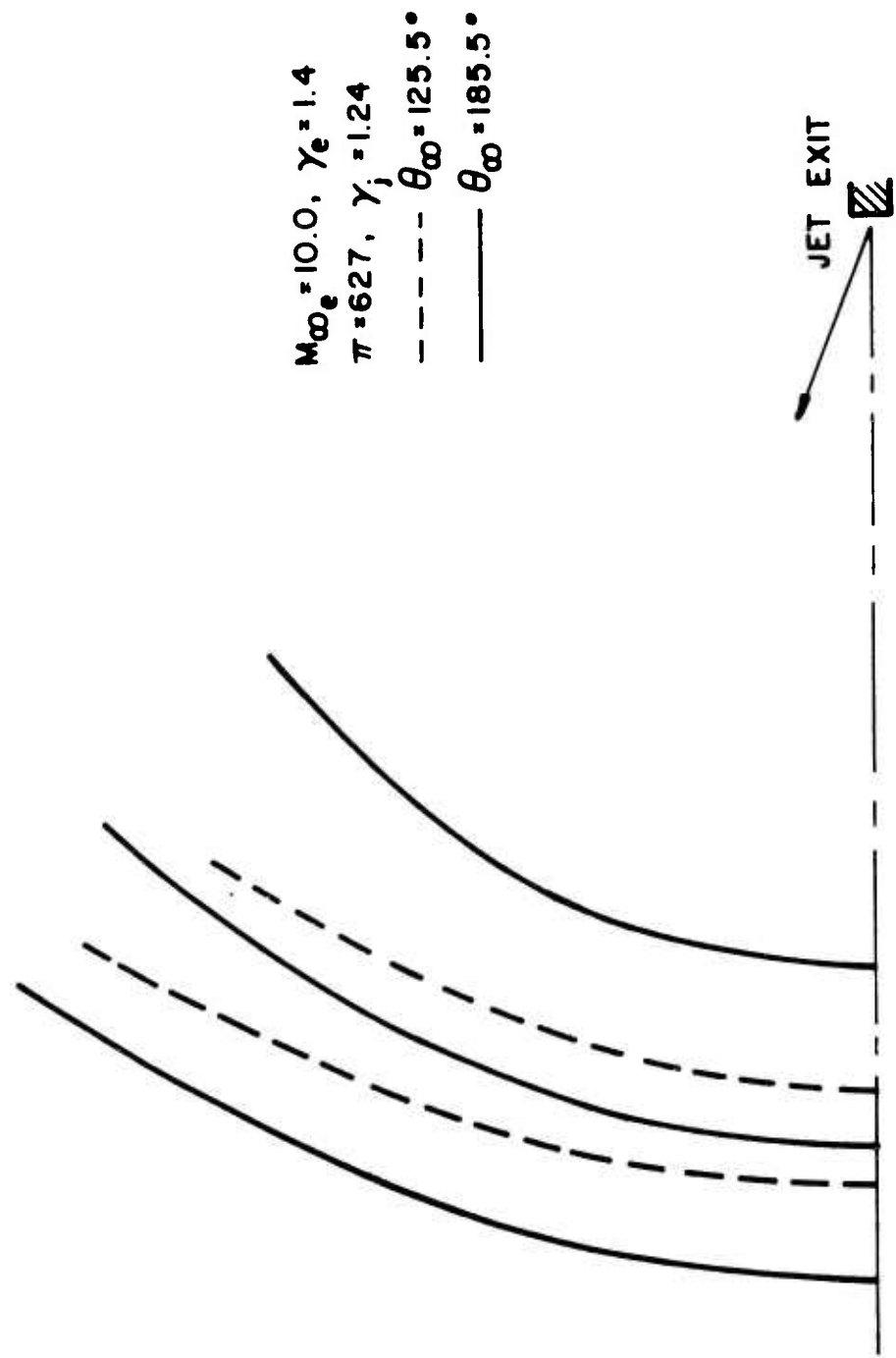


FIG. 11 VARIATION OF BOW GEOMETRY WITH θ_{∞}

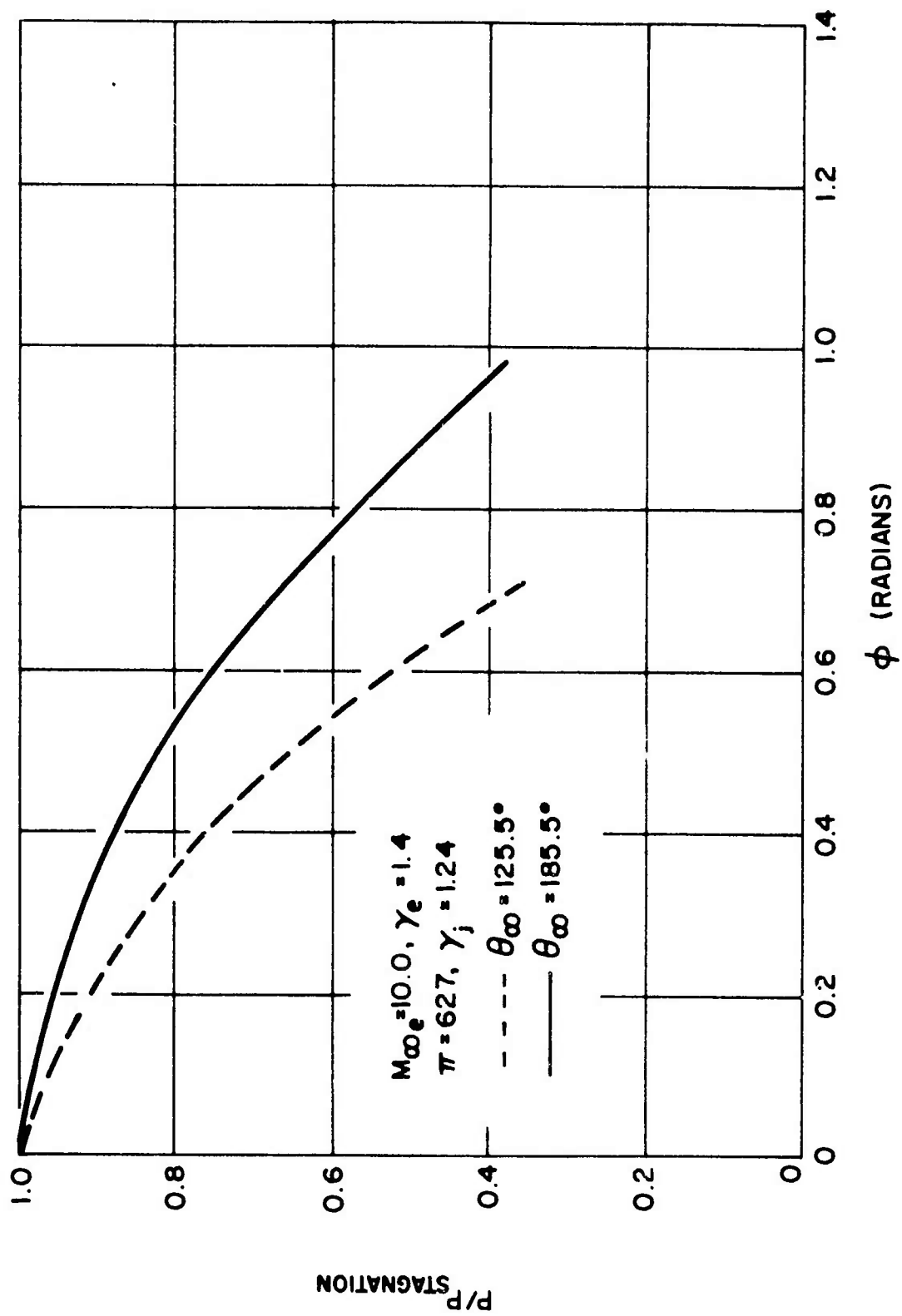


FIG. 12 VARIATION OF CONTACT SURFACE PRESSURE WITH θ_{∞}

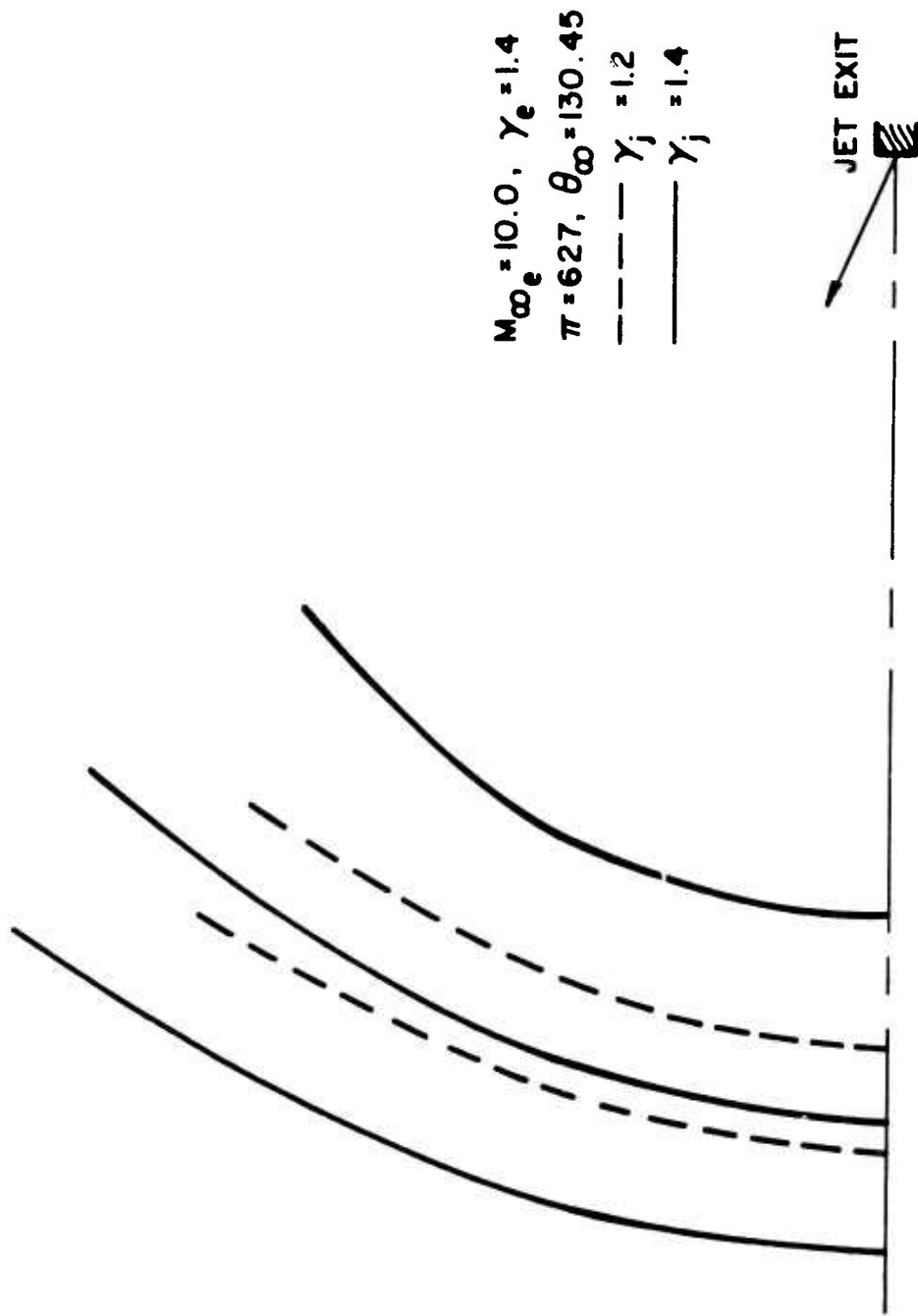


FIG. 13 VARIATION OF BOW GEOMETRY WITH γ_j

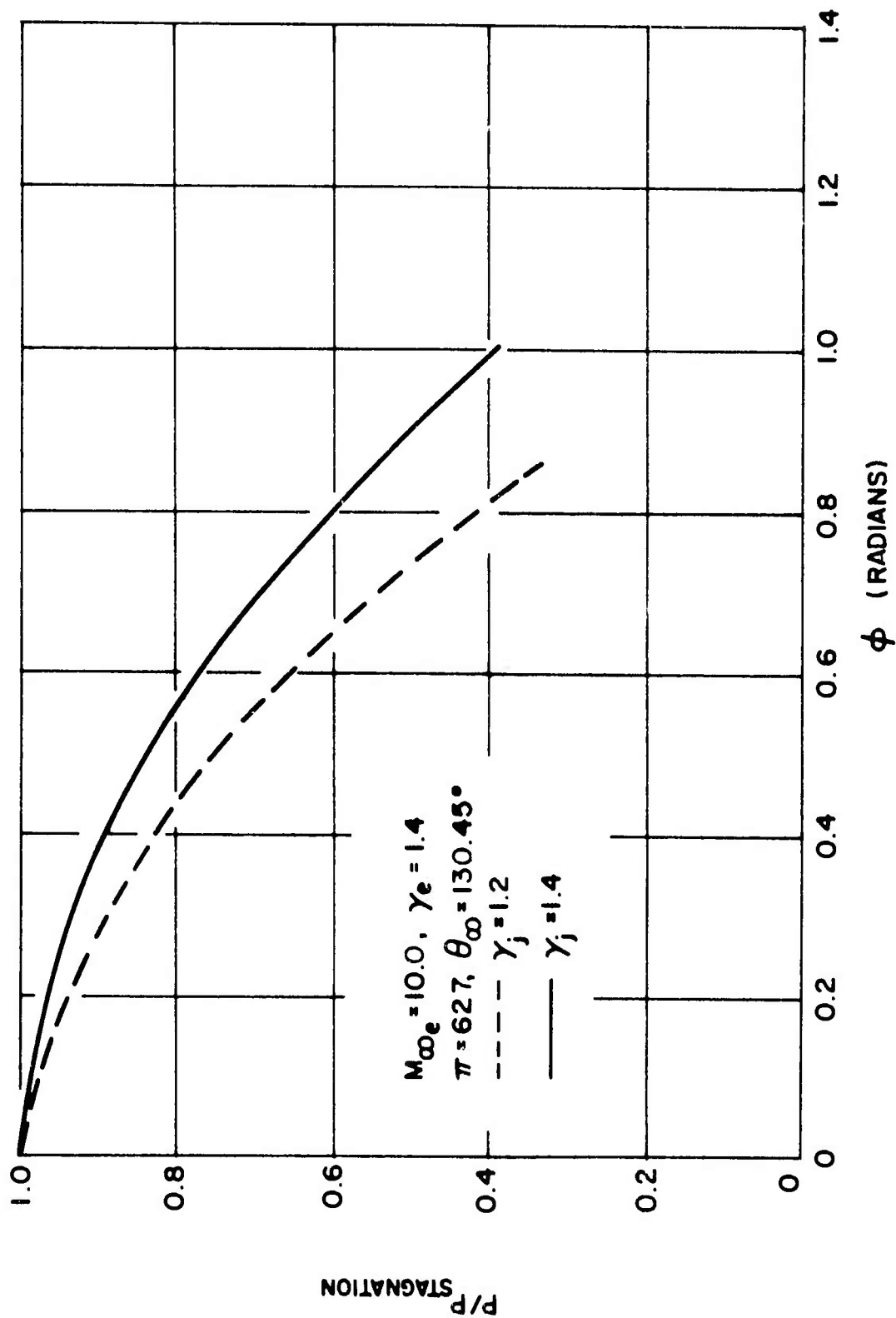


FIG. 14 VARIATION OF CONTACT SURFACE PRESSURE WITH γ_j

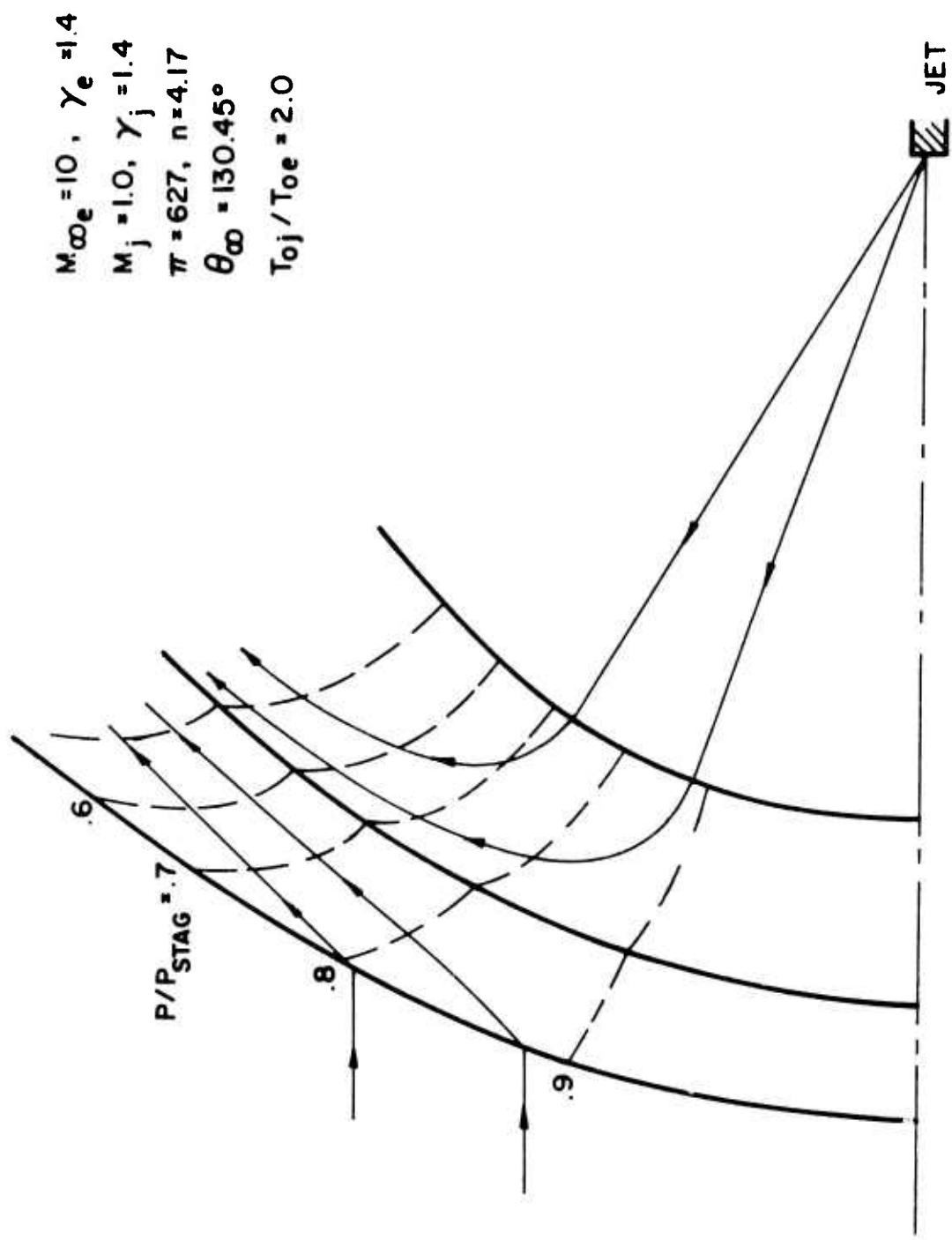


FIG. 15 ISOBARS AND STREAMLINES FOR BOW REGION

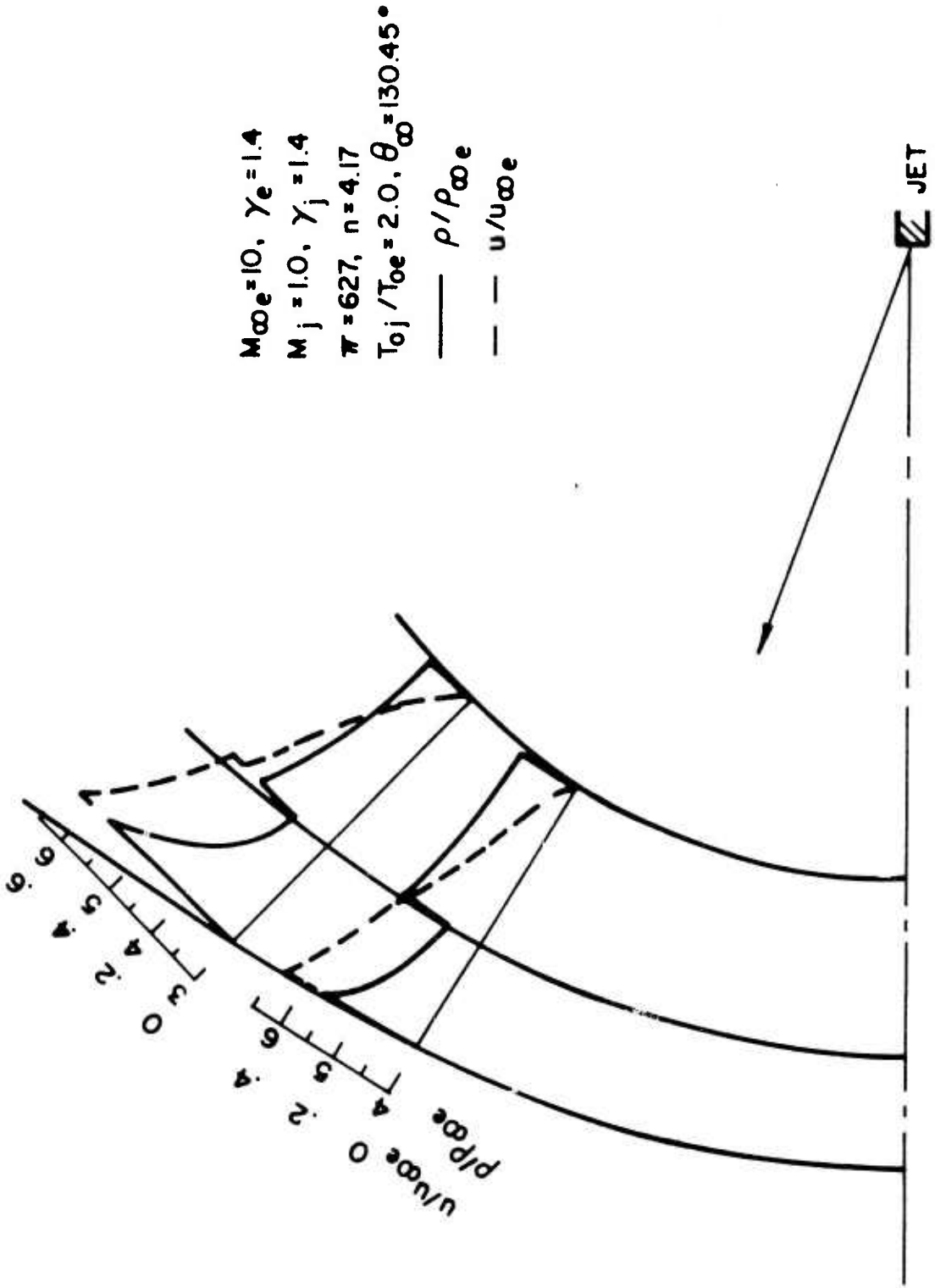


FIG. 16 DENSITY AND VELOCITY DISTRIBUTIONS FOR BOW REGION

$M_{\infty} = 10, \gamma_e = 1.4$
 $M_j = 3.0, \gamma_j = 1.24$
 $\pi = 627, n = 8.33$
 $\theta_{\infty} = 185.0^\circ$

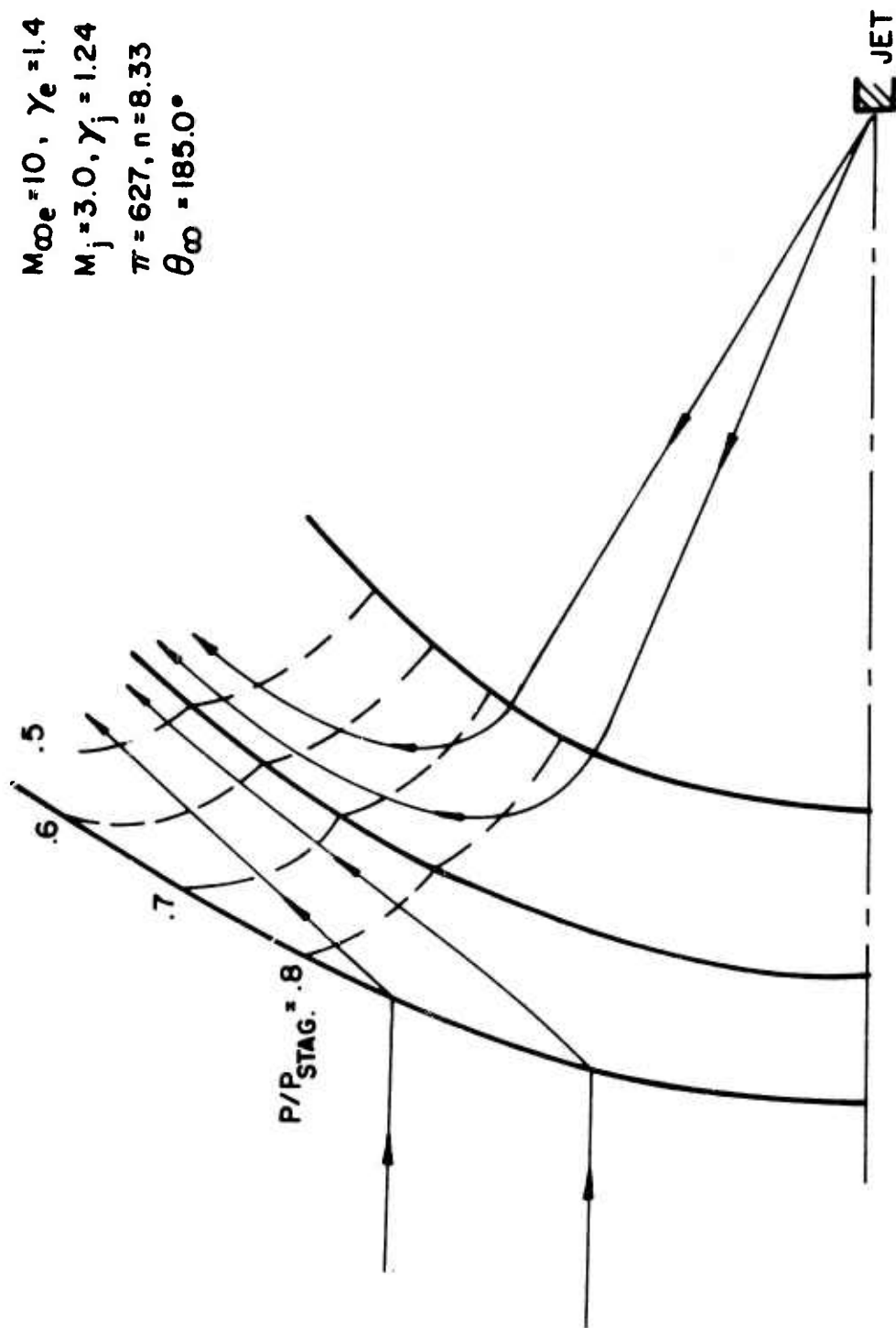


FIG. 17 ISOBARS AND STREAMLINES FOR BOW REGION

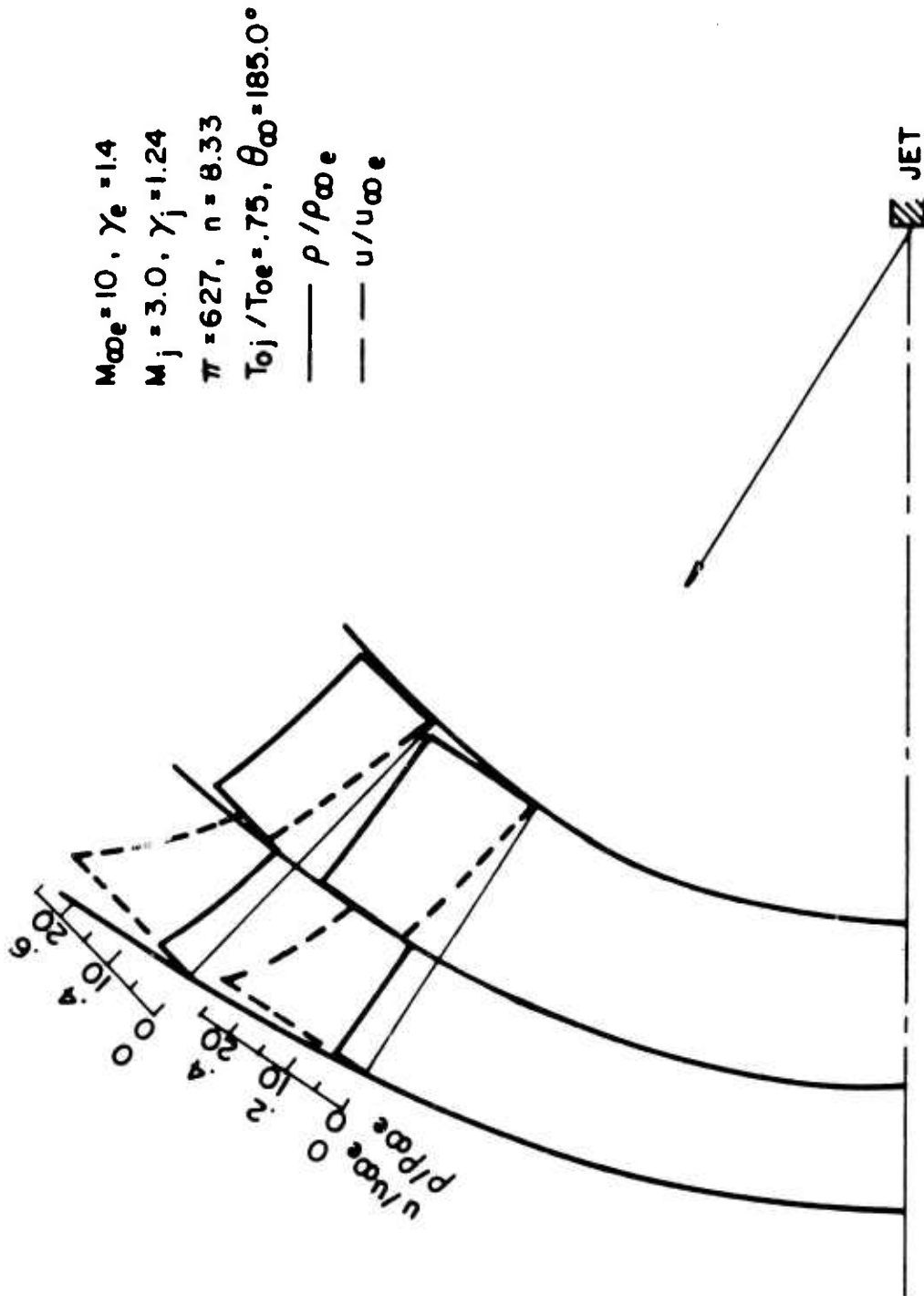


FIG. 18 DENSITY AND VELOCITY DISTRIBUTIONS FOR BOW REGION

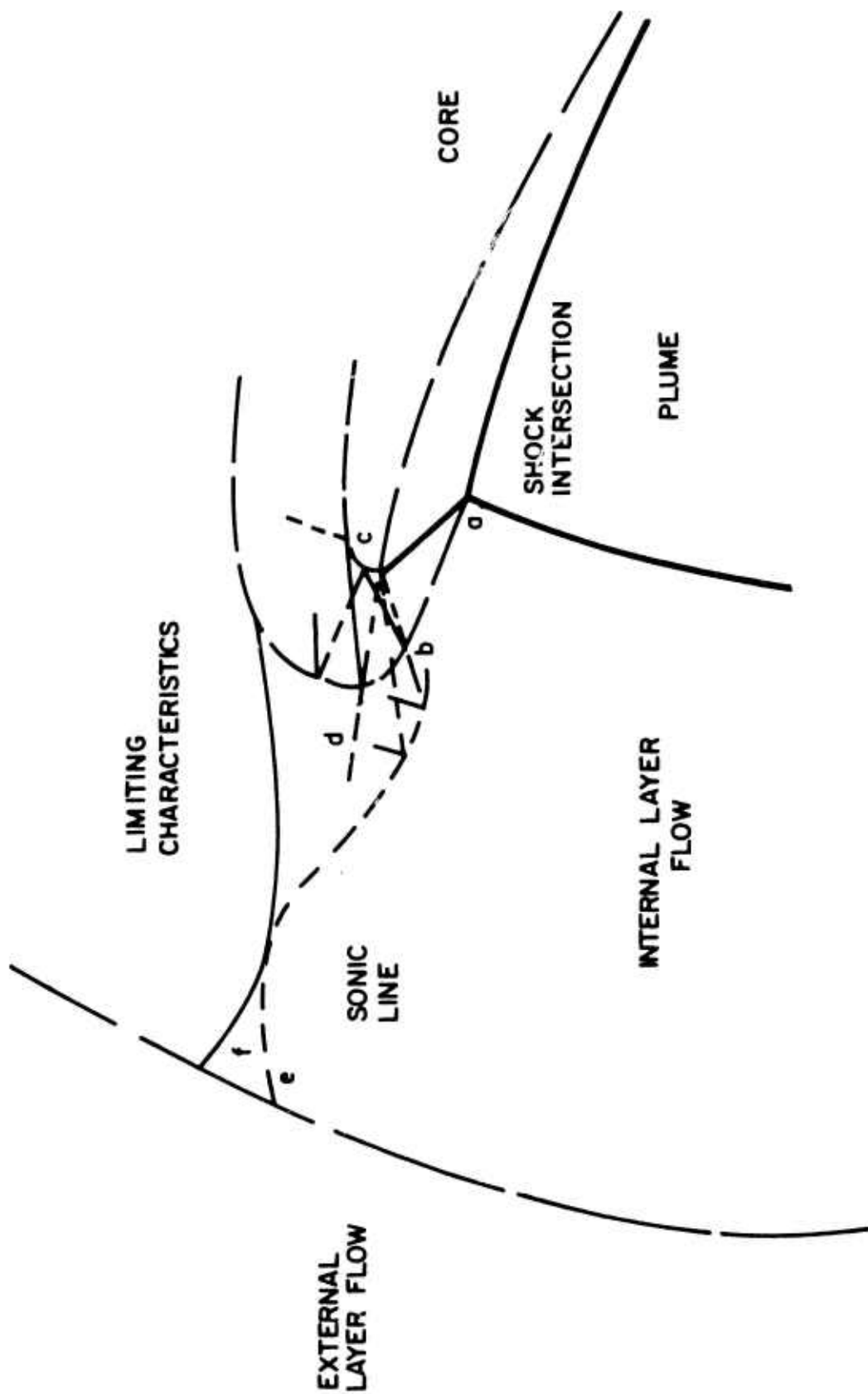


FIG. 19 CORNER REGION

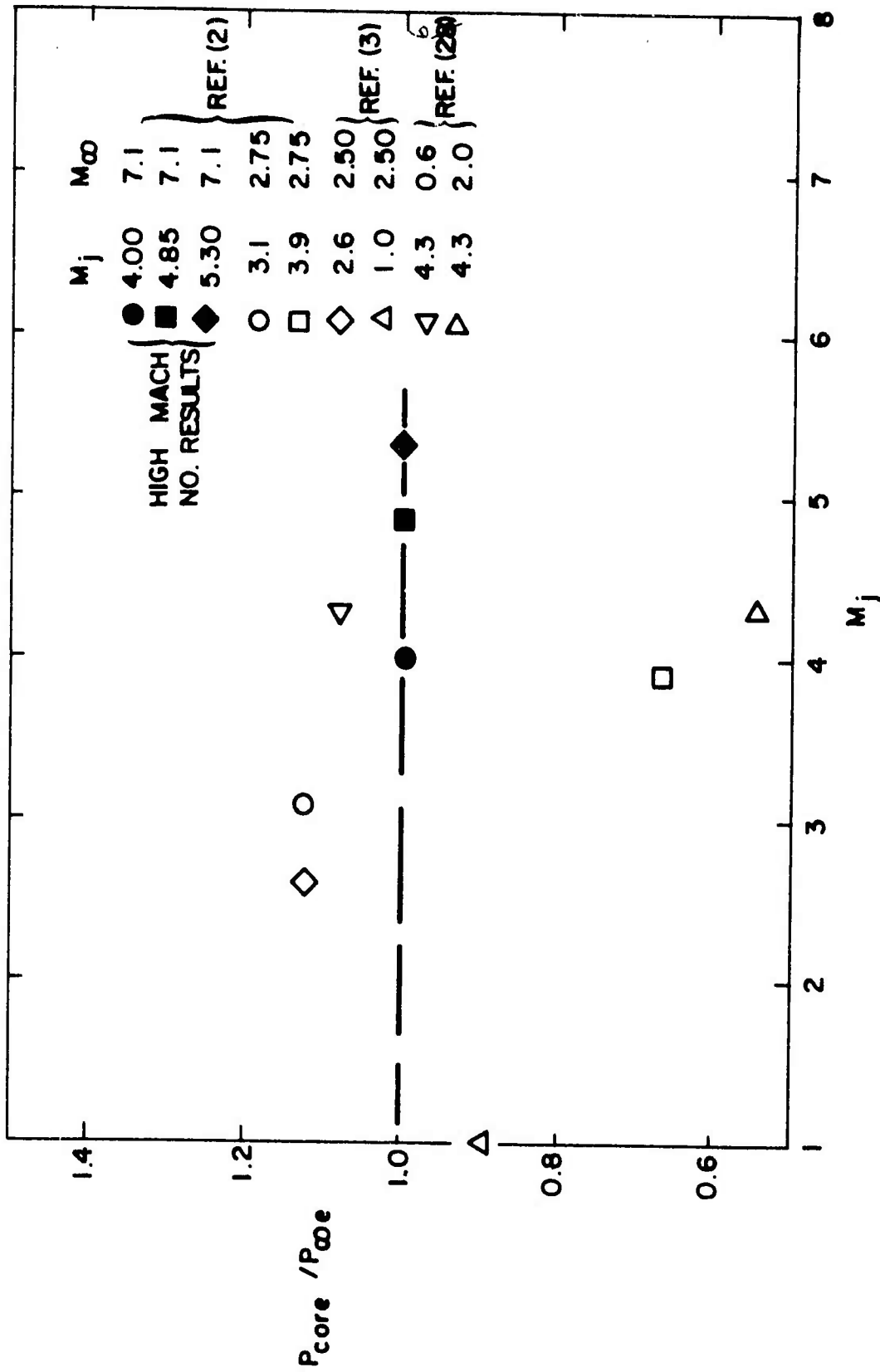


FIG. 20 CORE PRESSURE TO AMBIENT PRESSURE VS. JET EXIT MACH NUMBER

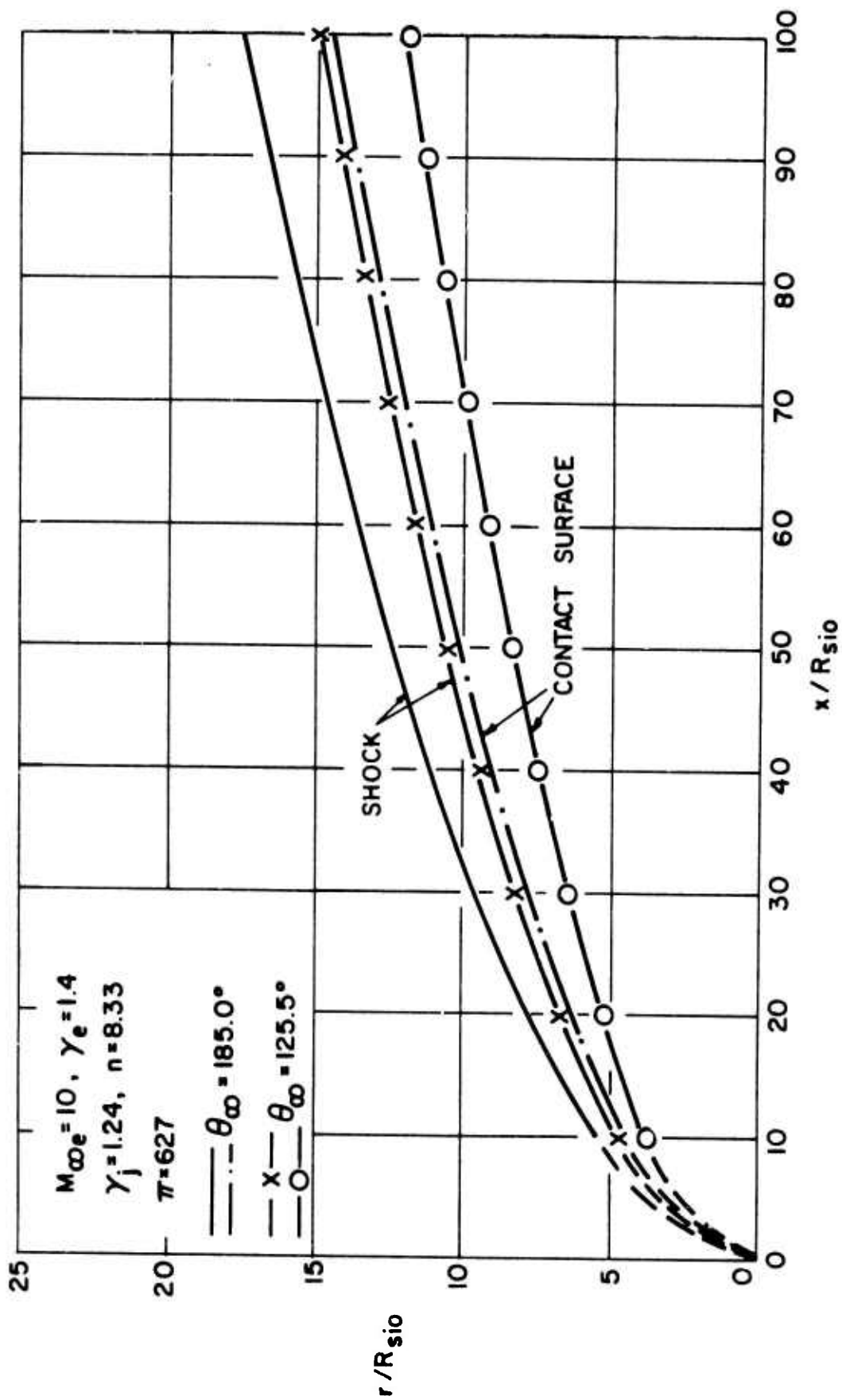


FIG. 21 FAR FIELD SHOCK AND CONTACT SURFACE POSITION

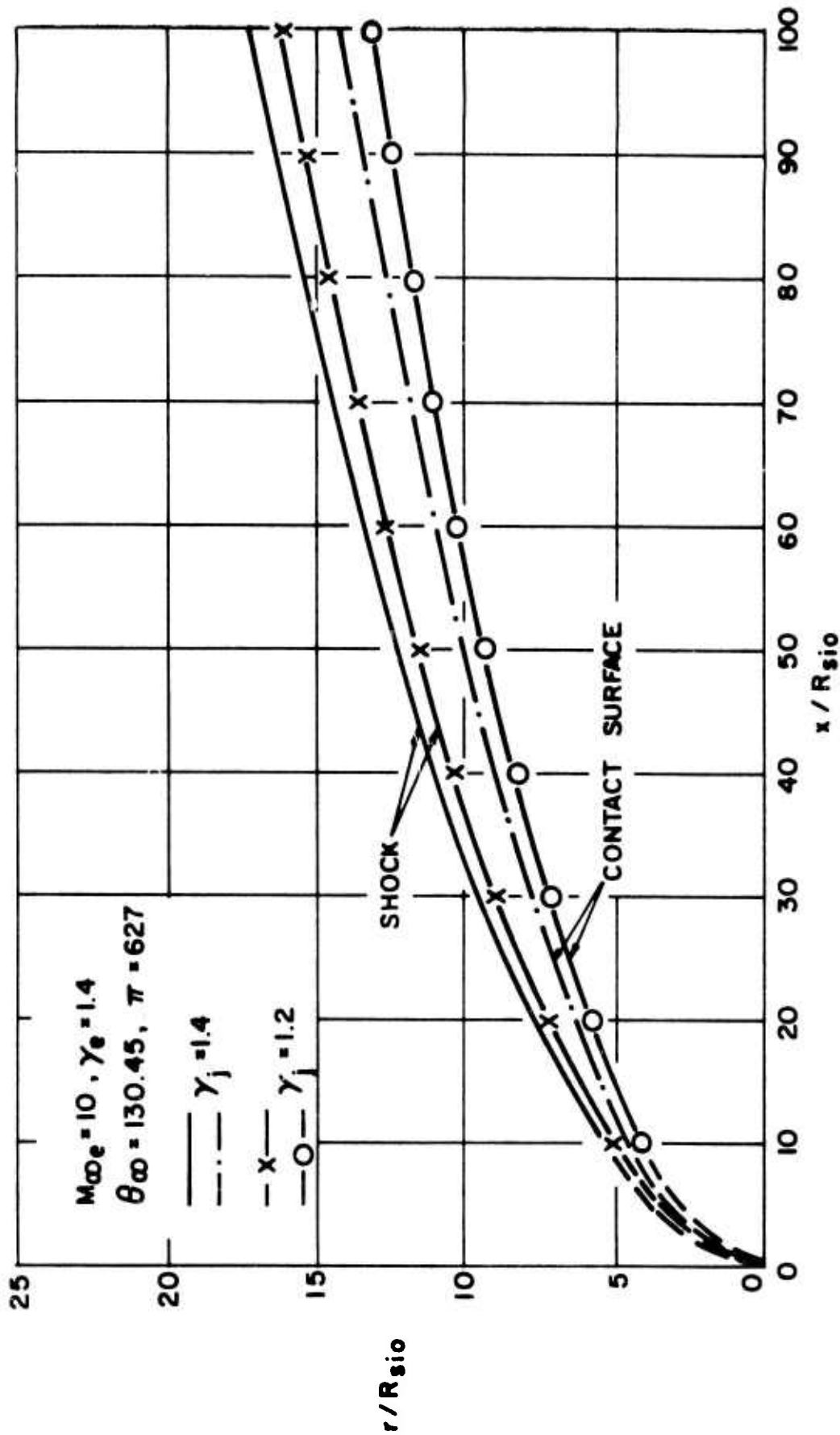


FIG. 22 FAR FIELD SHOCK AND CONTACT SURFACE POSITION

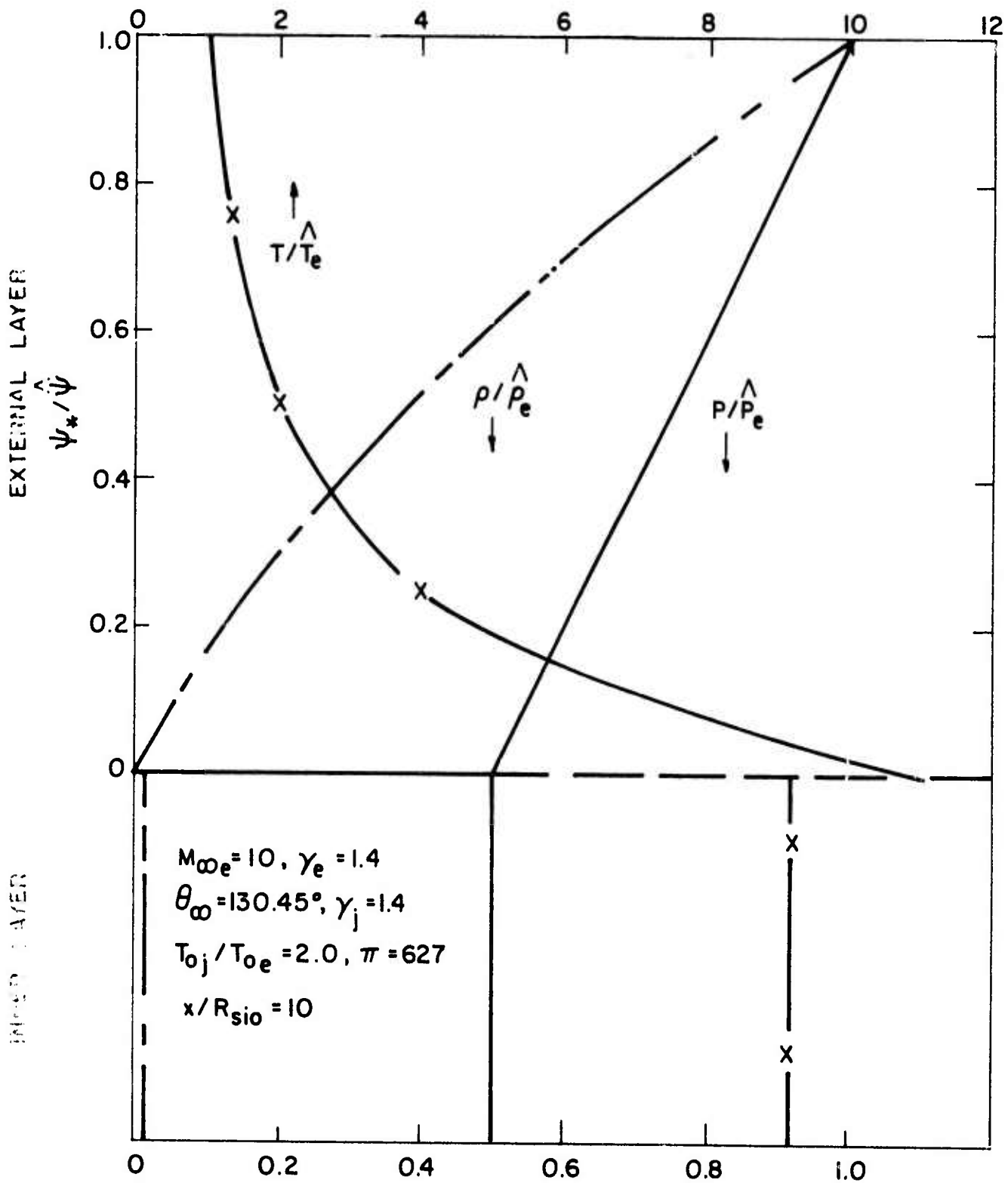


FIG.23 FAR FIELD PROPERTIES VS. STREAM FUNCTION

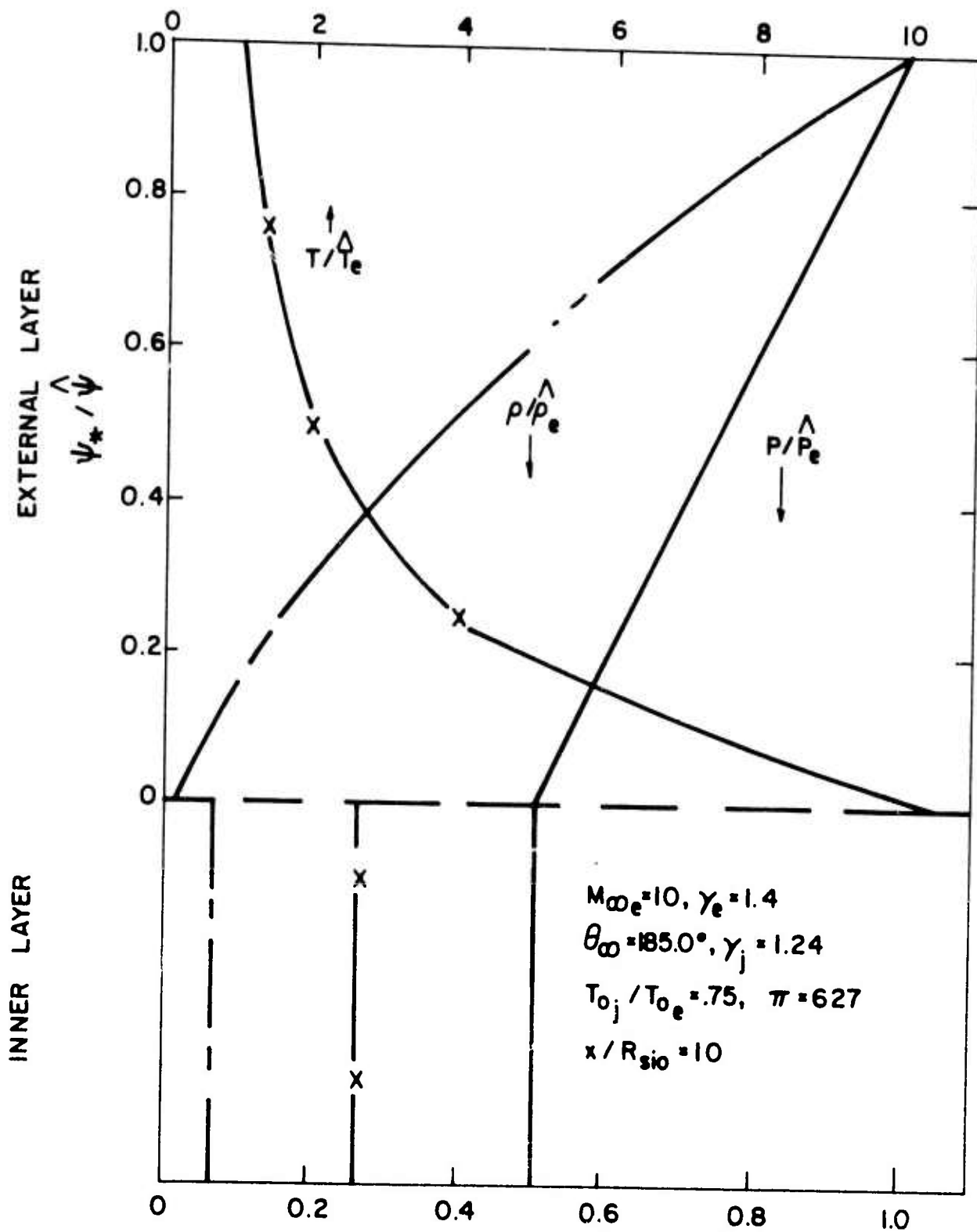


FIG. 24 FAR FIELD PROPERTIES VS. STREAM FUNCTION